Evaluation électrochimique d'électrocatalyseurs pour la réaction d'oxydation de l'eau : le cas de matériaux ultraporeux d'oxydes d'iridium et d'oxydes mixtes à base d'iridium

Silvia Alejandra Duran Amaya

▶ To cite this version:

Silvia Alejandra Duran Amaya. Evaluation électrochimique d'électrocatalyseurs pour la réaction d'oxydation de l'eau : le cas de matériaux ultraporeux d'oxydes d'iridium et d'oxydes mixtes à base d'iridium. Organic chemistry. Institut Polytechnique de Paris, 2021. English. NNT : 2021IPPAX095 . tel-03501623

HAL Id: tel-03501623
https://theses.hal.science/tel-03501623v1

Submitted on 23 Dec 2021

INSTITUT
POLYTECHNIQUE
DE PARIS

NNT : 2021IPPAX095

Thèse de doctorat

Electrochemical evaluation of oxygen evolution reaction electrocatalysts: the case of ultraporous iridium oxide and iridium-based mixed oxide materials

Thèse de doctorat de l'Institut Polytechnique de Paris
préparée à l'École Polytechnique

n°626: Ecole Doctorale de l'Institut Polytechnique de Paris
(ED IP Paris)
Spécialité de doctorat: Chimie

Thèse présentée et soutenue à Palaiseau, le 06 /12 /2021, par

Silvia Alejandra Duran Amaya

Composition du Jury :

Christel Laberty-Robert Professeure, Sorbonne Université (LCMCP)	Présidente
Laetitia Dubau Directrice de recherche, Université Grenoble Alpes (LEPMI)	Rapportrice
Têko Napporn Chargé de recherche, Université de Poitiers (IC2MP)	Rapporteur
Fouad Maroun Directeur de recherche, École Polytechnique (PMC)	Examinateur
Jennifer Peron Maîtresse de conférences, Université de Paris (ITODYS)	Examinatrice
Cédric Tard Chargé de recherche, École Polytechnique (LCM)	Directeur de thèse

“Escribe lo que no debe ser olvidado.”
-Isabel Allende-

“Write what should not be forgotten.”
-Isabel Allende-

ACKNOWLEDGEMENTS

First of all, I would like to thank my thesis jury who agreed to read and evaluate my work. I really enjoyed the questions and the discussion that followed my defense presentation. Special thanks to the rapporteurs Laetitia DUBAU and Têko NAPPORN for the precise and constructive input on my manuscript.

I would like to express my heartfelt appreciation to my supervisor Dr. Cédric TARD for giving me the opportunity to work with him, his patience, guidance, and knowledge, as well as his constant support to achieve this goal and make possible the development of this research. Made me grow professionally and allowed me to love more the research. Also, for making me feel comfortable while being so far from home. I also deeply thank our collaborators, the members of ITODYS (Jennifer, Marion and Marine) and LCMCP (Mateusz, Marco and Cédric) for their contributions to this work team.

I also thank to all the members of LCM team that is behind technical assistance and administration, as well as to all the other PhD students in LCM for opening the doors and for their contributions in the development of this project. I am particularly grateful to Sophie and Edith for always helping me when needed, and more precisely to my office partner and friend Radhika GUPTA (thank you for every laugh we had together in the office and outside the office, for all the times we got lost in Paris, and of course for letting me be your friend!). I also need to mention “my students” through all these three years that were so curious about electrochemistry, that made me realized how much I love teaching and how they contributed to my professional growth. To the people I met a long this journey outside the lab, and for friends that I met by the end of this process.

I want to thank my friends of the *SELVA* group (Monica, Claudia, Margarita, Carolina, Zulma and Sebastian), my Colombian friends that from the distance supported me for the past years when I shared good and bad news, for giving me new experiences and values. And thank you to a special person “*Churrito*” for his

"artistic" approval on the figures on my manuscript, and for encouraging me during the writing process.

Finally, a hearty thanks to my mom "*my engine*", my brother "*bola*", my father, and my whole family for their deeply love and support through this process, without this crazy family I would not be here writing this. I feel so lucky to be part of my family, thank them for their faith in me, allowing me to be as ambitious as I wish.

Silvia

RÉSUMÉ

La diversification des sources d’énergie en incorporant des technologies propres et renouvelables devrait jouer en rôle important pour s’affranchir du système actuel dominé par les énergies fossiles. L’hydrogène est un vecteur énergétique renouvelable prometteur, et l’électrolyseur d’eau à membrane échangeuse de proton (PEMWE) est une technologie reconnue pour produire du H_2 de haute pureté. Néanmoins, et malgré les performances prometteuses, une utilisation à grande échelle de ce type d’électrolyseur est confrontée à des problématiques de coût et d’efficacité pour lesquelles le catalyseur anodique est l’un des principaux contributeurs du fait de sa composition (matériaux à base d’iridium) et des grandes surtensions nécessaires pour la réaction de production d’oxygène (OER) qui induisent une cinétique lente.

Ce travail de thèse s’intéresse à l’étude électrochimique de différents catalyseurs à base d’iridium pour l’OER. Plusieurs stratégies ont été employées pour déterminer différentes propriétés comme la surface électroactive (ECSA) et la stabilité et la dégradation en condition d’électrolyse afin de pouvoir décrire, analyser et comparer les différents catalyseurs. Les dérivés d’oxydes mixtes de formule $Ir_{1-x}Mo_xO_2$ (x =0, 0.1, 0.3, 0.5, 0.7 and 1) ont été synthétisés par le procédé de spray-drying (déshydratation par atomisation) et calcinés à différentes températures entre 400 et 800 °C pour réduire le métal noble (Iridium) dans l'anode et d'améliorer la surface spécifique de l'oxyde d'iridium pur. Les électrocatalyseurs ont été caractérisés par diffraction des rayons X sur poudre (XRD), microscopie électronique à balayage (SEM), spectrométrie photoélectronique X (XPS) et spectroscopie d’absorption des rayons X (XAS). L’étude par SEM de ces matériaux a confirmé les morphonologies poreuses et amorphes à basses températures de calcination et les échantillons contenant 70 % de Mo présentaient une morphologie supplémentaire sous forme de plaquettes dans 400 et 600 °C. L’analyse des spectres XRD a aussi pu établir que les catalyseurs contenant x = 0.1, 0.3 and 0.5 ne presentent qu’une seule phase et sont obtenus à partir des températures de frittage de 450, 500 et 550 °C, respectivement. Cela a montré que l'ajout de molybdène retarde la cristallisation et que la taille des cristallites diminue avec molybdène. En revanche, les échantillons avec x = 0,7 présentent la coexistence des phases $Ir_{1-x}Mo_xO_2$ et MoO_3 à basse température de calcination.

En utilisant une électrode à disque tournant (RDE), les caractérisations électrochimiques par voltammétrie cyclique (CV) et chronoampérométrie, ainsi que des mesures de capacitance de double couche (C_{dl}) et d'électrodéposition à sous-potentiel de mercure (Hg-UPD) ont permis de s'intéresser aux mesures de surface électroactive de ces matériaux. Les CV de tous les oxydes mixtes a permis de comparer et d'observer l'influence de la température de frittage sur les performances vis-à-vis de l'OER. Pour observer l'influence de l'état d'oxydation de l'iridium sur les performances des OER iridium - oxydes de molybdène, les spectres XPS et XANES ont montré que lors de l'observation de l'état d'oxydation de l'iridium dans les températures sélectionnée, toutes les compositions ont mis en évidence Ir^{4+} ou la transition de Ir^{3+} à Ir^{4+}. Ainsi il a pu être démontré que l'état d'oxydation de l'iridium n'influence pas les performances électrocatalytiques de ces oxydes mixtes. De plus, les deux techniques démontrent que le même état d'oxydation est présent dans la surface comme et au cœur des matériaux. Trois des composés de la série $Ir_{1-x}Mo_xO_2$ (x = 0,1, 0,3, 0,5) calcinés à 450, 500 et 550 °C, respectivement, ont présenté les meilleures performances OER et ont été étudiés pour leur stabilité comme matériaux anodiques, où les trois composés ont maintenu un potentiel constant pendant plusieurs heures, suggérant que ces séries d'oxydes possèdent une bonne stabilité au cours du processus OER

La détermination de la surface électrochimique (ECSA) par différentes approches électrochimiques telles que la méthode de capacitance à double couche (Cdl) a permis d'obtenir une tendance du comportement du courant de charge de l'électrocatalyseur en fonction de la température de frittage, tandis que le méthode Hg-UPD permettait d'obtenir des résultats comparables aux mesures BET pour ces matériaux ultraporeux pur et poreux mixte. Enfin, malgré la méthode les trois compositions principales ont montré la plus grande surface sont aux températures de calcination optimales.

ABSTRACT

Diversifying energy sources by incorporating cleaner technologies i.e., renewable energy sources, are expected to play an important role to move from the current non-renewable dominated energy system. One of the promising energy carriers for renewable energy systems is hydrogen, and proton exchange membrane water electrolyzer (PEMWE) is one of the technologies known to produce highly pure H_2. Regardless the promising performances, large-scale use of such device faces efficiency and cost issues, among which the anode catalyst material is one of the main contributors due to its composition (Ir-based materials) and high overpotential towards the oxygen evolution reaction (OER) (slow kinetic).

This thesis work aimed to electrochemically study several Ir-based OER catalysts by different strategies since properties such as electrochemical surface area (ECSA), stability/degradation tests and catalytic processes are critical characteristics to describe, analyze and compare electrocatalysts. The mixed oxides derived from $Ir_{1-x}Mo_xO_2$ (x =0, 0.1, 0.3, 0.5, 0.7 and 1) were synthesized by the spray-drying process and calcined at different temperatures in the range 400 – 800 °C to address the challenge to reduce the noble metal content (Iridium) in the anode and enhanced the surface area of pure iridium oxide. The electrocatalysts were characterized by X-ray powder diffraction (XRD), scanning electron microscopy (SEM), X-ray photoelectron spectroscopy (XPS) and X-ray absorption spectroscopy (XAS). The SEM study of these materials confirmed the amorphous - porous morphologies at lower calcination temperatures and samples with 70%Mo exhibited an additional morphology in the form of platelet the range 400 – 600°C. XRD Rietveld refinements indicated single phases compounds were obtained for x = 0.1, 0.3 and 0.5 starting from the sintering temperatures of 450, 500 and 550 °C, respectively. This showed that the addition of molybdenum delays the crystallization, and the crystallite size decreases with molybdenum content. In contrast, samples with x = 0.7 present the coexistence of $Ir_{1-x}Mo_xO_2$ and MoO_3 phases at low calcination temperature.

The electrochemical characterization using rotating disc electrode (RDE) technique consisted of cyclic voltammetry (CV) and chronoamperometry, as well as double layer capacitance (C_{dl}) and Hg underpotential deposition (Hg-UPD), which allowed to investigate their ECSA. The CV of all the mixed oxides allowed to compare and observed the influence of the sintering temperature on the performance towards OER. To observe the influence of iridium oxidation state on OER iridium – molybdenum oxides performance, XPS and XANES measurements showed that when observing the oxidation state of iridium at the selected temperature range, all compositions evidenced Ir^{4+} or the transition from Ir^{3+} to Ir^{4+}. Thus, iridium oxidation state does not rule over iridium – molybdenum oxides OER performance. Furthermore, both techniques demonstrating that the same oxidation state is present in the surface as in the bulk. Three of the compounds of the series $Ir_{1-x}Mo_xO_2$ (x = 0.1, 0.3, 0.5) calcined at 450, 500 and 550 °C, respectively, exhibited the best OER performance and were selected to be further studied in view of the stability, where the three compounds maintained a constant potential over the course of several hours, suggesting that these oxide series possess a good stability during the OER process.

Electrochemical surface area (ECSA) determination by different electrochemical approaches such as double layer capacitance (C_{dl}) method allowed to obtain a trend of the charging current behavior of the electrocatalyst as function of the sintering temperature, while the Hg underpotential deposition (Hg-UPD) method results prove its relevancy and applicability for ultraporous and porous Ir-mixed oxides when tested in RDE giving consistent ECSA values in agreement with BET measurements**.** Finally, despite the method the three main compositions exhibited the largest surface are at the optimal calcination temperatures.

TABLE OF CONTENTS

ABBREVIATIONS

BET	Brunauer-Emmett-Teller
CA	chronoamperometry
CE	counter electrode
CNF	carbon nanofibers
CNT	carbon nanotubes
CO	carbon monoxide
CP	chronopotentiometry
CV	cyclic voltammetry
ECSA	electrochemical surface area
GC	glassy carbon
HER	hydrogen evolution reaction
LSV	Linear sweep voltammetry
MEA	Membrane electrode assembly
NHE	normal hydrogen electrode
NM	noble metal
NP	nanoparticle
OER	oxygen evolution reaction
PEM	proton exchange membrane
PEMWE	proton exchange membrane water electrolyzer
PMMA	Polymethylmethacrylate
RE	reference electrode
RDE	rotating disk electrode
SCE	saturated calomel electrode
SEM	scanning electron microscopy
TMC	transition metal catalyst
UPD	under potential deposition
WE	working electrode
XANES	x-ray absorption near edge structure
XPS	x-ray photoelectron spectrometry
XRD	x-ray diffraction

LIST OF SYMBOLS

Symbol	*Unit*	*Definition*
A	m^2	Area of the adsorbed gas molecule
C_{dl}	$\mu F\ cm^{-2}$	Differential double layer capacitance
C*	$\mu F\ cm^{-2}$	Reference double layer capacitance
E	V	electrode potential
E^0	V	standard potential
F	$C\ mol^{-1}$	Faraday's constant
ΔG	$kJ\ mol^{-1}$	Gibbs free energy
ΔG^0	$kJ\ mol^{-1}$	standard Gibbs free energy
ΔH	$kJ\ mol^{-1}$	enthalpy
ΔH^0	$kJ\ mol^{-1}$	standard enthalpy
i	mA	electric current
i_a	mA	anode electric current
i_c	mA	cathode electric current
i_0	mA	exchange electric current
j	$mA\ cm^{-2}$	current density
j_0	$mA\ cm^{-2}$	exchange current density
j_a	$mA\ cm^{-2}$	anode current density
j_c	$mA\ cm^{-2}$	cathode current density
n		number of electrons
η	mV	overpotential
η_{10}	mV	overpotential at 10 $mA\ cm^{-2}$
$N_{avogadro}$	mol^{-1}	Avogadro number
Q	$\mu C\ cm^{-2}$	Charge current under adsorption peak
R	$J\ mol^{-1}\ K^{-1}$	gas constant
S	$m^2\ g^{-1}$	Surface area of the catalyst
S_{BET}	$m^2\ g^{-1}$	Surface area of the catalyst by BET
S_{HgUPD}	$m^2\ g^{-1}$	Surface area of the catalyst by Hg-UPD
ΔS	$kJ\ mol^{-1}\ K^{-1}$	entropy
T	K	absolute temperature
ν	$mV\ s^{-1}$	Scan rate
V	V	voltage
α		charge transfer coefficient
α_a		anode charge transfer coefficient
α_c		cathode charge transfer coefficient

GENERAL INTRODUCTION

In recent years, the energy crisis has become one of the biggest challenges the world has to face. Major changes have to be made in energy systems to diversify energy sources incorporating cleaner technologies, leading to better use of energy. As a result, renewable energy sources are a great hope, however, these technologies present some issues including efficient energy storage. Therefore, water electrolyzers are possible solution to develop hydrogen as an energy vector.

Among electrolysis technologies, proton exchange water electrolyzer (PEMWE) is one of the most promising technologies for energy storage. This device is producing highly pure H_2, working at high current densities and pressures, and presenting high energy efficiencies comprised between 80 - 90%. Therefore, considering the relevance of the PEMWE technology for hydrogen production, this thesis proposes to investigate the issues presented by state-of-the-art catalysts for water oxidation in PEMWEs. These catalytic materials must be able to drive the catalytic reaction at low overpotentials and to present high catalytic activity and efficient mass transport of liquid and gases.[1] Also, they ought to have more durability, higher thermodynamic efficiency and lower cost of interconnects, since the electrolyzers performance is impeded mainly by the catalyst at the anode that drives the oxygen evolution reaction (OER).[2] For this reason, in recent years, research has focused on finding better catalysts than those according to the state-of-the-art, namely RuO_2 and IrO_2 derivatives.[3] The latter is exhibiting good activity and stability towards the OER but reducing its loading in the device is crucial since its cost is too high to meet the long-term costs of PEMWE and large-scale development.

However, new arrangements of Ir and Ru based oxides materials are still attractive as anode materials, and new routes of synthesis could also be investigated. As an example, extensive studies of Ru-Ir alloys and oxides have been carried out in order to enhance their activity and thermodynamic stability.[4-8] On the other hand, catalyst properties have been tuned by doping with Co,[9-11] K,[12] Bi,[13] Sn,[14] Ta[15] and Pt.[16] These materials are amorphous oxides and have been shown to be more active than single metal oxides. Our research focuses precisely on similar Ir-based oxide materials in order to find improved characteristics with respect to existing materials based on the achievements that have been obtained in recent years in this area.

In this order of ideas, the present thesis is based on the substitution of iridium by molybdenum in the form $Ir_{1-x}Mo_xO_2$ to study the Ir-mixed oxides as anode materials for the oxygen evolution reaction. As an example, IrO_2-MoO_3 hybrid composites were recently reported for OER by *Tariq et al.,*[17] and showed a 70% mole fraction of noble metal content, good conductive network, excellent stability and activity in acid environments. The work presented here deals with the study of the $Ir_{1-x}Mo_xO_2$ (x= 0, 0.1, 0.3, 0.5, 0.7 and 1) series as an anode catalyst based on the relationship between their structural characteristics and the improvement of the electrochemical behavior in the cell. Chapter 1 describes the state of art (scientific context), the operation of PEMWEs and the general requirements of the main components (anode, cathode and electrolyte). Chapter 2 presents the structural characterizations of the $Ir_{1-x}Mo_xO_2$ series. Chapter 3 highlights the performances of the Ir-Mo oxides as catalysts for the oxygen evolution reaction and stability tests by cyclic voltammetry (CV). Chapter 4 concerns the comparison of the different techniques to evaluate the Electrochemical Surface Area (ECSA). Chapter 5 presents the main conclusions mentioned in the previous chapters and finally, Chapter 6 presents a resume of the experimental methods that have been used throughout this work.

This work was carried out in collaboration with a research group at the laboratory ITODYS (group of Jennifer Peron and Marion Giraud, Université de Paris), providing us the Ir-Mo catalysts used for all the electrochemical methods performed by myself. SEM, XRD and BET characterization results presented in this thesis were performed also at the laboratory ITODYS.

CHAPTER 1. STATE OF THE ART

1.1. Introduction

1.1.1. Environmental context

Energy related issues such as renewable energy sources, dependency on fossil fuels and greenhouse gas emissions have become topics of global interest. The diversification in energy systems must be capable of providing security, profitability, and reliability to economic activities as well as to society of any country, since they present a high dependency on the currently most used source: fossil fuels.[18] Nowadays, wind and solar technologies have been able to demonstrate their large scale use, despite being limited by the geography area, since its use has been growing over the years according to the statistics of the International Energy Agency (IEA) (Figure 1.1).[19] This potential growth is strongly linked to the use of energy storage devices (Figure 1.2), however, those present some challenges such as modularization of the energy, cost of equipment, and energy storage efficiency.[20] Nevertheless, even if CO_2 emissions showed a stabilization in 2019 with 33.2 Gt [21] compared to the previous years, it is of primary importance to improve current renewable storage and usage technologies such as fuel cells and electrolyzers.

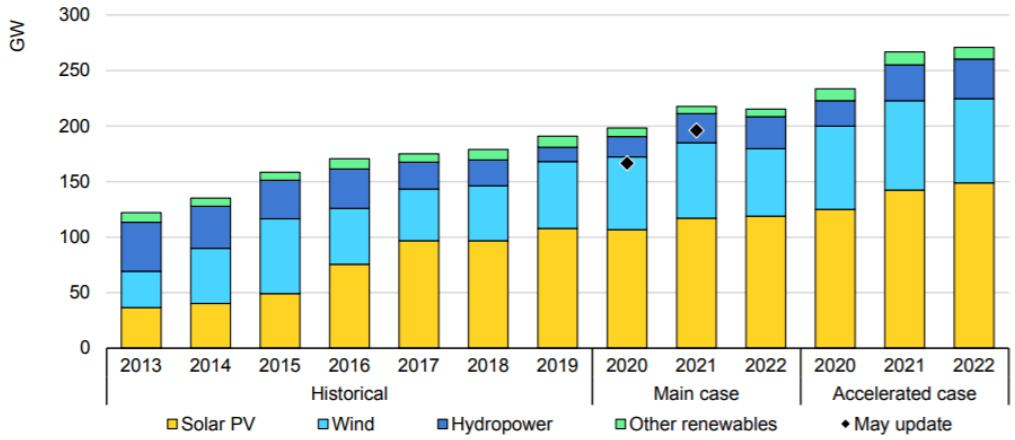

Figure 1.1. Electricity generation by different renewable sources (taken from[19]).

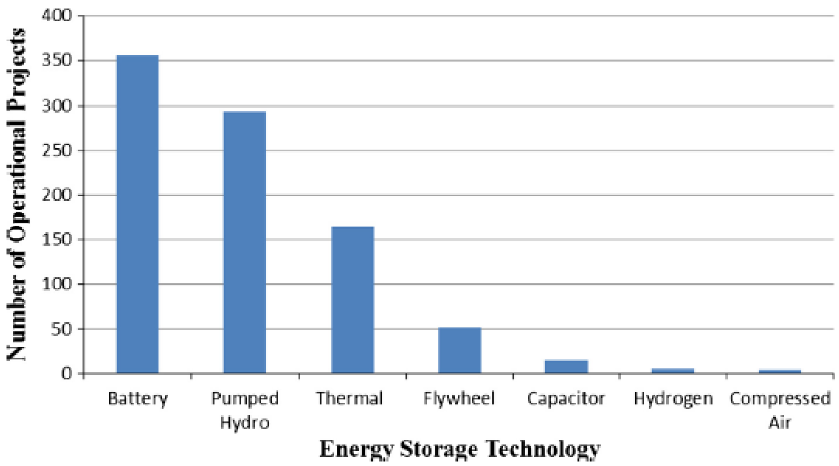

Figure 1.2. Use of different energy storage devices on operational projects in 2016 (taken from[20]).

On this basis, hydrogen appears to be a suitable clean energy vector, however, its main source comes from natural gas reforming process. Therefore, producing hydrogen while implementing an efficient energy device from a clean source, opens an interesting approach on how to integrate durability, availability, and efficiency.[22-25]

1.1.2. Hydrogen economy

Hydrogen as an energy vector is based on the potential to provide energy in an economically, environmentally, socially, and financially manner to country's services.[26, 27] Molecular hydrogen (H_2) can be obtained from different production methods such as photocatalytic, enzymatic, fermentative, steam reforming and electrolysis (Figure 1.3).[28] Currently, 120 Mt of hydrogen are produced each year, generated mainly from natural gas and coal, and consuming around 2% of the global total primary energy demand for its production.[29] It is expected that hydrogen by 2050 could meet 6 to 18% of the global energy demand, 20 to 25% of the transportation industry and ca. 10% of global building heating demand.[26] In order to accomplish those target numbers, the production systems currently available should transition to better resources, reinforcing the development of new hydrogen technologies and improving the current ones.

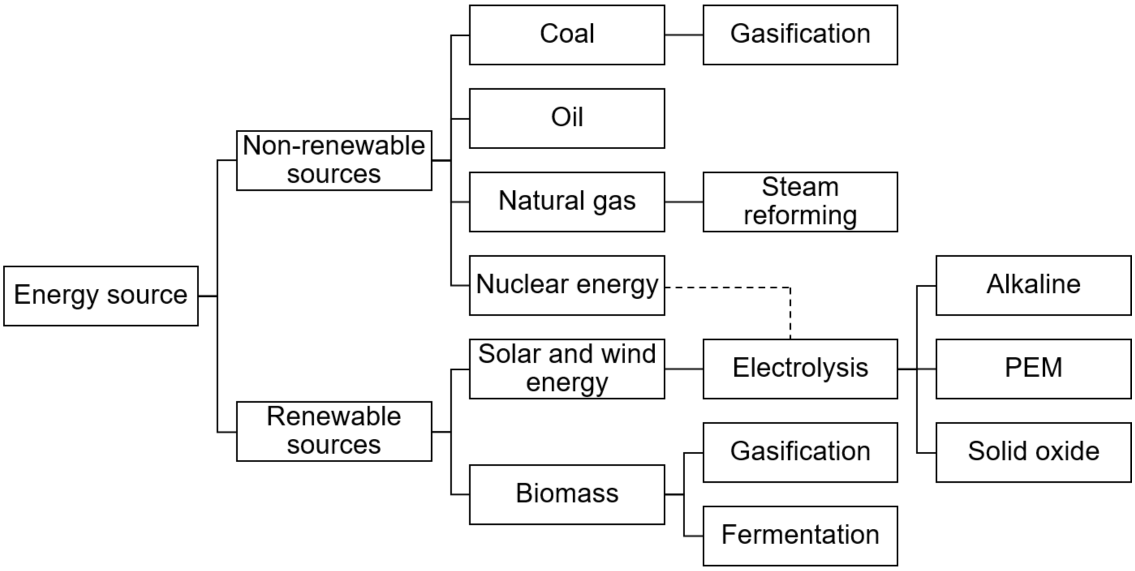

Figure 1.3. Main hydrogen production methods.

Water splitting is considered as the most environmental friendly way of hydrogen production, since it uses an abundant resource (water) while carrying a simple electrocatalytic process resulting on high hydrogen purity.[30] This hydrogen is generated in water electrolyzers by the process of electrolysis when a current is applied, and can be stored and then used for conversion in to electrical energy using fuel cells.[22, 25]

1.2. Water electrolyzers

The electrolysis of water is described in Eq. 1-1, where water is the reactant and splits into hydrogen and oxygen. The process happens in two half reactions known as hydrogen evolution reaction (HER, Eq. 1-3) and oxygen evolution reaction (OER, Eq. 1-2).

Water splitting: $H_2O \rightarrow H_2 + \frac{1}{2}O_2$ *(Eq. 1-1)*

Anode: $H_2O \rightarrow 2H^+ + 2e^- + \frac{1}{2}O_2$ *(Eq. 1-2)*

Cathode: $2H^+ + 2e^- \rightarrow H_2$ *(Eq. 1-3)*

Water electrolyzer devices may be classified in different types based on their operating conditions, electrolyte, and ionic agents.[22, 31] As shown in Table 1.1, the four technologies are briefly resume with their corresponding operational principles, operational temperatures, advantages, disadvantages, and ion exchange.[31-33]

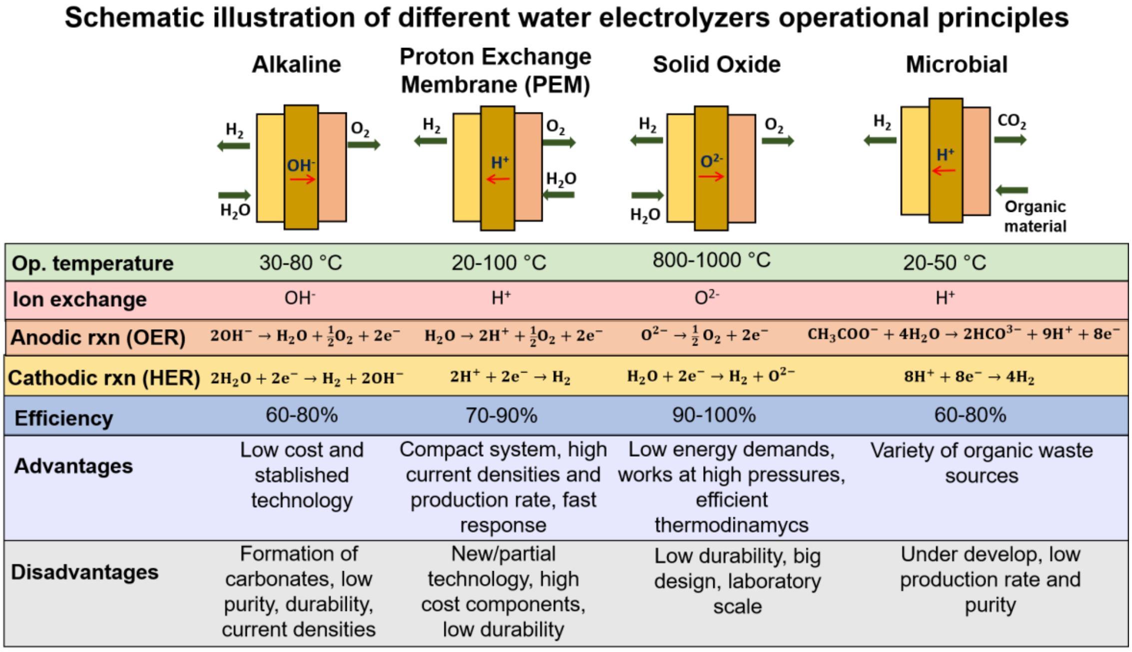

Schematic illustration of different water electrolyzers operational principles

	Alkaline	Proton Exchange Membrane (PEM)	Solid Oxide	Microbial
Op. temperature	30-80 °C	20-100 °C	800-1000 °C	20-50 °C
Ion exchange	OH^-	H^+	O^{2-}	H^+
Anodic rxn (OER)	$2OH^- \rightarrow H_2O + \frac{1}{2}O_2 + 2e^-$	$H_2O \rightarrow 2H^+ + \frac{1}{2}O_2 + 2e^-$	$O^{2-} \rightarrow \frac{1}{2}O_2 + 2e^-$	$CH_3COO^- + 4H_2O \rightarrow 2HCO^{3-} + 9H^+ + 8e^-$
Cathodic rxn (HER)	$2H_2O + 2e^- \rightarrow H_2 + 2OH^-$	$2H^+ + 2e^- \rightarrow H_2$	$H_2O + 2e^- \rightarrow H_2 + O^{2-}$	$8H^+ + 8e^- \rightarrow 4H_2$
Efficiency	60-80%	70-90%	90-100%	60-80%
Advantages	Low cost and stablished technology	Compact system, high current densities and production rate, fast response	Low energy demands, works at high pressures, efficient thermodinamycs	Variety of organic waste sources
Disadvantages	Formation of carbonates, low purity, durability, current densities	New/partial technology, high cost components, low durability	Low durability, big design, laboratory scale	Under develop, low production rate and purity

Table 1.1. Main characteristics of water electrolyzers.

Among the devices presented in Table 1.1, the solid oxide electrolyzer (SOE) is the only one for which operation temperature is much higher than the others (> 800 °C). This system uses the same materials used in solid oxide fuel cells (SOFC), such as Yttria-stabilized zirconia (YSZ), lanthanum strontium manganite (LSM) and Ni-YSZ, as electrolyte, cathode and anode materials, respectively.[22, 25, 31] However, this high operational temperature causes degradation of the system and lack of stability on the long term. A recent approach on the low temperature, microbial electrolyzer based on the use of renewable biomass and wastewaters has been proposed.[34] The process starts at the anode where the organic matter is oxidized by microbial organisms producing CO_2, protons and electrons. Protons and electrons then combine at the cathode to produce H_2.[22] This technology is still under development since stabilizing the operational temperature is crucial to maintain the organisms in optimum conditions for a long-term operation.[34] On the other hand, among these electrolyzers that operates at low temperatures, the alkaline electrolyzer is the most commercially available and well-stablished technology. For these devices, the electrolyte usually is a solution of KOH, and this alkaline medium improves the kinetics of the reactions at the electrodes. However, major drawbacks of this electrolyzer are the low current densities (< 400 mA cm^{-2}),[22, 35] the high ohmic losses across the electrolyte and diaphragm, and the formation of insoluble carbonates when the electrolyte comes in contact with the gasses (i.e., air, CO/CO_2).[36]

To overcome the challenges presented in the latter electrolyzer, the introduction of a solid polymer electrolyte into the electrolyzer allowed to overcome the low current densities and pressure operation, and mixing of gasses, resulting in PEM water electrolyzers. This one, nowadays, is considered as the most promising technologies for the conversion of hydrogen, in terms of sustainability, environmental impact and being a compact system.[1-3, 22, 24, 32, 37]

1.2.1. Proton Exchange Membrane Water Electrolyzer (PEMWE)

A proton exchange membrane water electrolyzer (PEMWE) is a solid polymer based electrochemical device that converts water into hydrogen and oxygen by electrochemical reactions. The polymer membrane allows the conduction of protons, but also the separation of gases and the prevention of corrosion phenomenon. PEMWE uses a solid polymer electrolyte (SPE) and operates at temperatures in the range of 20 to 100 °C. The SPE main role is to achieve high current densities (> 2 A cm^{-2}),[22] values reachable since the membrane leads to lower ohmic losses. The operating temperature allows compact and stackable designs with minor safety issues,[32] and the compact system allows to achieve high operational pressures (up to 700 bar, differential pressure).[38]

The basic design of a PEMWE consists of two electrodes (cathode and anode), an electrolyte (the polymer membrane), bipolar plates, current collectors and gas diffusion layers (GDL). Figure 1.4 presents the cross-section of a PEM electrolyzer and detailed operational scheme.

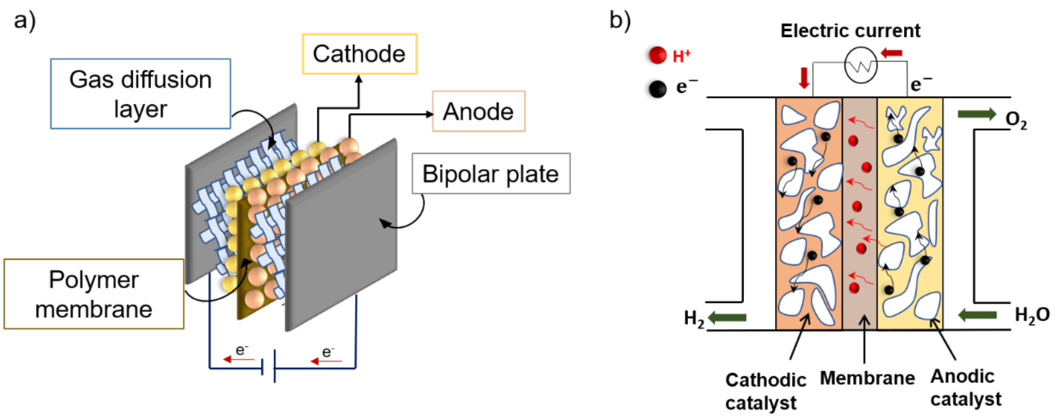

Figure 1.4. Scheme of a) membrane electrode assembly (MEA) and b) operational principle of PEMWE.

The simplified structure of a PEMWE presents a layer of a solid acidic polymer membrane (electrolyte) that lies between the two electrodes (anode and cathode) separating gas products and transport of protons. The anode and cathode are where the half reactions, oxygen evolution and hydrogen evolution, take place. The bipolar plates ensure the distribution of fuel and separates individual cell in a stack, and the mechanical stability. It also facilitates mass transport (i.e., water, gas) and heat management. The current collectors, on the other hand, allow the transport of two-phase fluid (liquid/gas) from the channels to the electrodes, and collects electrons.[37, 39, 40]

The operation of a PEMWE involves the splitting of water electrochemically into hydrogen and oxygen at the cathode and anode, respectively. Water is pumped into the anode splitting into oxygen (O_2), electrons (e^-) and protons (H^+). The latter travels via the polymer electrolyte (membrane) to the cathode section. The electrons are transported through the external power circuit in order to recombine with the protons to produce hydrogen (H_2). For this process, some energy is required, which can be calculated from the Gibbs free energy (ΔG), the standard free energy of reaction (ΔG^0; 25° C, 1 atm) and is equal to 237 kJ mol^{-1}, associated to the theoretical cell potential in Eq. 1-4, where *n* is the number of electrons and *F* is Faraday's constant:[22]

$$E^0 = \frac{\Delta G^0}{\mathrm{nF}} = 1.23\ \mathrm{V} \qquad \textit{(Eq. 1-4)}$$

However, since some entropy (ΔS) is generated, the change of enthalpy (ΔH) becomes more suitable following Eq. 1-5, and at standard conditions ΔH^0 equals to 298 kJ mol^{-1}:

$$\Delta \mathrm{H} = \Delta \mathrm{G} + \mathrm{T}\Delta S \qquad \textit{(Eq. 1-5)}$$

Therefore, the required voltage, now called thermo-neutral voltage (V_{TN}), results in 1.48 V (Eq. 1-6):

$$\mathrm{V_{TN}} = \frac{\Delta \mathrm{H}}{\mathrm{nF}} = \frac{\Delta \mathrm{G}}{\mathrm{nF}} + \frac{\mathrm{T}\Delta \mathrm{S}}{\mathrm{nF}} = 1.48\ V \qquad \textit{(Eq. 1-6)}$$

The excess of energy produced by the process is transformed into heat ($T\Delta S$) during the electrolysis, which adds to the total energy requirement, then the need of Gibbs free energy (ΔG) decreases as the temperature increases.[38] Moreover, for the water electrolysis in the cell assembly it is necessary to take into account the resistances generated by the electrochemical reactions (anodic and cathodic overpotentials) as well as the ohmic resistance (IR drop) for the total cell voltage.

1.3. PEMWE components

1.3.1. Solid polymer membrane

The membranes, in order to work efficiently, must have: (i) high strength, (ii) high efficiency and high oxidative stability, (iii) dimensionally stable with change of temperature, (iv) good durability, (v) high proton conductivity, (vi) high density (>90%) in order to avoid interconnected porosity, and (vii) operate at high current densities (2 A/cm^2).[41] The membranes for a PEMWE are mainly materials with perfluorosulfonic acid (PFSA) polymer, such as Nafion®, Aquivion®, Fumapem® or Flemion®.[22] Some other polymer membranes can be also used based on polybenzimidazoles (PBI), polyether sulfones (PES) and sulfonated polyether ketones (S-PEEK).[37]

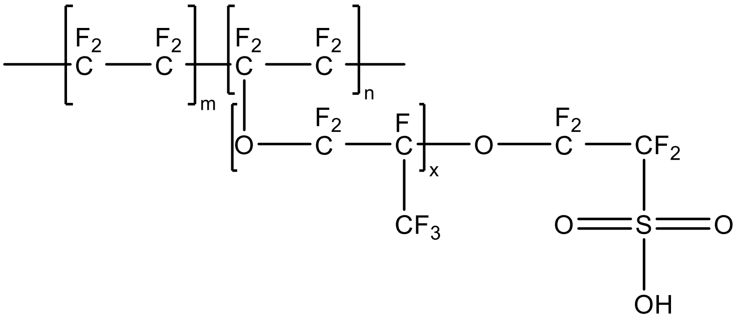

Figure 1.5. Chemical structure of Nafion.

The most commonly used is Nafion® (117, 115, 112 and 105) from *Dupont*, the difference among them relays on the equivalent weight and material thickness (i.e., Nafion 117 = 1100 g EW and 0.007 inches in thickness).[42] These membranes have shown good mechanical strength (yield strength between 1.82-2.50 MPa),[43] chemical and thermal stability (> 190 °C), high proton conductivity (> 0.2 S cm^{-1}),[44] high resistance to gas-crossover and current densities (> 1.5 A cm^{-2}) and high durability.[1, 37, 45] The main properties of Nafion membranes are water uptake, electro-osmotic drag coefficient and proton conductivity.[45] First, PFSA membranes (Figure 1.5) contain sulfonic acid ($SO_3^- H^+$) chains, which are heavily related to proton conductivity and water uptake. The latter is strongly influenced by the pretreatment of the membrane, high temperatures (> 100° C) for drying resulting in lower water content, and thus low proton conductivity. Furthermore, the electro-osmotic drag coefficient depends on the water uptake. To overcome this, TiO_2 and SiO_2 have been added to reinforce the membranes in order to operate higher temperatures and pressures, since these oxides are known for their water retention properties.[46, 47] Second, the polytetrafluoroethylene (PTFE) backbone provides robustness and stability while operating in acidic or alkaline environments.[48] Knowing these parameters allows to fabricate good membrane electrode assemblies (MEAs) (Figure 1.4a), which are the core of the PEMWE, consisting in an ionomer solution, a membrane and electrocatalysts (anode and cathode).

1.3.2. Electrocatalyst for PEMWE

1.3.2.1. Requirements

The electrocatalysts main function is to speed up the reaction kinetics in all the electrolysis devices presented in Table 1.1. On a general level, a well performing electrocatalyst must present the following characteristics:[22, 31, 32]

i. High electrochemical active surface area (i.e., porous material).
ii. Good chemical and electrochemical stability (i.e., catalytic activity and high corrosion resistance).
iii. High electrical conductivity (efficient electron transfer).
iv. Excellent mechanical stability for operating at high temperatures and pressures.
v. Reduce overpotential to carry out the cathodic and anodic reactions (i.e., good charge transfer kinetics for lower activation energy)
vi. Low capital cost to compete with traditional energy sources.

In the case of alkaline systems, the fulfillment of the above requirements is not as demanding as in proton exchange membrane water electrolyzers due to its acidic environment. Therefore, the electrocatalysts for PEMWE are usually expensive noble metals like iridium or iridium-ruthenium mixed oxide for the anode, and Pt black or Pt/carbon supported for the cathode, in contrast to the less expensive transition metals on alkaline electrolyzers.[49-52]

1.3.2.2. Cathodes for hydrogen evolution reaction (HER)

a) Hydrogen evolution reaction (HER)

One of the most widely investigated electrochemical reaction is the hydrogen evolution reaction (HER), a two-electron process where protons are reduced to molecular hydrogen as written in Eq. 1-3. The mechanism in acidic environment follows first an electrochemical hydrogen adsorption (Volmer reaction, Eq. 1-7) reaction, and secondly an electrochemical hydrogen desorption (Volmer-Heyrovsky or Volmer-Tafel reactions, Eq. 1-8 and Eq. 1-9, respectively) reaction:[53, 54]

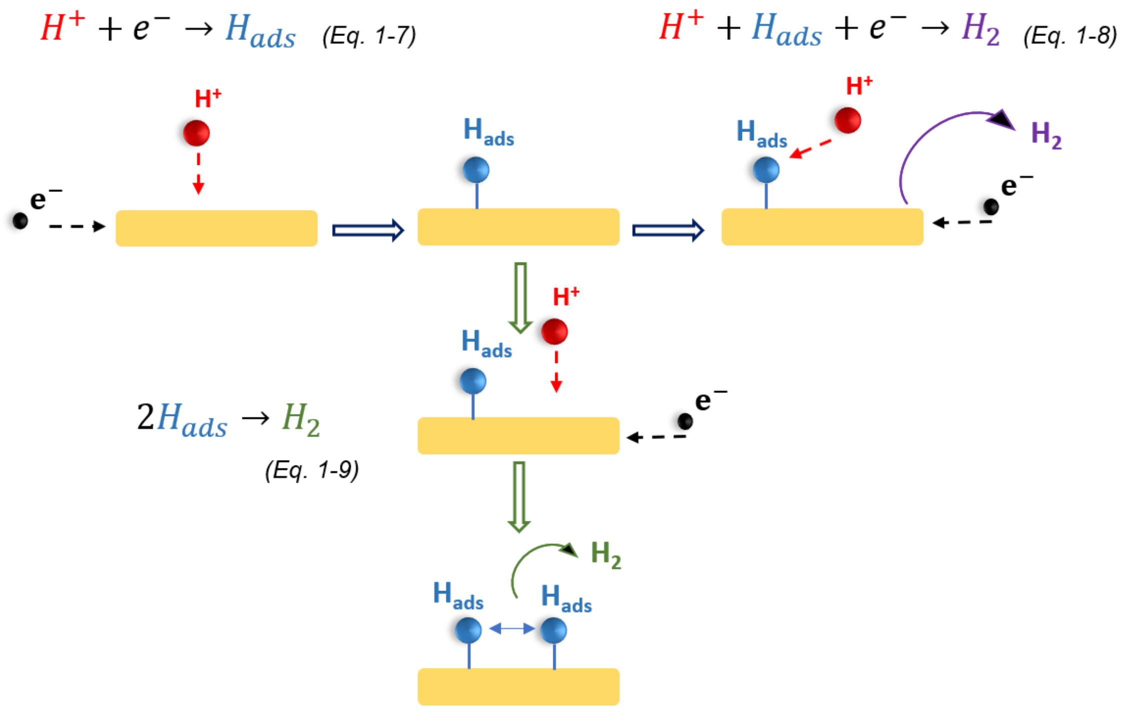

Figure 1.6. Two mechanisms of HER on the surface of the electrocatalyst in acid solution.

Depending on the kinetic that the catalysts present, the mechanism can be either a combination of Volmer + Tafel or a Volmer + Heyrovsky reactions, since adsorbed hydrogen is the only intermediate (Figure 1.6). Therefore, the challenges in PEMWE towards the HER were and are still focused on decreasing the cost of the well stablished electrocatalyst (Pt) as wells as increasing the performance and durability during operation.

b) Noble metals (NMs) electrocatalysts

Pt-catalysts are typical cathode materials in a PEMWE since Pt exhibits an excellent stability in acidic conditions while presenting very high HER activity. One of the strategies to reduce the cost of the catalyst is to use electrocatalytic supports, where nanoparticles (NPs) of Pt (or Pd, another active catalyst for HER) are spread. They should possess good resistance to corrosion, high conductivity, low cost and chemical stability with the loaded catalyst.[55] Carbon materials are the most commonly used as support at the cathode (but not for the anode since carbon can be easily oxidized into CO_2 at a low potential, 0.206 V vs RHE)[37, 56] and has a high electrochemical surface area.[57] Therefore, Pt/C is the state-of-art cathode material, where the loading of the NM is dispersed on the active phase (support) on gas diffusion electrodes on carbon nanotubes,[58] graphene [59-61] or carbon black (Figure 1.7).[62]

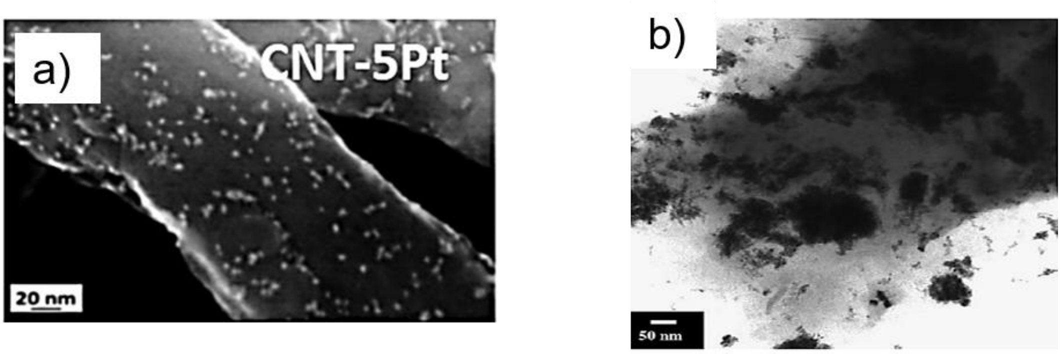

Figure 1.7. a) SEM image of CNT/Pt composite loaded with 5 wt% (taken from [63]) and b) TEM image of Pt/Vulcan carbon catalyst (taken from [56]).

It has been reported that Pt/C at low loadings (0.5-1 mg_{Pt} cm^{-2})[64, 65] reached current densities around 1 A cm^{-2} or more at very low overpotential (ca. 50 mV)[16, 66, 67] while operating at temperatures in the range of 70-80 °C. However, carbon-based supports used at the cathode usually present poor electrochemical stability on their own, then in order to be used as catalyst support they must be activated either chemically (oxidative pre-treatment by HNO_3, H_2O_2, O_2 or O_3) or physically (thermal treatment under inert atmosphere at 800-1100 °C or in air at 400-500 °C) to ensure good dispersion of the metal and catalytic activity.[55, 68] Therefore, modifications and the used of different synthesis routes to produce new structures or enhancing interactions between the substrate and the NM has been center of focused recently. Among these, graphite spheres [69] and nanofibers [70, 71] (CNF) have reported an increase in stability due to the hollow structure that allows a “confinement” of the NPs and favorable interaction of the alloy PdNi-CNF.[72] Also, core-shell catalysts, where a transition metal is the core and a Pt or Pd works as the shell, have resulted in an increase of the electrocatalytic efficiency due to the tunable properties of this technique to control the NM thickness(Figure 1.8). [73-75]

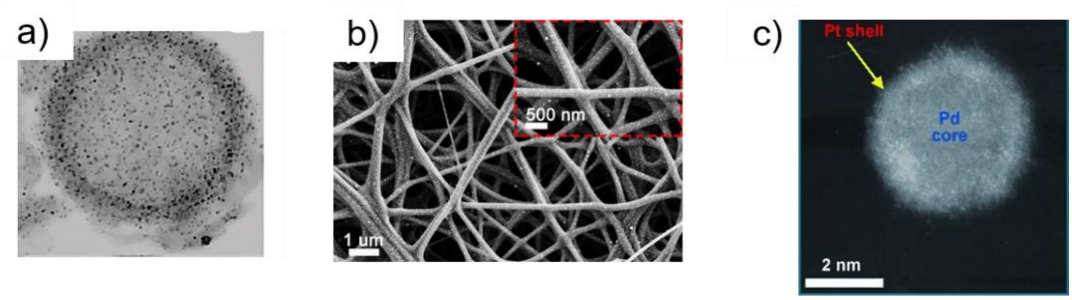

Figure 1.8. Different morphologies on carbon-based support a) TEM image of Pt@HGS (taken from[69]), b) SEM image of Pd/CNFs (taken from[72]) and c) HAADF image of Pt monolayer shell on Pd core-NPs (taken from [73])

Different route of synthesis such as chemical vapor deposition (CVD),[76-78] reactive spray deposition technology (RSDT),[57, 79] physical vapor deposition (PVD) [80, 81] and others have been used to tune properties on the carbon-based supports. Overall, the most promising morphology light be graphene. On its own it possesses unique properties (low resistivity, microporous structure) that can offer high surface area (~64 m^2 g_{Pt}) such as the Pt/rGO (reduced graphene oxide) and an improve in stability while testing the oxygen reduction reaction (ORR).[76, 82-84] Despite all these advances on the carbon support, it is still necessary to make more cost-effective the HER, leading to a research on earth-abundant materials.

c) Non-noble metals (Non-NMs) electrocatalysts

Sulfides, carbides, phosphides, oxides and nitrides composed of earth-abundant metals, usually named transition metal catalyst (TMC), haven been proposed as promising alternatives to platinum as HER electrocatalysts (Figure 1.9).[31] Sulfides, such as MoS_x-based more precisely MoS_2, exhibit a relatively high activity (overpotential in the range of 100-180 mV)[85] but still low compared to platinum catalysts. Also, molybdenum its higher in abundance compared to platinum, 1.2 ppm versus the 0.01 ppm of the earth's crustal rocks,[86, 87] respectively. This abundance makes MoS_x-based a promising option, with numerous morphological arrangements such as NPs,[88, 89] films,[90, 91] sheets [92] and composites.[93-95] However, these materials still present poor stability, but it has been demonstrated that by enhancing the active sites on the nanostructures, mentioned previously, is possible to surpass that throwback.[96]

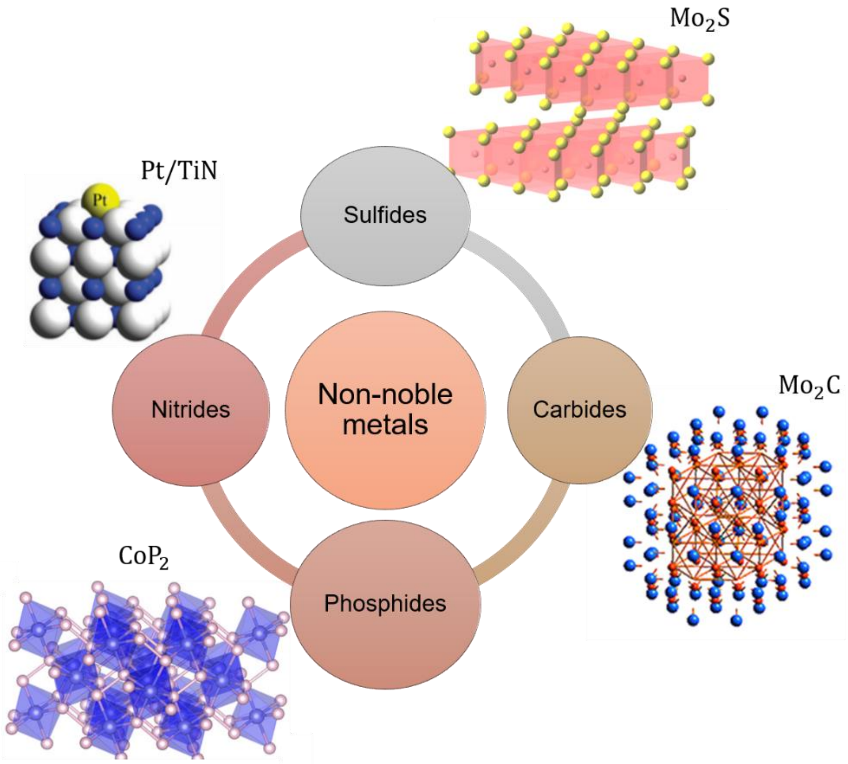

Figure 1.9. Different crystal structures of Non-NMs electrocatalysts. Crystal structures of Mo_2S (taken from[97]), Mo_2C (taken from[98]), CoP_2 (taken from[99]) and Pt/TiN (taken from[100]).

On the other hand, carbides (TMCs, transitional metal carbides) are formed by adding carbon atoms into the transitional metals interstitial sites such as Mo,[101] W,[31] Ti [102, 103] and others.[104] They present a high resistance to corrosion (ionic interaction), strong interaction with NMs (high conductivity due to the metallic interaction) and suitable adsorption properties (covalent interactions).[55, 102] Therefore, they are often use as a support for Pt-NPs like WC hollow spheres,[105, 106] Tl_3C_2 nanowires [107] or Mo_2C nanotubes.[108] The latter, as in the sulfide series, stands out among the carbides due to its d-band electronic structure which is like the platinum one. Therefore, the adjustable electronic structure makes it an attractive approach for HER catalysts.[109] Other common carbides are WC and Cr_3C_2, and both have reported good HER activity.[110] Furthermore, Ti carbide has attracted attention for possessing a conductivity in the range of 300-800 S m^{-1} and better corrosion resistance compared to other carbides (i.e., WC) in the potential window for HER (potential window between 0.8 V to 1 V vs SHE).[111]

However, more investigation is needed in terms of synthesis for expanding its applicability.[55, 102, 112]

Additionally to the TiC, among the transitional metal nitrides titanium nitride (TiN) has become a well-known supporting material, and its best performance is exhibited in the nanofiber morphology.[113] The graphite carbon nitride, because of its graphene like structure and large number of active binding sites, is suitable for the dispersion of Pt-NPs.[114] Recently, among the nitrides mesoporous materials, Pd/$NiCo_2S_4$ and NiMo nanosheets have improved the exposure of active sites enhancing the electrocatalytic HER with reasonable overpotentials (~70-90 mV) and small Tafel slopes (70 mV dec^{-1} and 35 mV dec^{-1}, respectively).[115, 116] Lastly, phosphide ions have brought interesting electron transfer kinetic contribution when coupled to transition metals like Fe, Co, Ni and Mn.[117, 118] Fe_xP and NiP phosphides exhibit sites with great affinity for proton adsorption.[119-121] Moreover, metal alloys phosphides are presenting low metal dissolution in acid solution and excellent corrosion resistance.[67, 122]

1.3.2.3. Anode for oxygen evolution reaction (OER)

a) Oxygen evolution reaction (OER)

Opposite to HER, the oxygen evolution reaction (OER) is more complex with four electron-proton coupled reactions that makes the kinetics much slower than the HER. It requires higher driving force to surpass the energy barriers with larger overpotentials to drive the O_2 evolution (Eq. 1-2). Several reaction mechanisms have been proposed,[123] but overall the OER reaction in acidic solution follows the oxidation of two water molecules to produce one of oxygen molecule through four electron-proton coupled steps (Figure 1.10).[123-126]

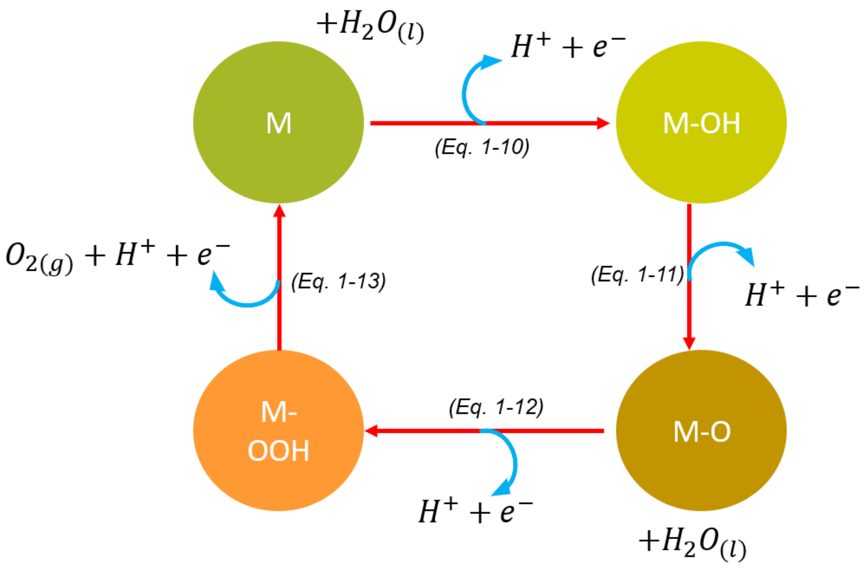

Figure 1.10. OER mechanism in acidic conditions (blue arrows) with peroxide intermediates (red arrows).

The equations mechanism that follows Figure 1.10 are based on metal oxide (MO$_x$):[123, 124, 126-129]

$$M + H_2O_{(l)} \rightarrow MOH + (H^+ + e^-) \qquad \textit{(Eq. 1-10)}$$

$$MOH \rightarrow MO + (H^+ + e^-) \qquad \textit{(Eq. 1-11)}$$

$$MO + H_2O_{(l)} \rightarrow MOOH + (H^+ + e^-) \qquad \textit{(Eq. 1-12)}$$

$$MOOH \rightarrow O_{2(g)} + M + (H^+ + e^-) \qquad \textit{(Eq. 1-13)}$$

The first step (Eq. 1-10) is the formation of absorbed $^{\bullet}$OH species at the surface of M, then this metal-hydroxide follows a further oxidation (proton-electron coupling) to form an oxo species (Eq. 1-11). On Eq. 1-12, a nucleophilic attack by another water molecule leads to the hydroperoxide intermediate (MOOH), which then releases an oxygen molecule to regenerate the initial M active site (Eq. 1-13).[126, 129] The major difference among the different mechanisms proposed is on the last step, the formation of molecular oxygen. MO produced at Eq. 1-11, can undergo a different route to form O_2 by the combination of two MO molecules (Eq. 1-14).[124, 127]

$$2MO \rightarrow 2M + O_{2(g)} \qquad \textit{(Eq. 1-14)}$$

Despite the differences mentioned above, for a general electrocatalytic ability it has been established that the formation of the intermediates M-O, M-OH and M-OOH are crucial for the electrocatalysis of OER.[124, 127, 129] Moreover, the mechanism is strongly dependent on the nature of catalyst, therefore creating a universal mechanism for the different types of electrocatalyst is challenging.

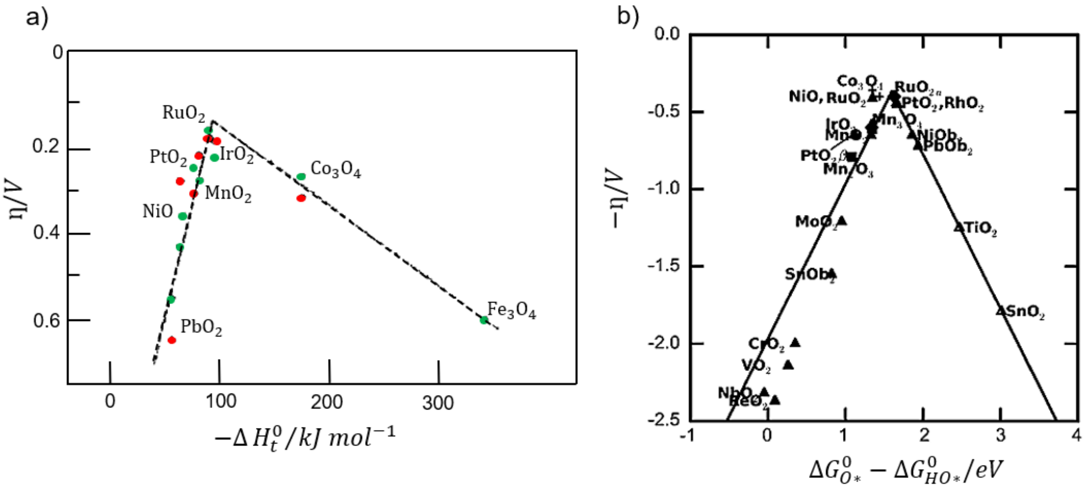

Figure 1.11. a) Volcano shaped curve for the OER activity of different oxides as function of their enthalpy (modified from[130]) and b) activity trends towards the OER for rutile and anatase oxides (taken from[131]).

However, Trasatti associated the overpotential with the change of enthalpy of the lower to higher oxide of the intermediates giving a volcano shaped curve as a useful tool with predictive character (Figure 1.11a)[130] or a recent one of *Isabela et al.,*[131] based on rutile and anatase phases from different oxides (Figure 1.11b). As observed in Figure 1.11, metal oxides such as RuO_2 and IrO_2 are the ones presenting the lowest overpotential (100-200 mV) to drive a current density of 10 mA cm^{-2} (η_{10} = overpotential at 10 mA cm^{-2}), since their oxidation potential are close to the oxygen evolution equilibrium potential.[131, 132] Figure 1.12 presents how OER electrocatalyst can be classified nowadays such as alloys, diversification in morphology, mixture of oxides, low-cost transitions metals (TMs) and others.

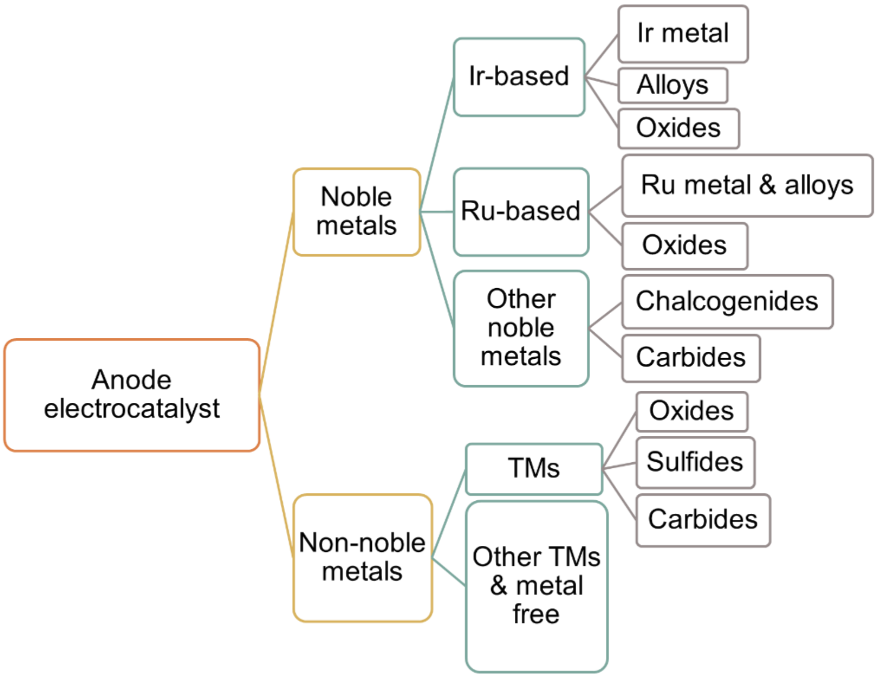

Figure 1.12. Classification of OER electrocatalyst materials based on metal content.

b) *Noble metals (NMs) electrocatalyst*

IrO_2 and RuO_2 are the establish oxides for OER catalysts due to their electron conductivity and acceptable stability towards the corrosion from the acidic conditions of the membrane.[5, 133, 134]

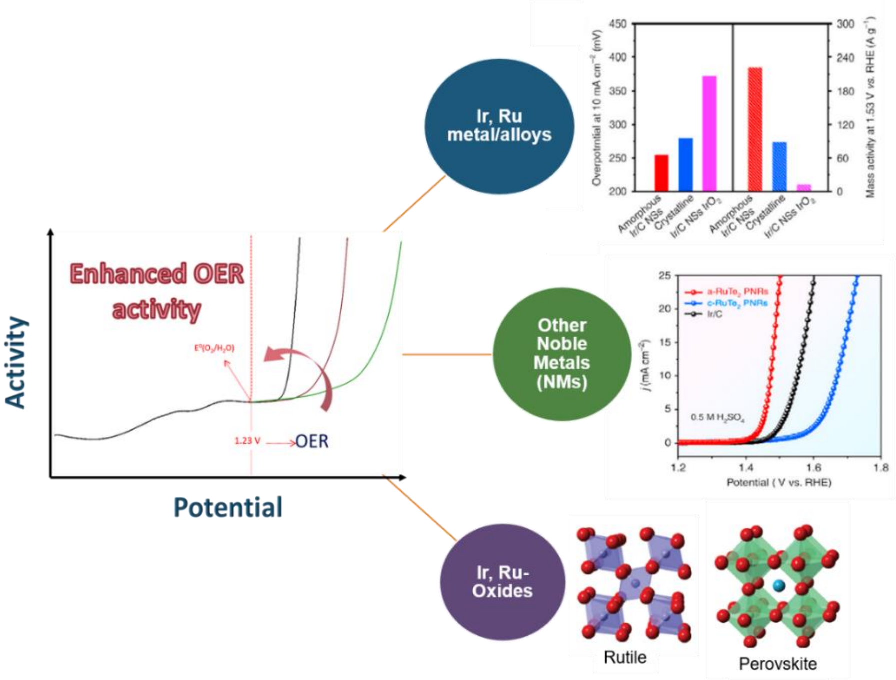

Figure 1.13. Strategies towards NMs based catalysts for OER.

On the other hand, Pd, Rh and Pt have shown high performances due to their structural durability,[134-136] but to date Ir and Ru are the most extensively studied in a variation of arrangements such as metal/alloys and oxides (Figure 1.13). Moreover, recent advances have been undertaken towards crystal structure/morphology to tune the properties as well as to the increase the surface area to enhance the catalytic activity in order to reduce the cost of the catalysts in the MEA.[31, 67, 125]

Iridium based materials. Diverse iridium metal/alloys and oxides have been developed for OER, since iridium offers an excellent compromise between activity and durability under strong acidic conditions. Ir-metal nanomaterials can work under harsh conditions, and in order to take advantage of the stability and activity that it offers a variety of strategies have been developed. For instance, the control of the size and the morphology as well as the elaboration of heterostructures with other electroactive nanomaterials (synergic effects).[137, 138] Ir-NPs such as IrFe-NPs (Figure 1.14a) have shown an η_{10} = 240-290 mV for 12h, probably thanks to the different sizes of Ir atoms dispersed that are protected by the structure that helps as well to protect Fe-Ir from oxidation, resulting in durable catalysts in harsh catalytic conditions.[139] A similar approach has been done with nickel in the form of Ir-NiO with an η_{10} = 215 mV as a results of the synergic effect of the excess electrons of iridium on the surface of NiO.[140] By improving the dispersion of the metal, the size of the metal can also be controlled. For this, supports such graphene,[141, 142] nanotubes,[143, 144] nanobowls,[145] silica,[146] and others [94, 147] are used to confine the particle size as well as to increase the surface area.[148] Moreover, Ir-metal hybrids have been elaborated with transition metals such as cobalt [149] in the form of nitrides [150] and hydroxides.[151] The metallic cobalt nitride interaction with the Ir NPs enhances the OER performance.

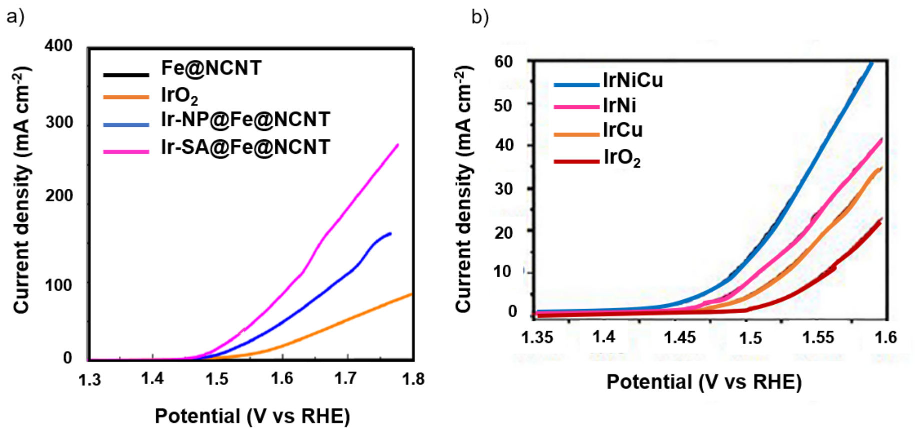

Figure 1.14. a) OER performance of commercial IrO_2 and Ir-Fe NPs tested in O_2 purged 0.5 mol L^{-1} H_2SO_4 solution (taken and modified from[139]) and b) LSV curves for OER performance of Ir-Ni alloys in N_2-saturated 0.5 mol L^{-1} H_2SO_4 solution at 5 mV s^{-1} (taken and modified from[152])

Alloying with NMs (i.e., Pt, Ru) by using synergetic effects, and transition metals (i.e., Ni, Co, Fe, Cu, Mn, Te, Cr) thanks to their 3d electronic structure, have proven to be a way to minimize the amount of iridium loading. Among the Ir-NMs alloys, Ir-Pd [153, 154] and Ir-Ru [8, 155] present the most favorable mix with design shapes that exposes active sites and surface configurations such as nanowires, nano-hollow spheres and nanocubes, where electron transfer between the metals allowed to lower the energy barriers of the OER.[153] Other alloys, such as Ir-Rh are presenting a higher mass activity than pure Ir-NPs,[156] and Ir_6Ag_9 NTs/C did not present any obvious potential change within 6 h of operating at 5 mA cm^{-2} and can reach low overpotential of η_{10} = 285 mV.[157] Despite these advances, if the use of Ir-NMs is still desirable, is crucial to maximize the efficiency of the NMs with mixture of TMs like IrRuMn,[158] IrRu@Te,[159] M-RuIr (M = Co, Ni, Fe),[160] and NiIrRuAl.[161] TMs are weakening the adsorption and desorption of oxygen intermediates (-OH, -O and -OOH), therefore enhancing the OER[152, 162] as observed in Figure 1.14b. Besides element composition, different nanostructures (i.e., nanocages,[163] nanowires,[164] and nanocrystals [165]) of Ir-TMs are playing a role in the catalytic activity, especially regarding anticorrosion properties due to the species that are produced at the surface or the grain boundaries of these structures.[166]

Additional to the synergetic effects and electronic structure, the crystal structure plays a crucial role in the activity and durability of iridium oxides. The latter changes from one to another due to the variations in crystal structure as compared with the state-of-art catalyst, rutile IrO_2. This crystalline form, despite of having a lower catalytic activity compared to its counterpart, amorphous IrO_2, is more stable in terms of iridium dissolution. Therefore, morphology plays a key role in introducing metals into the rutile structure to enhance the efficiency such as noble metal Ru (i.e., $Ru_{0.5}Ir_{0.5}O_2$,[5] $Ir_{0.7}Ru_{0.3}O_2$ [133]) and low-cost TMs like Cr,[167] Mn,[168-170] Co,[10] Fe,[171] and Mo.[17] The common characteristic among them is the porosity achieved, thanks to the route of synthesis such as spray-drying (Figure 1.15b) and spray pyrolysis. To date, 1D nanotubes/nanowires, 3D and hierarchical structures are the morphologies that exhibit abundant active sites and good structural stability. To achieved this, knowing which TM is less stable (low resistance to corrosion) enables building a structure that protects it and at the same time allows the efficient OER activity.[162, 172, 173]

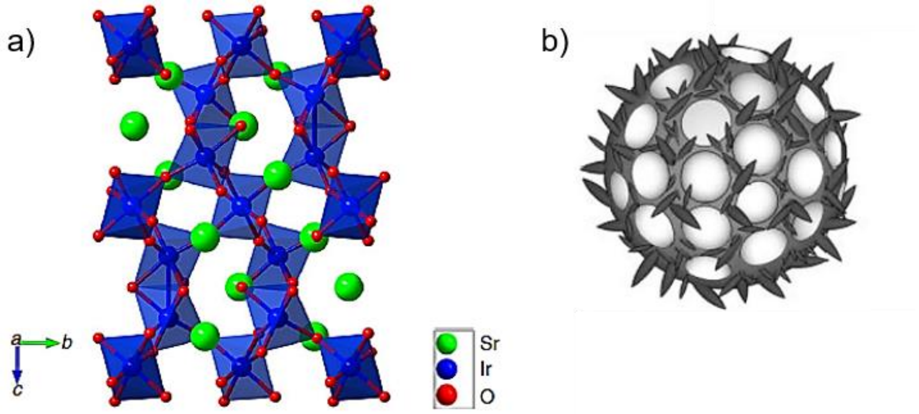

Figure 1.15. a) Perovskite structure of 6H-$SrIrO_3$ (taken from[174]) and b) schematic representation of the hierarchical structure obtained by spray-drying (taken from[175])

On the other hand, Ir-based perovskites [176, 177] are a good approach to reduce iridium loading since it is possible to make full or partial substitutions of the cations thanks to the flexibility that IrO_6 offers. Overpotentials around η_{10} = 250-270 mV have been reported for perovskites $SrIrO_3$[174] (Figure 1.15a), and double layered Ba_2PrIrO_6.[176] Moreover, as mentioned above, amorphous IrO_x does present higher catalytic activity than the crystalline rutile IrO_2. This is due to random oriented bonds and flexible structures that makes it easier to get oxidized during OER, in addition to the large electrochemical surface area and electrolyte-electrocatalyst interface [178] (i.e., perovskite-like catalysts[179]). Overall, previous results can lead to more ideas to design better catalysts or enhance the recent ones to be more active electrocatalysts. However, a better understanding of the porosity, the chemical composition, the surface area and the atomic arrangements needs to be investigated for Ir-based materials.

Ruthenium based materials. As iridium, ruthenium is one of the rare metals, but with 0.0004 ppm of the earth's crust [180] vs the 0.00003 ppm for iridium,[181] it is considered to have slightly more abundant reserves. Ruthenium is known for its activity but low stability towards OER as compared to iridium.[182] Based on that low stability, investigations towards Ru-based catalysts has move towards better durability with high catalytic activity preserved. Single ruthenium metal with oxygen-free coordination has been proposed to reduce dissolution in acidic media, such as Ru1-N4 with a nitrogen-carbon support and Ru1-Pt3Cu, both reported with low overpotentials (η_{10} = 267 mV and 220 mV, respectively). Since then, theoretical calculations provided a coordination strategy for high OER performances (Figure 1.16).[183, 184] As in Ir-based catalysts, the use of alloying is employed as an approach for Ru-based catalysts to provide higher stability. Ternary alloys like Pt-Pd-Ru[185] showed a low dissolution of the metals in acidic media as compared to the metallic form of Ru. Binary alloys such as Ru-M (M = Pd, Cu, Ir, Co, Cr, Ni, Re), in particular $Ru_{60}Co_{40}$ mixed phase exhibited an improved catalytic activity (203 mA mg_{Ru}^{-1}) versus the pure Ru NPs (100 mA mg_{Ru}^{-1}).[186]

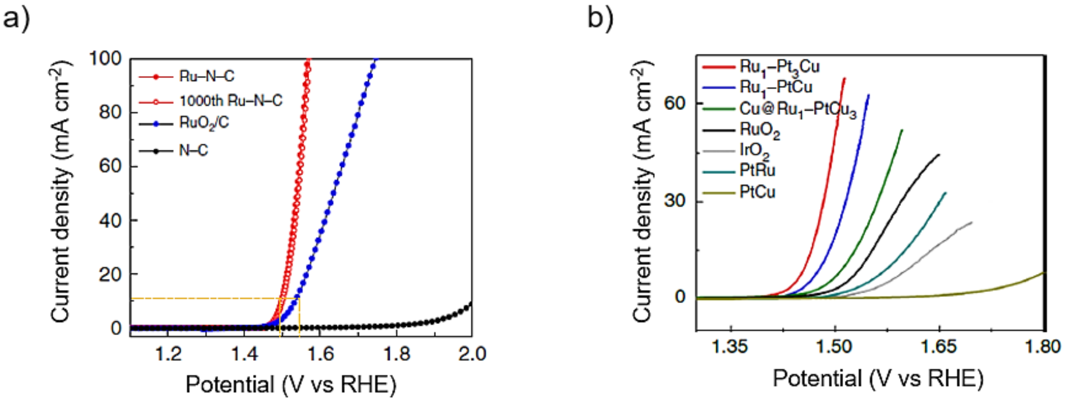

Figure 1.16. OER performance of a) Ru-N-C in 0.5 mol L^{-1} H_2SO_4 electrolyte (taken from[183]) and b) Ru_1-Pt_3Cu in O_2-saturted 0.1 M $HClO_4$ solution (taken from[184]).

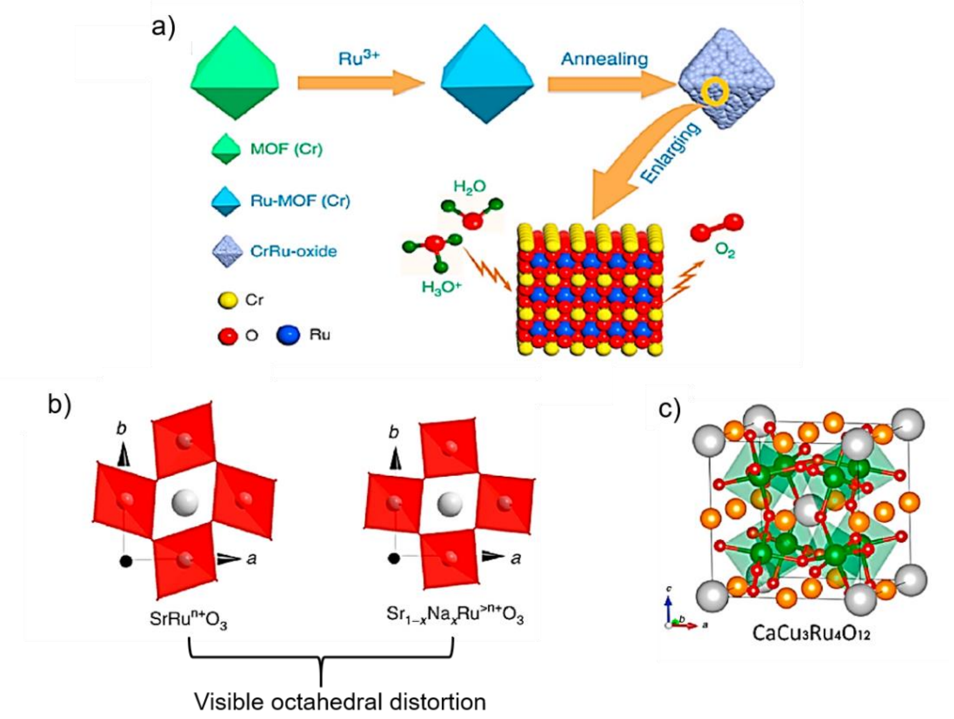

Figure 1.17. Doping strategies of a) chromium-ruthenium electrocatalyst preparation (taken from[187]); b) octahedral distortion by sodium doping (taken from[188]); c) crystal structure representation of the perovskite $CaCu_3Ru_4O_{12}$ (taken from[189])

The favorable binding energy of ruthenium oxides towards the OER intermediates (-OH, -O and -OOH), results in high OER activity. As mentioned previously, the properties that rutile and perovskite oxides present in iridium are also favorer with ruthenium. Rutile RuO_2 performances depend on the synthesis method. This is exemplified with mesoporous RuO_2 which presents an η_{10} = 266 mV when synthesized by nano replication (a mesoporous silica template is used for then being impregnated with the metal oxide, which is later removed by wet-etching process),[190] while the one synthesized by Adams method (fusion of the metal chloride precursor with $NaNO_3$ in air at elevated temperatures)[191] shows η_{10} = 326 mV.[192] In addition, improved strategies as deposition of the catalyst such as films,[193-195] and morphologies such as hollow porous structures,[196] have reported that based on the orientation of the film like *Roy et al.,*[193] (i.e., (100), (001), (101), and (111) orientations) it is possible to control the corrosion of the oxide, and *Su et al.,*[196] by creating defects on the structure by doping while controlling the morphology, more active sites can be obtained. This latter has attracted attention and the doping with different TMs such Cu,[196] Mn,[197] Co,[198] and Cr [187] have improved the catalytic performances due to the electronic structure as well as the doping induced defects that generate oxygen vacancies (Figure 1.17a). These vacancies can also be generated in perovskites oxides, among them $SrRuO_3$ [188] with Na doping (Figure 1.17b) and $CaCu_3Ru_4O_{12}$ (Figure 1.17c).[189] These materials are showing better structural stability as well as the influence of displaced of the d-band center that optimizes the binding energies towards the reaction intermediates. In addition to these advances, more efforts are needed to develop nanostructures with beneficial chemical components with rutile and perovskite oxides.

Other NMs. Ir- and Ru-based catalysts are the most studied, but other NMs arrangements present high performance for OER, such as NMs chalcogenides. Those materials are bringing unique structures with a good number of vacancies like Li-$IrSe_2$,[199] where the ion intercalation between lithium, iridium and selenium provide a high porosity material resulting in an overpotential of η_{10} = 180 mV. Also, amorphous chalcogenides with favored electronic properties that enhances the electron-transfer have shown reasonable OER activity.[200] Moreover, Pt- and Rh-based catalysts have been proposed such as RhCu nanotubes and PtNi/CNFs with overpotentials around η_{10} = 300-400 mV.[201, 202] These examples are showing that other NMs can be promising candidates and more research is encouraged to design materials in this field.

c) Non noble metal (Non-NMs) materials

Noble metal free electrocatalysts have attracted attention towards OER with the aim of developing catalysts based on earth abundant elements like Mn, Fe, Co and Ni.

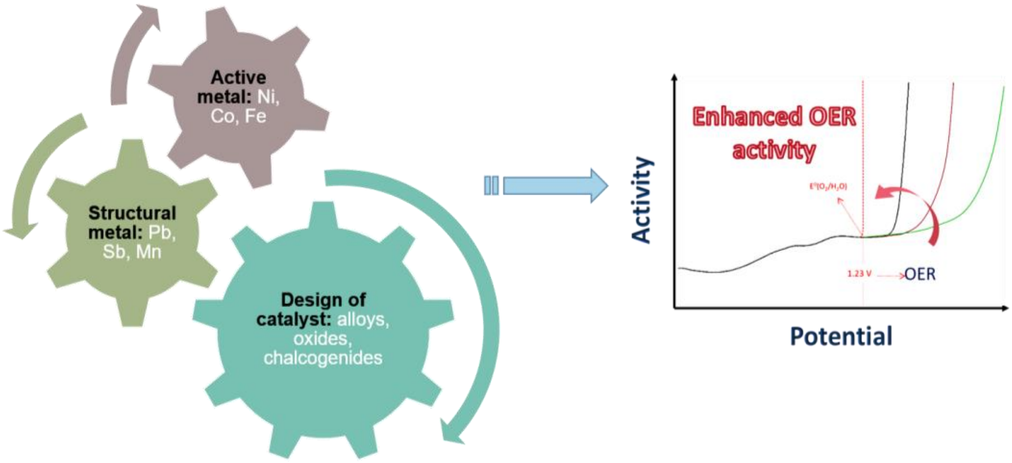

Figure 1.18. Schematic representation of how non-precious metals combine with design strategies result in efficient OER catalyst.

However, most of them are unstable under OER conditions (high oxidative potentials) and in order to surpass this challenge research has moved towards the design of the catalysts in the form of alloys, oxides, chalcogenides and others (Figure 1.18).[126, 203]

Transition metals (TMs). Different route of synthesis, designs, and characterizations have been used to study electrocatalytic performances of TMs. These catalysts can be classified as well by alloys/metals, single metal or mixed metal oxides, hydroxides, chalcogenides and phosphides.[204] The affordable price of TMs oxides makes single metal or mixed oxides very attractive materials. Their stability properties and tunable structures can be modulated by controlling the morphology, the composition and the electronic structure, usually using doping strategies.

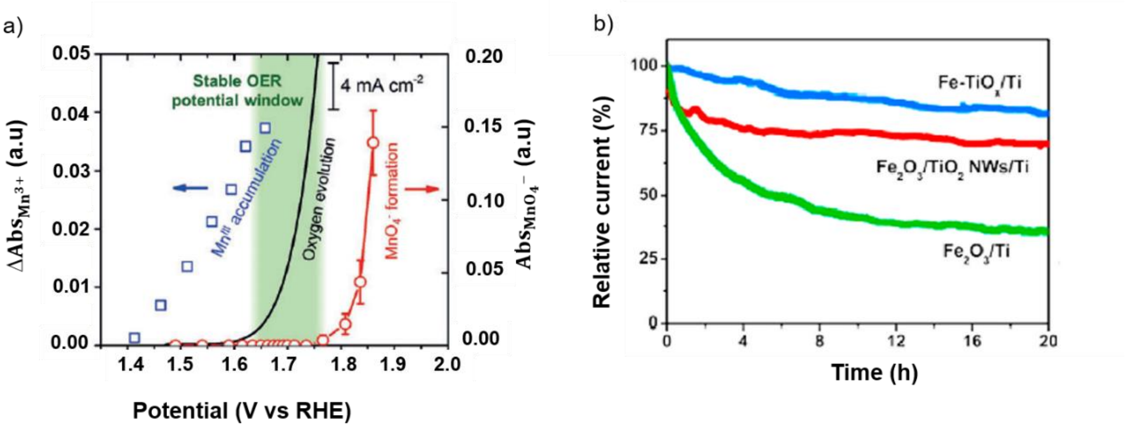

Figure 1.19. a) Potential dependence of Mn^{3+} accumulation (blue squares), OER current (black line), and MnO_4^- generation (red circles) (taken and modified from[205]) and b) chronoamperometry of Fe-TiO_x LNWs/Ti vs SCE for 20h (taken from[206]).

Single metal oxides such MO_x (M = Mn, Fe, Co and Ni) have resistant corrosion properties and very good OER activity in acid media. Among them MnO_x is the most stable one in acid electrolytes due to its metal-oxygen bond strength, and is also the most studied due to the different existing oxidation states and crystal structures.[207] Among the MnO_2 crystal structures α-MnO_2 presents a high activity between the four polymorphs.[208] Based on this, studies have reported the change of induced phase transformation from δ-MnO_2 to α-MnO_2.[207] However, the main issue is the formation of $\mathrm{MnO_4^-}$ so research nowadays has moved toward stabilizing the oxide more precisely the stabilization of Mn^{3+} (Figure 1.19a).[205] As the stability decreases as the first row of TMs advances, then it is expected that Co/Fe oxides activity in acidic conditions decreases. However, elaborated designs of these oxides have shown promising catalytic performance, which is the case for CoO_x supported on FTO (fluorine-doped tin oxide),[209] CP (carbon paper),[210] and NPs,[211] where the strong interfacial and formation of oxygen vacancies act as active sites (CoO_x/NPs showed a η_{10} = 295 mV). On the other hand, iron oxides are not widely studied since they dissolve rapidly in OER conditions. Few studies are focusing on improving these oxides by either doping or using hybridization. For instance, $Co_xFe_{1-x}O_y$ [212] with 5% Co-doping showed a balanced catalytic activity and a durability up to 50 h at 10 mA cm^{-2}, and Fe-TiO_x

LNWs/Ti [206] presented as well a stable current density for 20 h with only a decrease of 18.7% in activity (Figure 1.19b).

The above results open an insight into mixed oxides in the idea of taking advantage of the acid stable TMs oxides such as MnO_x, PbO_x and SbO_x, and active compounds CoO_x and FeO_x in acid conditions. In this regard, binary and ternary oxides are design such as cobalt and manganese doping in Sb_2O_6 [213] and $CoFePbO_x$ [214] showed a negligible change in potential for 24 h to 50 h while maintaining a current density of 10 mA cm^{-2} and 1 mA cm^{-2}, respectively. Nevertheless, high overpotentials are still needed to achieve such activities. Another interestingly combination is $Ni_xMn_{1-x}Sb_{1.6-1.8}O_y$, since antimony offers a great thermodynamic stability , manganese provides structural stability and nickel offers active surface to enhanced OER, reporting a negligible increase in overpotential during 150 h at 10 mA cm^{-2}. [215] Moreover, cubic perovskites oxides such as $CaCoO_3$ and $SrCoO_3$, and the double perovskite $LaFe_xNi_{1-x}O_3$ (LFNO) showed to be good catalysts for OER. The first one due to its smaller lattice constant, and LFNO for its increased in surface area and strong interaction Ni-O.[203]

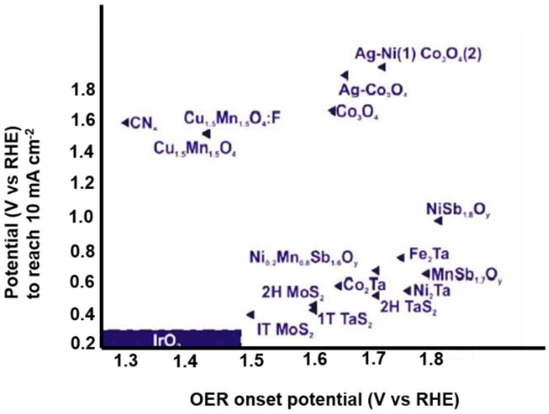

Figure 1.20. Overview of OER onset potential or potential required to reach 10 mA cm^{-2} of Non-NMs catalysts in comparison with IrO_2 (taken and modified from[67]).

Furthermore, the incorporation of anions to manipulate the electronic structure can result in excellent electrochemical properties, therefore TMs sulfides and phosphides have emerged as electrocatalysts for OER. Some advances in this area have been made with Co_3S_4/NPs,[216] Co-doped MoS_2,[217] $NiAl_\delta P$,[218] and amorphous NiFeP.[219] In addition to the above non-NMs based catalyst, other earth abundant compounds can be found, such as polyoxometalates, Prussian blue analogues and TMs-nitrogen-carbon moieties.[124-126, 203, 204] Overall, the catalytic performances of these non-NMs catalysts are still inferior to the NM-based catalysts, and more efforts are needed to enhance the catalytic activity and stability by surface, compositional, and structural engineering. A resume is presented in Figure 1.20.

1.4. Conclusion and objectives of PhD thesis

This chapter has provided an insight into proton exchange membrane water electrolyzer function principle, main reaction mechanisms and electrocatalysts currently used for HER and OER. One of the main obstacles highlighted for PEMWE is for the anodic part where the OER takes place, from which major energy losses are observed. In addition, the high-cost of the state-of-art anode electrocatalyst, iridium, as well as the complexity mechanism of OER makes the development of these devices limited when considering a large-scale use of those devices.

Generally, to improve the electrocatalyst or reduce its loading, two approaches are largely used: increasing the intrinsic activity or increasing the number of active sites by enhancing the surface area. This has been proven to be possible with low-cost abundant earth metals that by a well-designed catalyst favorable OER performance can be achievable, such as the case of molybdenum as a hybrid composite in IrO_2-MoO_3.[17] Considering the latter, this thesis focuses on the electrochemical characterization of amorphous and crystalline Ir-Mo electrocatalysts, with the aim to enhance the OER with reduced iridium content. The underlying idea is indeed the use of a material able to work at very high current density under high pressures while operating, with a specific porous morphology that will promote water and gas transport. The above bibliographic analysis serves as a basis for preparing possibly new materials, expecting that they have electrocatalytic properties suitable to be used as an electrode material at the anode in PEMWE.

Therefore, to carry out this, the following objectives were implemented by taking into account the achievements reported in the literature for alternative catalysts:

- ✓ Study the influence of the synthesis technique to produce porous catalyst compositions.
- ✓ Study the impact of the catalyst composition during OER activity and stability by cyclic voltametric and chronoamperometry.
- ✓ Study the underpotential deposition of metals as a technique to measure the electrochemical surface area, with the aim to observe the influence of the catalyst content to enhance the specific surface area in order to maximize the activity by lowering the metal.

1.5. References

1. Carmo, M., et al., A comprehensive review on PEM water electrolysis. *Int. J. Hydrogen Energy*, 2013, *38* (12), 4901-4934.
2. Bessarabov, D., et al., *PEM electrolysis for hydrogen production: principles and applications*. CRC Press: Boca Raton, FL, 2016; p 389.
3. Maric, R.; Yu, H., Proton Exchange Membrane Water Electrolysis as a Promising Technology for Hydrogen Production and Energy Storage. 2019.
4. Siracusano, S., et al., Performance of a PEM water electrolyser combining an IrRu-oxide anode electrocatalyst and a short-side chain Aquivion membrane. *Int. J. Hydrogen Energy*, 2015, *40* (42), 14430-14435.
5. Siracusano, S., et al., Nanosized IrO_x and $IrRuO_x$ electrocatalysts for the O_2 evolution reaction in PEM water electrolysers. *Appl. Catal. B: Environmental*, 2015, *164*, 488-495.
6. Audichon, T., et al., Electroactivity of RuO_2-IrO_2 mixed nanocatalysts toward the oxygen evolution reaction in a water electrolyzer supplied by a solar profile. *Int. J. Hydrogen Energy*, 2014, *39* (30), 16785-16796.
7. Koetz, R.; Stucki, S., Stabilization of ruthenium dioxide by iridium dioxide for anodic oxygen evolution in acid media. *Electrochim. Acta*, 1986, *31* (10), 1311-16.
8. Koetz, R.; Stucki, S., Oxygen evolution and corrosion on ruthenium-iridium alloys. *J. Electrochem. Soc.*, 1985, *132* (1), 103-7.
9. González-Huerta, R. G., et al., Oxygen evolution in Co-doped RuO_2 and IrO_2: Experimental and theoretical insights to diminish electrolysis overpotential. *J. Power Sources*, 2014, *268*, 69-76.
10. Corona-Guinto, J. L., et al., Performance of a PEM electrolyzer using $RuIrCoO_x$ electrocatalysts for the oxygen evolution electrode. *Int. J. Hydrogen Energy*, 2013, *38* (28), 12667-12673.
11. Jirkovsky, J., et al., Particle size dependence of oxygen evolution reaction on nanocrystalline RuO_2 and $Ru_{0.8}Co_{0.2}O_{2-x}$. *Electrochem. Commun.*, 2006, *8* (9), 1417-1422.
12. Sun, W., et al., Hollandite Structure $K_{x\approx0.25}IrO_2$ Catalyst with Highly Efficient Oxygen Evolution Reaction. *ACS Appl. Mater. Interfaces*, 2016, *8* (1), 820-826.
13. Sardar, K., et al., Bismuth Iridium Oxide Oxygen Evolution Catalyst from Hydrothermal Synthesis. *Chem. Mater.*, 2012, *24* (21), 4192-4200.
14. A. Marshall, et al., Electrochemical characterisation of $Ir_xSn_{1-x}O_2$ powders as oxygen evolution electrocatalysts. *Electrochim. Acta*, 2006, *51*, 3161-3167.

15. Marshall, A. T., et al., Performance of a PEM water electrolysis cell using $Ir_xRu_yTa_zO_2$ electrocatalysts for the oxygen evolution electrode. *Int. J. Hydrogen Energy*, 2007, *32* (13), 2320-2324.
16. Neyerlin, K. C., et al., Combinatorial Study of High-Surface-Area Binary and Ternary Electrocatalysts for the Oxygen Evolution Reaction. *J. Electrochem. Soc.*, 2009, *156* (3), B363-B369.
17. Tariq, M., et al., Unraveling the Beneficial Electrochemistry of IrO_2/MoO_3 Hybrid as a Highly Stable and Efficient OER Catalyst. *ACS Sustain. Chem. Eng.*, 2018, *6* (4), 4854–4862.
18. Gallo, A. B., et al., Energy storage in the energy transition context: A technology review. *Renew. Sustain. Energy Rev.*, 2016, *65*, 800-822.
19. IEA *Renewables 2020* International Energy Agency: 2020.
20. Aneke, M.; Wang, M., Energy storage technologies and real life applications – A state of the art review. *Applied Energy*, 2016, *179*, 350-377.
21. IEA *Global Energy Review 2019*; International Energy Agency: 2019.
22. Shiva Kumar, S.; Himabindu, V., Hydrogen production by PEM water electrolysis – A review. *Materials Science for Energy Technologies*, 2019, *2* (3), 442-454.
23. IRENA, *Hydrogen: a renewable energy perspective*. International Renewable Energy Agency: 2019.
24. Chi, J.; Yu, H., Water electrolysis based on renewable energy for hydrogen production. *Chinese J. Catal.*, 2018, *39* (3), 390-394.
25. Iain Staffell, et al., The role of hydrogen and fuel cells in the global energy system *Energy Environ. Sci.*, 2018.
26. Acar, C.; Dincer, I., Review and evaluation of hydrogen production options for better environment. *J. Clean. Prod.*, 2019, *218*, 835-849.
27. van Putten, R., et al., Fuelling the hydrogen economy: Scale-up of an integrated formic acid-to-power system. *Int. J. Hydrogen Energy*, 2019, *44* (53), 28533-28541.
28. Kaur, M.; Pal, K., Review on hydrogen storage materials and methods from an electrochemical viewpoint. *J. Energy Storage*, 2019, *23*, 234-249.
29. IRENA *Hydrogen: A renewable energy perspective* International Renewable Energy Agency: Abu Dhabi, 2019.
30. Liu, X., et al., Research progress and surface/interfacial regulation methods for electrophotocatalytic hydrogen production from water splitting. *Mater. Today Energy*, 2020, *18*.
31. Khan, M. A., et al., Recent Progresses in Electrocatalysts for Water Electrolysis. *Electrochem. Eng. Rev.*, 2018, *1* (4), 483-530.
32. Sapountzi, F. M., et al., Electrocatalysts for the generation of hydrogen, oxygen and synthesis gas. *Prog. Energy Combust. Sci.*, 2017, *58*, 1-35.
33. Grigoriev, S. A., et al., Current status, research trends, and challenges in water electrolysis science and technology. *Int. J. Hydrogen Energy*, 2020, *45* (49), 26036-26058.
34. Ahn, Y., et al., Optimizing the operating temperature for microbial electrolysis cell treating sewage sludge. *Int. J. Hydrogen Energy*, 2017, *42* (45), 27784-27791.
35. Zeng, K.; Zhang, D., Recent progress in alkaline water electrolysis for hydrogen production and applications. *Prog. Energy Combust. Sci.*, 2010, *36* (3), 307-326.
36. Leng, Y., et al., Solid-state water electrolysis with an alkaline membrane. *J. Am. Chem. Soc.*, 2012, *134* (22), 9054-7.
37. Feng, Q., et al., A review of proton exchange membrane water electrolysis on degradation mechanisms and mitigation strategies. *J. Power Sources*, 2017, *366*, 33-55.
38. Babic, U., et al., Critical Review—Identifying Critical Gaps for Polymer Electrolyte Water Electrolysis Development. *J. Electrochem. Soc.*, 2017, *164* (4), F387-F399.
39. Shirvanian, P.; van Berkel, F., Novel components in Proton Exchange Membrane (PEM) Water Electrolyzers (PEMWE): Status, challenges and future needs. A mini review. *Electrochem. Commun.*, 2020, *114*.

40. Hermann, A., et al., Bipolar plates for PEM fuel cells: A review. *Int. J. Hydrogen Energy*, 2005, *30* (12), 1297-1302.
41. Sun, X., et al., Earth-Abundant Electrocatalysts in Proton Exchange Membrane Electrolyzers. *Catalysts*, 2018, *8* (12), 657.
42. Kim, Y. S.; Pivovar, B. S., Chapter Four - Polymer Electrolyte Membranes for Direct Methanol Fuel Cells. In *Advances in Fuel Cells*, Zhao, T. S.; Kreuer, K. D.; Van Nguyen, T., Eds. Elsevier Science: 2007; Vol. 1, pp 187-234.
43. Kundu, S., et al., Mechanical properties of Nafion™ electrolyte membranes under hydrated conditions. *Polymer*, 2005, *46* (25), 11707-11715.
44. Goñi-Urtiaga, A., et al., Solid acids as electrolyte materials for proton exchange membrane (PEM) electrolysis: Review. *Int. J. Hydrogen Energy*, 2012, *37* (4), 3358-3372.
45. Ito, H., et al., Properties of Nafion membranes under PEM water electrolysis conditions. *Int. J. Hydrogen Energy*, 2011, *36* (17), 10527-10540.
46. Baglio, V., et al., Solid Polymer Electrolyte Water Electrolyser Based on Nafion-TiO_2Composite Membrane for High Temperature Operation. *Fuel Cells*, 2009, *9* (3), 247-252.
47. Antonucci, V., et al., High temperature operation of a composite membrane-based solid polymer electrolyte water electrolyser. *Electrochim. Acta*, 2008, *53* (24), 7350-7356.
48. Maiyalagan, T.; Pasupathi, S., Components for PEM Fuel Cells: An Overview. *Mater. Sci. Forum*, 2010, *657*, 143-189.
49. Siracusano, S., et al., An electrochemical study of a PEM stack for water electrolysis. *Int. J. Hydrogen Energy*, 2012, *37* (2), 1939-1946.
50. Antolini, E., Iridium As Catalyst and Cocatalyst for Oxygen Evolution/Reduction in Acidic Polymer Electrolyte Membrane Electrolyzers and Fuel Cells. *ACS Catal.*, 2014, *4* (5), 1426-1440.
51. Xu, D., et al., Earth-Abundant Oxygen Electrocatalysts for Alkaline Anion-Exchange-Membrane Water Electrolysis: Effects of Catalyst Conductivity and Comparison with Performance in Three-Electrode Cells. *ACS Catal.*, 2018, *9* (1), 7-15.
52. David, M., et al., Advances in alkaline water electrolyzers: A review. *J. Energy Storage*, 2019, *23*, 392-403.
53. Lasia, A., Mechanism and kinetics of the hydrogen evolution reaction. *Int. J. Hydrogen Energy*, 2019, *44* (36), 19484-19518.
54. Jayabal, S., et al., Understanding the high-electrocatalytic performance of two-dimensional MoS_2 nanosheets and their composite materials. *J. Mater. Chem. A*, 2017, *5* (47), 24540-24563.
55. Chalgin, A., et al., Effect of supporting materials on the electrocatalytic activity, stability and selectivity of noble metal-based catalysts for oxygen reduction and hydrogen evolution reactions. *Prog. Nat. Sci. Mat*, 2020, *30* (3), 289-297.
56. Grigoriev, S. A., et al., Evaluation of carbon-supported Pt and Pd nanoparticles for the hydrogen evolution reaction in PEM water electrolysers. *J. Power Sources*, 2008, *177* (2), 281-285.
57. Ayers, K. E., et al., Pathways to ultra-low platinum group metal catalyst loading in proton exchange membrane electrolyzers. *Catal. Today*, 2016, *262*, 121-132.
58. Chen, Z., et al., Supportless Pt and PtPd nanotubes as electrocatalysts for oxygen-reduction reactions. *Angew. Chem., Int. Ed.*, 2007, *46* (22), 4060-4063.
59. Xiao, H., et al., Electric field-assisted synthesis of Pt, carbon quantum dots-coloaded graphene hybrid for hydrogen evolution reaction. *J. Power Sources*, 2020, *451*.
60. Pushkarev, A. S., et al., Electrocatalytic layers modified by reduced graphene oxide for PEM fuel cells. *Int. J. Hydrogen Energy*, 2015, *40* (42), 14492-14497.
61. Nguyen, N.-A., et al., NiCoPt/graphene-dot nanosponge as a highly stable electrocatalyst for efficient hydrogen evolution reaction in acidic electrolyte. *J. Alloys Compd.*, 2020, *849*.

62. Zhang, Y., et al., Low content of Pt supported on Ni-MoC$_x$/carbon black as a highly durable and active electrocatalyst for methanol oxidation, oxygen reduction and hydrogen evolution reactions in acidic condition. *Appl. Surf. Sci.*, 2017, *412*, 327-334.
63. Mercado-Zúñiga, C., et al., Effect of Pt loading on the hydrogen production of CNT/Pt composites functionalized with carboxylic groups. *Int. J. Hydrogen Energy*, 2020, *45* (51), 27012-27025.
64. Giddey, S., et al., High purity oxygen production with a polymer electrolyte membrane electrolyser. *J. Membr. Sci.*, 2010, *346* (1), 227-232.
65. Badwal, S. P. S., et al., Hydrogen and oxygen generation with polymer electrolyte membrane (PEM)-based electrolytic technology. *Ionics*, 2006, *12* (1), 7-14.
66. Neyerlin, K. C., et al., Study of the Exchange Current Density for the Hydrogen Oxidation and Evolution Reactions. *J. Electrochem. Soc.*, 2007, *154* (7).
67. Hughes, J. P., et al., Polymer electrolyte electrolysis: A review of the activity and stability of non-precious metal hydrogen evolution reaction and oxygen evolution reaction catalysts. *Renew. Sustain. Energy Rev.*, 2021, *139*.
68. Antolini, E., Carbon supports for low-temperature fuel cell catalysts. *Appl. Catal. B*, 2009, *88* (1-2), 1-24.
69. Pizzutilo, E., et al., The Space Confinement Approach Using Hollow Graphitic Spheres to Unveil Activity and Stability of Pt-Co Nanocatalysts for PEMFC. *Adv. Energy Mater.*, 2017, *7* (20).
70. Sebastián, D., et al., Enhanced oxygen reduction activity and durability of Pt catalysts supported on carbon nanofibers. *Appl. Catal. B*, 2012, *115-116*, 269-275.
71. Ruiz-Cornejo, J. C., et al., Synthesis and applications of carbon nanofibers: a review. *Rev. Chem. Eng.*, 2020, *36* (4), 493-511.
72. Chen, J., et al., Carbon nanofiber-supported PdNi alloy nanoparticles as highly efficient bifunctional catalysts for hydrogen and oxygen evolution reactions. *Electrochim. Acta*, 2017, *246*, 17-26.
73. Sasaki, K., et al., Core-protected platinum monolayer shell high-stability electrocatalysts for fuel-cell cathodes. *Angew. Chem. Int. Ed. Engl.*, 2010, *49* (46), 8602-7.
74. Strasser, P., et al., Lattice-strain control of the activity in dealloyed core-shell fuel cell catalysts. *Nat Chem*, 2010, *2* (6), 454-60.
75. Jang, J. H., et al., Rational syntheses of core-shell Fe$_x$@Pt nanoparticles for the study of electrocatalytic oxygen reduction reaction. *Sci Rep*, 2013, *3*, 2872.
76. Grigoriev, S. A., et al., Platinum and palladium nano-particles supported by graphitic nano-fibers as catalysts for PEM water electrolysis. *Int. J. Hydrogen Energy*, 2011, *36* (6), 4143-4147.
77. García-Contreras, M. A., et al., Pt, PtNi and PtCoNi film electrocatalysts prepared by chemical vapor deposition for the oxygen reduction reaction in 0.5M KOH. *J. Alloys Compd.*, 2010, *504*, S425-S428.
78. Xu, S., et al., Chemical vapor deposition of graphene on thin-metal films. *Cell Rep.*, 2021.
79. Roller, J. M., et al., Catalyst nanoscale assembly from the vapor phase on corrosion resistant supports. *Electrochim. Acta*, 2013, *107*, 632-655.
80. Xu, C., et al., Physical vapor deposition process for engineering Pt based oxygen reduction reaction catalysts on NbO$_x$ templated carbon support. *J. Power Sources*, 2020, *451*.
81. Brault, P., et al., Polymer Electrolyte Fuel Cell Electrodes Grown by Vapor Deposition Techniques. *Chem. Vap. Deposition*, 2011, *17* (10-12), 296-304.
82. Ozdemir, O. K., A novel method to produce few layers of graphene as support materials for platinum catalyst. *Chemical Papers*, 2018, *73* (2), 387-395.
83. Yan, X., et al., Pt nanoparticles decorated high-defective graphene nanospheres as highly efficient catalysts for the hydrogen evolution reaction. *Carbon*, 2018, *137*, 405-410.

84. Xu, G.-R., et al., Platinum nanocuboids supported on reduced graphene oxide as efficient electrocatalyst for the hydrogen evolution reaction. *J. Power Sources*, 2015, *285*, 393-399.
85. Corrales-Sanchez, T., et al., MoS_2-based materials as alternative cathode catalyst for PEM electrolysis. *Int. J. Hydrogen Energy*, 2014, *39* (35), 20837-20843.
86. Chromium, molybdenum and tungsten. In *Chemistry of the elements*, N.N. Greenwood, A. E., Ed. 1997; pp 1002 - 1039.
87. Nickel, palladium and platinum. In *Chemistry of the elements*, N.N. Greenwood, A. E., Ed. 1997; pp 1144 - 1172.
88. Peng, X., et al., Atomic-scale intercalation of amorphous MoS_2 nanoparticles into N-doped carbon as a highly efficient electrocatalyst for hydrogen evolution reaction. *Int. J. Hydrogen Energy*, 2020, *45* (51), 27193-27201.
89. Ren, J.-T., et al., Molybdenum-based nanoparticles (Mo_2C, MoP and MoS_2) coupled heteroatoms-doped carbon nanosheets for efficient hydrogen evolution reaction. *Appl. Catal. B: Environmental*, 2020, *263*.
90. Wang, R., et al., Direct growth of high-content 1T phase MoS_2 film by pulsed laser deposition for hydrogen evolution reaction. *Appl. Surf. Sci.*, 2020, *504*.
91. Patel, M. D., et al., Directly deposited porous two-dimensional MoS_2 films as electrocatalysts for hydrogen evolution reactions. *Mater. Lett.*, 2018, *225*, 65-68.
92. Yousefzadeh, S.; Mardani, N., Facile synthesis of MoS_2 nanosheets-deposited TiO_2 nanotubes array electrode for enhanced electrocatalytic hydrogen evolution reaction. *Inorg. Chem. Commun.*, 2021.
93. Dong, W., et al., Defective-MoS_2/rGO heterostructures with conductive 1T phase MoS_2 for efficient hydrogen evolution reaction. *Int. J. Hydrogen Energy*, 2021, *46* (14), 9360-9370.
94. Peng, K., et al., Emerging hierarchical ternary 2D nanocomposites constructed from montmorillonite, graphene and MoS_2 for enhanced electrochemical hydrogen evolution. *Chem. Eng. J.*, 2020, *393*.
95. Khazraei, S., et al., Synergistic effect of ascorbic acid on the synthesis of mesoporous rGO-MoS_2(100) nanocomposites and promotion of hydrogen evolution reaction. *Int. J. Hydrogen Energy*, 2019, *44* (26), 13284-13295.
96. Yan, Y., et al., Recent Development of Molybdenum Sulfides as Advanced Electrocatalysts for Hydrogen Evolution Reaction. *ACS Catal.*, 2014, *4* (6), 1693-1705.
97. Stellmach, D., et al., Catalytic Behavior of Molybdenum Sulfide for the Hydrogen Evolution Reaction as a Function of Crystallinity and Particle Size Using Carbon Multiwall Nanotubes as Substrates. *Z. Phys. Chem.*, 2020, *234* (5), 1021-1043.
98. Sun, H., et al., Thermodynamics guided ultrafast and continuous preparation of Mo_2C nanocrystals for hydrogen evolution electrocatalysis. *Mater. Des.*, 2020, *193*.
99. Jinyan Cai, Y. S., Yipeng Zang, Shuwen Niu, Yufang Xie, Xusheng Zheng, N-induced lattice contraction generally boosts the hydrogen evolution catalysis of P-rich metal phosphides. *Sci. Adv.*, 2020, *6*.
100. Zhang, R. Q., et al., The role of titanium nitride supports for single-atom platinum-based catalysts in fuel cell technology. *Phys. Chem. Chem. Phys.*, 2012, *14* (48), 16552-7.
101. Rabi, O., et al., An inclusive review on the synthesis of molybdenum carbide and its hybrids as catalyst for electrochemical water splitting. *Mol. Catal.*, 2020, *494*.
102. Saha, S., et al., Titanium carbide: An emerging electrocatalyst for fuel cell and electrolyser. *Int. J. Hydrogen Energy*, 2021.
103. Zhang, X., et al., Progress in hydrogen production over transition metal carbide catalysts: challenges and opportunities. *Curr. Opin. Chem. Eng*, 2018, *20*, 68-77.
104. García, G., et al., Electrocatalysis on metal carbide materials. *Int. J. Hydrogen Energy*, 2016, *41* (43), 19664-19673.

105. Wang, Y., et al., Scalable processing hollow tungsten carbide spherical superstructure as an enhanced electrocatalyst for hydrogen evolution reaction over a wide pH range. *Electrochim. Acta*, 2019, *319*, 775-782.
106. Tang, C., et al., Tungsten carbide hollow microspheres as electrocatalyst and platinum support for hydrogen evolution reaction. *Int. J. Hydrogen Energy*, 2015, *40* (8), 3229-3237.
107. Jiang, Y., et al., Coupling PtNi Ultrathin Nanowires with MXenes for Boosting Electrocatalytic Hydrogen Evolution in Both Acidic and Alkaline Solutions. *Small*, 2019, *15* (12), e1805474.
108. Saha, S., et al., Performance evaluation of platinum-molybdenum carbide nanocatalysts with ultralow platinum loading on anode and cathode catalyst layers of proton exchange membrane fuel cells. *J. Power Sources*, 2018, *378*, 742-749.
109. Li, Y., et al., Current progress of molybdenum carbide-based materials for electrocatalysis: potential electrocatalysts with diverse applications. *Mater. Today Chem.*, 2021, *19*.
110. Regmi, Y. N., et al., Carbides of group IVA, VA and VIA transition metals as alternative HER and ORR catalysts and support materials. *J. Mater. Chem. A*, 2015, *3* (18), 10085-10091.
111. Saha, S., et al., Titanium carbide: An emerging electrocatalyst for fuel cell and electrolyser. *Int. J. Hydrogen Energy*, 2021, *46* (24), 12801-12821.
112. Chen, W. F., et al., Recent developments in transition metal carbides and nitrides as hydrogen evolution electrocatalysts. *Chem Commun (Camb)*, 2013, *49* (79), 8896-909.
113. Kim, H., et al., Highly efficient and durable TiN nanofiber electrocatalyst supports. *Nanoscale*, 2015, *7* (44), 18429-34.
114. Bhowmik, T., et al., Palladium Nanoparticle–Graphitic Carbon Nitride Porous Synergistic Catalyst for Hydrogen Evolution/Oxidation Reactions over a Broad Range of pH and Correlation of Its Catalytic Activity with Measured Hydrogen Binding Energy. *ACS Catal.*, 2016, *6* (3), 1929-1941.
115. Sheng, G., et al., Flowerlike $NiCo_2S_4$ Hollow Sub-Microspheres with Mesoporous Nanoshells Support Pd Nanoparticles for Enhanced Hydrogen Evolution Reaction Electrocatalysis in Both Acidic and Alkaline Conditions. *ACS Appl Mater Interfaces*, 2018, *10* (26), 22248-22256.
116. Chen, W. F., et al., Hydrogen-evolution catalysts based on non-noble metal nickel-molybdenum nitride nanosheets. *Angew. Chem. Int. Ed. Engl.*, 2012, *51* (25), 6131-5.
117. Li, Y., et al., A review: Target-oriented transition metal phosphide design and synthesis for water splitting. *Int. J. Hydrogen Energy*, 2021, *46* (7), 5131-5149.
118. Luo, S., et al., Facile synthesis of cobalt phosphide nanoparticles as highly active electrocatalysts for hydrogen evolution reaction. *Colloids Surf, A Physicochem Eng Asp*, 2020, *600*.
119. Pang, Y., et al., Self-supported amorphous nanoporous nickel-cobalt phosphide catalyst for hydrogen evolution reaction. *Prog. Nat. Sci. Mat*, 2021.
120. Chouki, T., et al., Solvothermal synthesis of iron phosphides and their application for efficient electrocatalytic hydrogen evolution. *Int. J. Hydrogen Energy*, 2020, *45* (41), 21473-21482.
121. Lu, Z.-p.; Sepunaru, L., Electrodeposition of iron phosphide film for hydrogen evolution reaction. *Electrochim. Acta*, 2020, *363*.
122. Wang, Y., et al., Synergistically engineering ultralow Pt doped FeNi alloy/FeNi phosphide nanoparticles for advanced hydrogen evolution reaction. *Colloids Surf, A Physicochem Eng Asp*, 2020, *604*.
123. Bockris, J. O. M., Kinetics of Activation Controlled Consecutive Electrochemical Reactions: Anodic Evolution of Oxygen. *J. Chem. Phys.*, 1956, *24* (4), 817-827.

124. Charles, V., et al., Progress and challenges pertaining to the earthly-abundant electrocatalytic materials for oxygen evolution reaction. *Sustainable Materials and Technologies*, 2021, *28*.
125. Paul, S. C., et al., Nanomaterials as electrocatalyst for hydrogen and oxygen evolution reaction: Exploitation of challenges and current progressions. *Polyhedron*, 2021, *193*.
126. Chen, Z., et al., Electrocatalysts for acidic oxygen evolution reaction: Achievements and perspectives. *Nano Energy*, 2020, *78*.
127. Suen, N. T., et al., Electrocatalysis for the oxygen evolution reaction: recent development and future perspectives. *Chem. Soc. Rev.*, 2017, *46* (2), 337-365.
128. Rossmeisl, J., et al., Electrolysis of water on (oxidized) metal surfaces. *Chem. Phys.*, 2005, *319* (1-3), 178-184.
129. Shan, J., et al., Regulating Electrocatalysts via Surface and Interface Engineering for Acidic Water Electrooxidation. *ACS Energy Lett.*, 2019, *4* (11), 2719-2730.
130. Trasatti, S., Electrocatalysis in the anodic evolution of oxygen and chlorine. *Electrochim. Acta*, 1984, *29* (11), 1503-1512,.
131. Man, I. C., et al., Universality in Oxygen Evolution Electrocatalysis on Oxide Surfaces. *ChemCatChem*, 2011, *3* (7), 1159-1165.
132. Man, I. C. Theoretical study of Electro-caratlysts for oxygen evolution. Technical University of Denmark, Kgs. Lyngby, Denmark, 2011.
133. Cheng, J., et al., Study of $Ir_xRu_{1-x}O_2$ oxides as anodic electrocatalysts for solid polymer electrolyte water electrolysis. *Electrochim. Acta*, 2009, *54* (26), 6250-6256.
134. Cherevko, S., et al., Dissolution of Noble Metals during Oxygen Evolution in Acidic Media. *ChemCatChem*, 2014, *6* (8), 2219-2223.
135. Bai, J., et al., Ultrathin Rhodium Oxide Nanosheet Nanoassemblies: Synthesis, Morphological Stability, and Electrocatalytic Application. *ACS Appl. Mater. Interfaces*, 2017, *9* (20), 17195–17200.
136. A. Damjanovic, A. D., J. OM Bockris, Electrode kinetics of oxygen evolution and dissolution on Rh, Ir, and Pt-Rh alloy electrodes *J. Electrochem. Soc.*, 1966, *113* (7).
137. Owe, L.-E., et al., Iridium–ruthenium single phase mixed oxides for oxygen evolution: Composition dependence of electrocatalytic activity. *Electrochim. Acta*, 2012, *70*, 158-164.
138. C. Angelinetta, S. T., Lj.D. Atanososka, R.T. Atanasoski, Surface properties of RuO_2-IrO_2 mixed oxide electrodes. *J. Electroanal. Chem. Interf. Electrochem.*, 1986, *214* (1–2), 535-546.
139. Luo, F., et al., Robust and Stable Acidic Overall Water Splitting on Ir Single Atoms. *Nano Lett.*, 2020, *20* (3), 2120-2128.
140. Wang, Q., et al., Ultrahigh-Loading of Ir Single Atoms on NiO Matrix to Dramatically Enhance Oxygen Evolution Reaction. *J. Am. Chem. Soc.*, 2020, *142* (16), 7425-7433.
141. Sánchez-Page, B., et al., Influence of graphene sheet properties as supports of iridium-based N-heterocyclic carbene hybrid materials for water oxidation electrocatalysis. *J. Organomet. Chem.*, 2020, *919*.
142. Yu, X., et al., Surface oxidized iron-nickel nanorods anchoring on graphene architectures for oxygen evolution reaction. *Chin. Chem. Lett.*, 2021.
143. Wen, X., et al., Ultrafine iridium oxide supported on carbon nanotubes for efficient catalysis of oxygen evolution and oxygen reduction reactions. *Mater. Today Energy*, 2018, *10*, 153-160.
144. Badam, R., et al., Synthesis and electrochemical analysis of novel IrO_2 nanoparticle catalysts supported on carbon nanotube for oxygen evolution reaction. *Int. J. Hydrogen Energy*, 2018, *43* (39), 18095-18104.
145. Xue, Q., et al., Carbon nanobowls supported ultrafine iridium nanocrystals: An active and stable electrocatalyst for the oxygen evolution reaction in acidic media. *J. Colloid Interface Sci.*, 2018, *529*, 325-331.

146. Sugita, Y., et al., Connected iridium nanoparticle catalysts coated onto silica with high density for oxygen evolution in polymer electrolyte water electrolysis. *Nanoscale Advances*, 2020, *2* (1), 171-175.
147. Xu, J., et al., Antimony doped tin oxides and their composites with tin pyrophosphates as catalyst supports for oxygen evolution reaction in proton exchange membrane water electrolysis. *Int. J. Hydrogen Energy*, 2012, *37* (24), 18629-18640.
148. Karimi, F.; Peppley, B. A., Metal Carbide and Oxide Supports for Iridium-Based Oxygen Evolution Reaction Electrocatalysts for Polymer-Electrolyte-Membrane Water Electrolysis. *Electrochim. Acta*, 2017, *246*, 654-670.
149. Badruzzaman, A., et al., Recent advances in cobalt based heterogeneous catalysts for oxygen evolution reaction. *Inorg. Chim. Acta*, 2020, *511*.
150. Liu, T., et al., Insight into a class of cobalt nitrides for oxygen evolution catalysis: Nitrogen-rich matters. *Electrochim. Acta*, 2019, *323*.
151. Huang, T., et al., A heterostructure of layered double hydroxide wrapped in few-layer carbon with iridium doping for efficient oxygen evolution. *Electrochim. Acta*, 2019, *296*, 590-597.
152. Zhang, J., et al., Hierarchical iridium-based multimetallic alloy with double-core-shell architecture for efficient overall water splitting. *Sci. China Mater.*, 2019, *63* (2), 249-257.
153. Chatterjee, S., et al., Nanoporous multimetallic Ir alloys as efficient and stable electrocatalysts for acidic oxygen evolution reactions. *J. Catal.*, 2021, *393*, 303-312.
154. Zhang, T., et al., Ir-Pd nanoalloys with enhanced surface-microstructure-sensitive catalytic activity for oxygen evolution reaction in acidic and alkaline media. *Sci. China Mater.*, 2018, *61* (7), 926-938.
155. Lee, S. W., et al., Multifunctional Ir–Ru alloy catalysts for reversal-tolerant anodes of polymer electrolyte membrane fuel cells. *J. Mater Sci Technol*, 2021, *60*, 105-112.
156. Guo, H., et al., Rational Design of Rhodium-Iridium Alloy Nanoparticles as Highly Active Catalysts for Acidic Oxygen Evolution. *ACS Nano*, 2019, *13* (11), 13225-13234.
157. Zhu, M., et al., Superior overall water splitting electrocatalysis in acidic conditions enabled by bimetallic Ir-Ag nanotubes. *Nano Energy*, 2019, *56*, 330-337.
158. Aizaz Ud Din, M., et al., Synthesis of 3D IrRuMn Sphere as a Superior Oxygen Evolution Electrocatalyst in Acidic Environment. *Chemistry*, 2020, *26* (25), 5662-5666.
159. Xu, J., et al., Strong Electronic Coupling between Ultrafine Iridium–Ruthenium Nanoclusters and Conductive, Acid-Stable Tellurium Nanoparticle Support for Efficient and Durable Oxygen Evolution in Acidic and Neutral Media. *ACS Catal.*, 2020, *10* (6), 3571-3579.
160. Shan, J., et al., Transition-Metal-Doped RuIr Bifunctional Nanocrystals for Overall Water Splitting in Acidic Environments. *Adv. Mater.*, 2019, *31* (17), e1900510.
161. Liu, N., et al., Hierarchically porous nickel–iridium–ruthenium–aluminum alloys with tunable compositions and electrocatalytic activities towards the oxygen/hydrogen evolution reaction in acid electrolyte. *J. Mater. Chem. A*, 2020, *8* (13), 6245-6255.
162. Chen, Z., et al., Iridium-based nanomaterials for electrochemical water splitting. *Nano Energy*, 2020, *78*.
163. Kwon, T., et al., Dopant-Assisted Control of the Crystallite Domain Size in Hollow Ternary Iridium Alloy Octahedral Nanocages toward the Oxygen Evolution Reaction. *Cell Rep.*, 2020, *1* (12).
164. Wang, Y., et al., Nanoporous Iridium-Based Alloy Nanowires as Highly Efficient Electrocatalysts Toward Acidic Oxygen Evolution Reaction. *ACS Appl Mater Interfaces*, 2019, *11* (43), 39728-39736.
165. Pi, Y., et al., Highly Efficient Acidic Oxygen Evolution Electrocatalysis Enabled by Porous Ir–Cu Nanocrystals with Three-Dimensional Electrocatalytic Surfaces. *Chem. Mater.*, 2018, *30* (23), 8571-8578.

166. Jin, H., et al., Lanthanide metal-assisted synthesis of rhombic dodecahedral MNi (M = Ir and Pt) nanoframes toward efficient oxygen evolution catalysis. *Nano Energy*, 2017, *42*, 17-25.
167. Gou, W., et al., Iridium-Chromium Oxide Nanowires as Highly Performed OER Catalysts in Acidic Media. *ChemCatChem*, 2019, *11* (24), 6008-6014.
168. Zhou, Z., et al., Cultivating crystal lattice distortion in IrO_2 via coupling with MnO_2 to boost the oxygen evolution reaction with high intrinsic activity. *Chem. Commun.*, 2018, *54* (39), 4959-4962.
169. Grupioni, A. A. F., et al., Voltammetric characterization of an iridium oxide-based system: the pseudocapacitive nature of the Ir0.3Mn0.7O2 electrode. *Electrochim. Acta*, 2002, *48* (4), 407-418.
170. Ghadge, S. D., et al., Experimental and Theoretical Validation of High Efficiency and Robust Electrocatalytic Response of One-Dimensional (1D) $(Mn,Ir)O_2$:10F Nanorods for the Oxygen Evolution Reaction in PEM-Based Water Electrolysis. *ACS Catal.*, 2019, *9* (3), 2134-2157.
171. Lee, J., et al., Boosting Stability and Activity of Oxygen Evolution Catalyst in Acidic Medium: Bimetallic Ir−Fe Oxides on Reduced Graphene Oxide Prepared through Ultrasonic Spray Pyrolysis. *ChemCatChem*, 2019, *11* (11), 2615-2623.
172. Audichon, T., et al., IrO_2 Coated on RuO_2 as Efficient and Stable Electroactive Nanocatalysts for Electrochemical Water Splitting. *J. Phys. Chem. C*, 2016, *120* (5), 2562-2573.
173. Hu, W., et al., Ir-Surface Enriched Porous Ir-Co Oxide Hierarchical Architecture for High Performance Water Oxidation in Acidic Media. *ACS Appl. Mater. Interfaces*, 2014, *6* (15), 12729-12736.
174. Yang, L., et al., Efficient oxygen evolution electrocatalysis in acid by a perovskite with face-sharing IrO_6 octahedral dimers. *Nat Commun*, 2018, *9* (1), 5236.
175. Faustini, M., et al., Hierarchically Structured Ultraporous Iridium-Based Materials: A Novel Catalyst Architecture for Proton Exchange Membrane Water Electrolyzers. *Adv. Energy Mater.*, 2019, *9* (4), 1802136.
176. Diaz-Morales, O., et al., Iridium-based double perovskites for efficient water oxidation in acid media. *Nat Commun*, 2016, *7*, 12363.
177. Zhang, R., et al., A Dissolution/Precipitation Equilibrium on the Surface of Iridium-Based Perovskites Controls Their Activity as Oxygen Evolution Reaction Catalysts in Acidic Media. *Angew. Chem.* , 2019, *131* (14), 4619-4623.
178. Anantharaj, S.; Noda, S., Amorphous Catalysts and Electrochemical Water Splitting: An Untold Story of Harmony. *Small*, 2020, *16* (2), e1905779.
179. Zhang, R., et al., A Dissolution/Precipitation Equilibrium on the Surface of Iridium-Based Perovskites Controls Their Activity as Oxygen Evolution Reaction Catalysts in Acidic Media. *Angew. Chem. Int. Ed. Engl.*, 2019, *58* (14), 4571-4575.
180. Sahu, A. K., et al., Properties and Applications of Ruthenium. In *Noble and Precious Metals - Properties, Nanoscale Effects and Applications*, 2018.
181. Larissa, B., Copper(I) complexes as emitting materials. In *New Emitters for OLEDs: The coordination- and photo-chemistry of mononuclear neutral copper(I) complexes*, Logos Verlag Berlin GmbH: Berlin, 2016.
182. Cherevko, S., et al., Oxygen and hydrogen evolution reactions on Ru, RuO_2, Ir, and IrO_2 thin film electrodes in acidic and alkaline electrolytes: A comparative study on activity and stability. *Catal. Today*, 2016, *262*, 170-180.
183. Cao, L., et al., Dynamic oxygen adsorption on single-atomic Ruthenium catalyst with high performance for acidic oxygen evolution reaction. *Nat Commun*, 2019, *10* (1), 4849.
184. Yao, Y., et al., Engineering the electronic structure of single atom Ru sites via compressive strain boosts acidic water oxidation electrocatalysis. *Nat. Catal.*, 2019, *2* (4), 304-313.

185. Soszko, M., et al., Electrochemical dissolution of Pt-Pd-Ru alloys. *J. Electroanal. Chem.*, 2020, *877*.
186. Forgie, R., et al., Bimetallic Ru Electrocatalysts for the OER and Electrolytic Water Splitting in Acidic Media *Electrochem. Solid-State Lett.*, 2010, *13* (4), B36.
187. Lin, Y., et al., Chromium-ruthenium oxide solid solution electrocatalyst for highly efficient oxygen evolution reaction in acidic media. *Nat Commun*, 2019, *10* (1), 162.
188. Retuerto, M., et al., Na-doped ruthenium perovskite electrocatalysts with improved oxygen evolution activity and durability in acidic media. *Nat Commun*, 2019, *10* (1), 2041.
189. Miao, X., et al., Quadruple perovskite ruthenate as a highly efficient catalyst for acidic water oxidation. *Nat. Commun.*, 2019, *10* (1).
190. Kukshon, J., et al., Synthesis of mesoporous iron oxide nanoparticles from mesoporous silica template via nano-replication. *Functional Materials Letters*, 2012, *01*.
191. Felix, C., et al., Synthesis and Optimisation of IrO2 Electrocatalysts by Adams Fusion Method for Solid Polymer Electrolyte Electrolysers. *Micro and Nanosystemse*, 2012, *4* (3), 186-191.
192. Lee, S. W., et al., Ordered mesoporous ruthenium oxide with balanced catalytic activity and stability toward oxygen evolution reaction. *Catal. Today*, 2020, *358*, 203-209.
193. Roy, C., et al., Trends in Activity and Dissolution on RuO_2 under Oxygen Evolution Conditions: Particles versus Well-Defined Extended Surfaces. *ACS Energy Lett.*, 2018, *3* (9), 2045-2051.
194. Goryachev, A., et al., Electrochemical stability of RuO_2(110)/Ru(0001) model electrodes in the oxygen and chlorine evolution reactions. *Electrochim. Acta*, 2020, *336*.
195. Biswas, A., et al., Enhanced electrocatalytic oxygen evolution activity in geometrically designed $SrRuO_3$ thin films. *Appl. Surf. Sci.*, 2020, *529*.
196. Su, J., et al., Assembling Ultrasmall Copper-Doped Ruthenium Oxide Nanocrystals into Hollow Porous Polyhedra: Highly Robust Electrocatalysts for Oxygen Evolution in Acidic Media. *Adv. Mater.*, 2018, e1801351.
197. Chen, S., et al., Mn-Doped RuO_2 Nanocrystals as Highly Active Electrocatalysts for Enhanced Oxygen Evolution in Acidic Media. *ACS Catal.*, 2019, *10* (2), 1152-1160.
198. Tian, Y., et al., A Co-Doped Nanorod-like RuO_2 Electrocatalyst with Abundant Oxygen Vacancies for Acidic Water Oxidation. *iScience*, 2020, *23* (1), 100756.
199. Zheng, T., et al., Intercalated Iridium Diselenide Electrocatalysts for Efficient pH-Universal Water Splitting. *Angew. Chem. Int. Ed. Engl.*, 2019, *58* (41), 14764-14769.
200. Wang, J., et al., Amorphization activated ruthenium-tellurium nanorods for efficient water splitting. *Nat Commun*, 2019, *10* (1), 5692.
201. Chen, J., et al., A bifunctional electrocatalyst of PtNi nanoparticles immobilized on three-dimensional carbon nanofiber mats for efficient and stable water splitting in both acid and basic media. *J. Mater. Sci.*, 2017, *52* (22), 13064-13077.
202. Cao, D., et al., Construction of Defect-Rich RhCu Nanotubes with Highly Active Rh_3Cu_1 Alloy Phase for Overall Water Splitting in All pH Values. *Adv. Energy Mater.*, 2020, *10* (9).
203. Wu, Z. P., et al., Non-Noble-Metal-Based Electrocatalysts toward the Oxygen Evolution Reaction. *Adv. Funct. Mater.*, 2020, *30* (15).
204. Pan, Q.; Wang, L., Recent perspectives on the structure and oxygen evolution activity for non-noble metal-based catalysts. *J. Power Sources*, 2021, *485*.
205. Li, A., et al., Stable Potential Windows for Long-Term Electrocatalysis by Manganese Oxides Under Acidic Conditions. *Angew. Chem. Int. Ed. Engl.*, 2019, *58* (15), 5054-5058.
206. Zhao, L., et al., Iron oxide embedded titania nanowires – An active and stable electrocatalyst for oxygen evolution in acidic media. *Nano Energy*, 2018, *45*, 118-126.
207. Huynh, M., et al., Nature of Activated Manganese Oxide for Oxygen Evolution. *J. Am. Chem. Soc.*, 2015, *137* (47), 14887-904.

208. Hayashi, T., et al., Electrochemical characterization of manganese oxides as a water oxidation catalyst in proton exchange membrane electrolysers. *R Soc Open Sci*, 2019, *6* (5), 190122.
209. Mondschein, J. S., et al., Crystalline Cobalt Oxide Films for Sustained Electrocatalytic Oxygen Evolution under Strongly Acidic Conditions. *Chem. Mater.*, 2017, *29* (3), 950-957.
210. Yang, X., et al., Highly acid-durable carbon coated Co_3O_4 nanoarrays as efficient oxygen evolution electrocatalysts. *Nano Energy*, 2016, *25*, 42-50.
211. Tong, Y., et al., A Bifunctional Hybrid Electrocatalyst for Oxygen Reduction and Evolution: Cobalt Oxide Nanoparticles Strongly Coupled to B,N-Decorated Graphene. *Angew. Chem. Int. Ed. Engl.*, 2017, *56* (25), 7121-7125.
212. Kwong, W. L., et al., Cobalt-doped hematite thin films for electrocatalytic water oxidation in highly acidic media. *Chem Commun (Camb)*, 2019, *55* (34), 5017-5020.
213. Evans, T. A.; Choi, K.-S., Electrochemical Synthesis and Investigation of Stoichiometric, Phase-Pure $CoSb_2O_6$ and $MnSb_2O_6$ Electrodes for the Oxygen Evolution Reaction in Acidic Media. *ACS Appl. Energy Mater.*, 2020, *3* (6), 5563-5571.
214. Huynh, M., et al., Design of template-stabilized active and earth-abundant oxygen evolution catalysts in acid. *Chem Sci*, 2017, *8* (7), 4779-4794.
215. Moreno-Hernandez, I. A., et al., Crystalline nickel manganese antimonate as a stable water-oxidation catalyst in aqueous 1.0 M H_2SO_4. *Energy Environ. Sci.*, 2017, *10* (10), 2103-2108.
216. Chauhan, M.; Deka, S., Hollow Cobalt Sulfide Nanoparticles: A Robust and Low-Cost pH-Universal Oxygen Evolution Electrocatalyst. *ACS Appl. Energy Mater.*, 2019, *3* (1), 977-986.
217. Xiong, Q., et al., One-step synthesis of cobalt-doped MoS_2 nanosheets as bifunctional electrocatalysts for overall water splitting under both acidic and alkaline conditions. *Chem Commun (Camb)*, 2018, *54* (31), 3859-3862.
218. Cheng, W., et al., A metal-vacancy-solid-solution NiAlP nanowall array bifunctional electrocatalyst for exceptional all-pH overall water splitting. *J. Mater. Chem. A*, 2018, *6* (20), 9420-9427.
219. Hu, F., et al., Amorphous Metallic NiFeP: A Conductive Bulk Material Achieving High Activity for Oxygen Evolution Reaction in Both Alkaline and Acidic Media. *Adv. Mater.*, 2017, *29* (32).

CHAPTER 2. STRUCTURAL STUDY OF $Ir_{1-x}Mo_xO_2$

The materials presented in this chapter follow the general formula $Ir_{1-x}Mo_xO_2$ where x = 0, 0.1, 0.3, 0.5, 0.7 and 1. The catalysts were developed using a cost-effective synthesis route by creating a mix in water of $IrCl_3$, $MoCl_5$ and PMMA beads (template polymethylmethacrylate), followed by a thermal treatment in order to remove organic material, and annealed at different temperatures to form Ir-Mo phases. XRD analysis revealed a single phase with rutile IrO_2-type structure for samples with less than 70%Mo and SEM images showed porous microspheres with a variety of shapes.

The catalysts were synthesized by Mateusz Odziomek at LCMP (group of Cédric Boissiere, Sorbonne Université). X-Ray and Scanning Electron Microscopy (SEM) characterization techniques were performed at ITODYS (group of Jennifer Peron and Marion Giraud, Université de Paris) by Marine Elmaalouf. All the results presented in this chapter were analyzed, summarized and reviewed with the relevant colleagues in order to introduced the electrochemical experiments presented in chapters 3 and 4.

2.1 Introduction

In recent years, the interest of developing new catalysts for the OER have become a crucial point in fundamental and applied research with the aim of increasing the PEMWE commercialization. To date, IrO_2 is the only catalyst that combines both activity and stability for the OER, however, iridium being one of the rarest elements on earth with 0.000037 ppm in the earth crust,[1] the cost of such materials is high. Therefore, it is necessary to reduce or replace the amount of NM, in this case iridium, on the anode side of the electrolyzer. One of the approaches is by using Non-NMs in order to produce active mixed oxides with interesting morphologies, structures, stoichiometries, and other characteristics (i.e., conductivity, stability and activity).[2-4] These materials usually present higher electrochemical activity compared to state-of-art IrO_2, despite the lack of long-term stability due to iridium leaching, which can also probably enhances the O_2 evolution by the modification of the structure or the morphology. Understanding morphology changes makes it possible to develop new synthesis techniques that can allow to achieve novel materials with new morphologies while retaining main characteristics that are crucial for the reaction (nature of the material and stoichiometry).

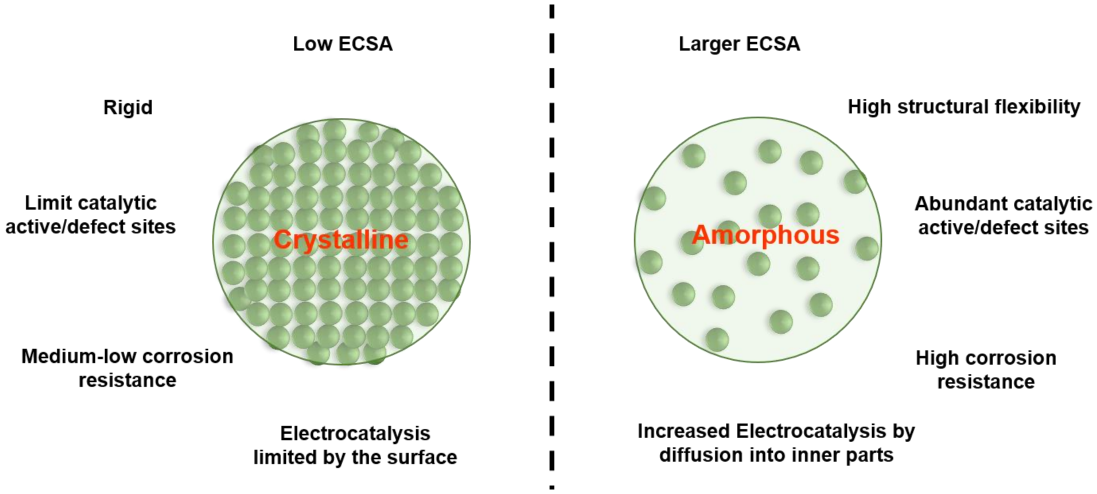

Figure 2.1 Illustration comparing main characteristics between crystalline and amorphous catalysts.

The different routes of synthesis to produce iridium oxide nanoparticles (crystalline or amorphous) are hydrothermal method,[5] sol-gel, thermal decomposition,[6] Adams fusion method[7] or polyol route,[8, 9] all of which are allowing the control of the morphology. From this, Ir-based materials, especially amorphous oxides (Figure 2.1), have been reported to be more active than their crystalline form,[10] and other non-NMs catalysts that contains amorphous phases are reported repeatedly to be better performing OER electrocatalysis in acid media.[11] IrO_2-Ta_2O_5 was one of the first amorphous Ir-based oxide where an accelerated oxygen evolution was achieved and a significant increase in active surface area was reached by only changing the thermal decomposition temperature.[6, 12] However, amorphous IrO_x are usually obtained without mixing with another metal, therefore these oxides are usually in the form of thin films[13-15] presenting only an overpotential of 220 mV at 10 mA cm^{-2}.[15] Also, *Kim et al.,*[4] have successfully reported an iridium oxide shell on a metallic iridium core that exhibited a great balance between activity and stability. Hierarchical structures such as the one presented by *Faustini et al.,*[10] reported a versatile process to produce highly porous Ir-based and mixed oxides with an increase of surface area with high accessibility to active sites.

Moreover, other amorphous electrocatalysts based on Non-NMs such as Co, Ni, Fe and Mo have been proposed. However, these materials have been mostly developed for alkaline systems, but they still show the importance of amorphization in oxides.[16] Among them, molybdenum in the form of sulfides, carbides and phosphides have been extensively studied[17-19] mostly for HER but not extensively in the form of oxides.[20] So far *Cheng et al.,*[7] and *Tariq et al.,*[21] have reported mixed Mo oxides for OER in acidic conditions, $Ir_{0.4}Ru_{0.6}Mo_xO_y$ and the hybrid composite IrO_2-MoO_3. The latter presented a high activity-stability compared to state-of-art IrO_2 by almost doubling the performances (25.2 mA cm^{-2} vs 11.7 mA cm^{-2}) as well as an overpotential of 110 mV at 10 mA cm^{-2}. Additionally, molybdenum is an abundant element in the earth's crust, with a variation of oxidation states that makes it interesting and suitable to undergo OER. Also, the strong binding interaction of Non-NMs oxides with NMs-NPs is a promising way of reducing the use of NMs, therefore, this combination is suitable to reduce costs since a balance in activity can be achivable.[22, 23]

Based on the above and to the best of our knowledge no pseudo-amorphous or poor crystalline Ir-Mo oxides have been synthesized by a cost-effective synthesis route. Therefore, in this chapter we report the synthesis and characterization of $Ir_{1-x}Mo_xO_2$ compounds (x = 0, 0.1, 0.3, 0.5, 0.7 and 1) by the spray-drying technique,[10, 24] and the formation of a pure mixed oxide phase evidenced by XRD as well as SEM as complementary characterization techniques.

2.2. Synthesis and characterization

The main goal of this section is to study the maximum solubility of Mo in the IrO_2 matrix. The structural characterization of the synthesized materials by the spray-drying method were performed by SEM and X-ray diffraction in order to confirm the formation of single phases at the corresponding calcination temperatures.

2.2.1. Experimental section

2.2.1.1. Material synthesis

Different routes of synthesis can be applied to synthesized metallic iridium or amorphous iridium oxide materials.[7, 9, 25] The disadvantage of these methods is that they lead to irregular morphologies, they use of high temperatures synthesis and they are not scalable for industrial preparation. On the other hand, the spray-drying method which is a low cost, water-based and scalable process is widely use in the production of powder milk in the food industry and in pharmaceutical industry,[26] and has been proved as well that allows the production of porous catalysts.[27, 28]

In this work, the spray-drying process was used to tune the crystallinity and porosity of the materials in order to enhance the catalytic surface area and the diffusion of reactants and products. $Ir_{1-x}Mo_xO_2$, were prepared at different values of x (x =0, 0.1, 0.3, 0.5, 0.7 and 1), using $IrCl_3.xH_2O$ (98%, Alfa-Aesar) and $MoCl_5.xH_2O$ (98%, Sigma-Aldrich) as inorganic precursors. These were hydrolyzed in water, and PMMA beads were latter introduced while maintaining a constant stirring. The process is illustrated graphically in Figure 2.2.

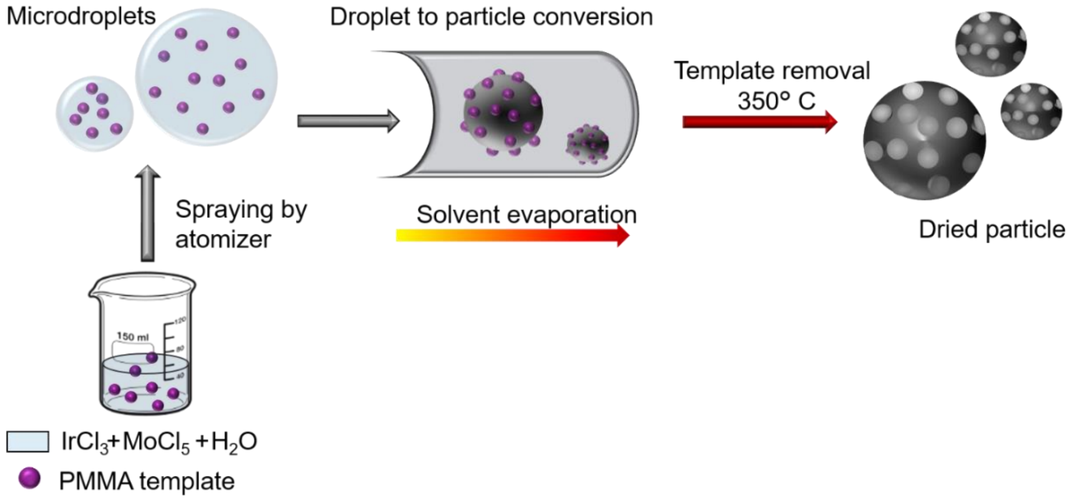

Figure 2.2 Graphical representation of spray-drying process of Ir-Mo oxides.

After stirring, the precursors solution is first sprayed to form microdroplets which are then transported by an air flux in a drying chamber where evaporation of water takes place. During the evaporation, is where the importance of the PMMA beads is noticeable since they provide the pore formation thanks to the quenching effect that takes place. This effect is the one that allows metal species to surround the beads. After evaporation, the powder is then collected in a glass vessel by a vortex separator. The collected powder is then calcined in the range 400 - 800°C increasing every 50°C. Full description of the components of the spray-drying technique is presented in chapter 6.

2.2.1.2. Structural characterization

a) SEM

The morphology of the compounds was observed using scanning electron microscopy (Zeiss SUPRA 40 FESEM). The images were recorded based on backscattered electrons with an accelerating voltage of 5 Kv and are presented in section 2.2.2.

b) XRD

As prepared $Ir_{1-x}Mo_xO_2$ where characterized by means of X-ray, and their diffractograms are shown in section 2.2.2. ITODYS group is using a Panalytical X'pert pro diffractometer working in Brag Brentano geometry with Co Kα radiation and a multichannel X'celerator detector. The diffractometer was operated over the angular range $2\theta = 15 - 120$ ° for Rietveld analysis. The qualitative identification of phases was performed by comparing the XRD profile reflections with diffraction profiles reported in the Inorganic Crystal Structure Database (ICSD). Based on that, structural information was extracted by Rietveld refinement using MAUD program [29] allowing the determination of *a,c* parameters, and crystallites sizes for each diffraction peak.

2.2.2. Results and discussion

2.2.2.1. Morphology and structural properties

The mixed oxides are labelled as *x*-Mo, where *x* corresponds to the mole percentage content of molybdenum in the sample. The synthesis of $Ir_{1-x}Mo_xO_2$ was carried out at different compositions of x (0, 0.1, 0.3, 0.5, 0.7 and 1) and calcined at the following temperatures 400, 450, 500, 550, 600 and 800 °C in order to determine the doping limit of molybdenum in the IrO_2 matrix, as well as to observe at what temperature single phases of each composition are obtained.

However, 70-Mo compositions calcined in the range 400 – 600° C were not obtained as single phases as shown in Figure 2.3.

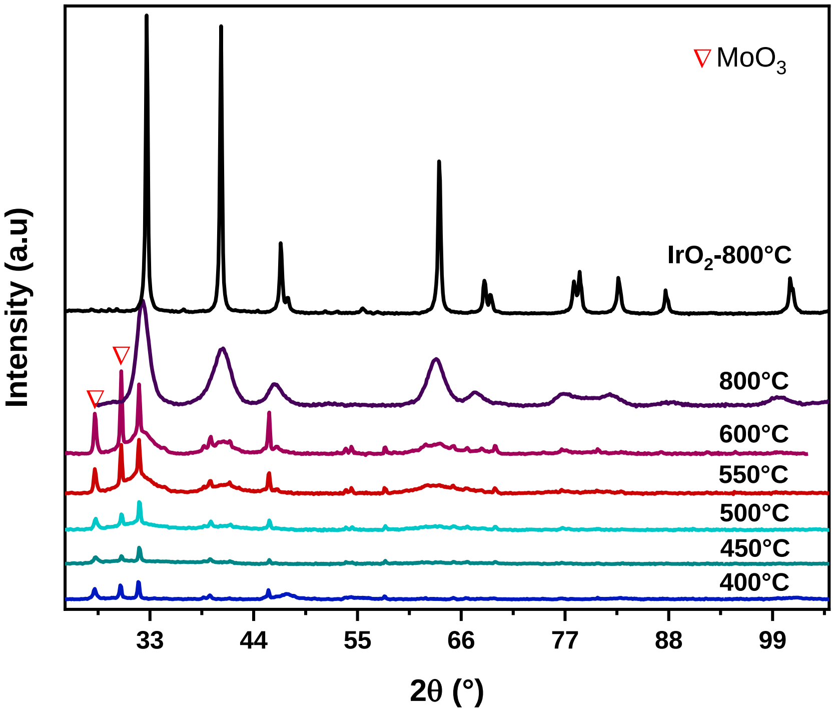

Figure 2.3 XRD patterns of $Ir_{0.3}Mo_{0.7}O_2$ after calcination at different temperatures in air.

The XRD analysis in 70-Mo showed the mixture of oxides, MoO_3 and $Ir_{1-x}Mo_xO_2$. The additional peaks in the range of 2θ = 23 – 28°, which correspond to the indexed planes (100), (002), and (011), are congruent with the secondary phase, MoO_3 (ICSD 98-015-2314, orthorhombic unit cell with *Pnma* space group), and overlap the desired formation of the Ir-70%Mo oxide. Similar behaviour was presented in the hybrid composite IrO_2-MoO_3 with 70% Mo calcined at 450 °C prepared by hydrothermal method.[21] However, it was only possible to obtain a single phase of $Ir_{0.3}Mo_{0.7}O_2$ with no impurities at 800 °C in our case.

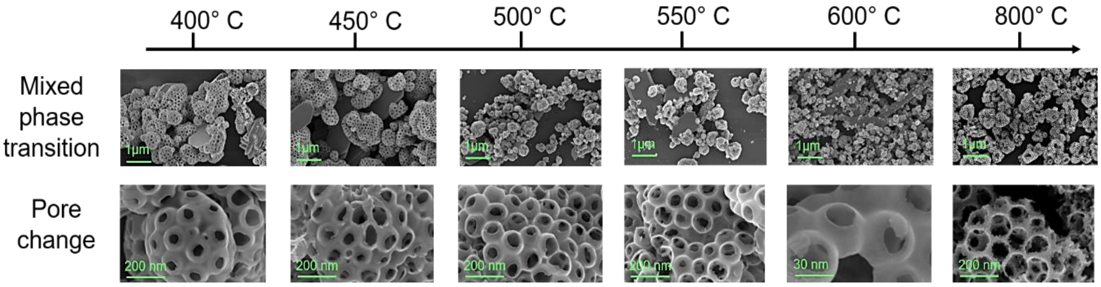

Figure 2.4 SEM micrographs of 70-Mo after calcination at different temperatures in air.

SEM images of the as-synthesized 70-Mo oxides are shown in Figure 2.4. In these micrographs, the plate-like particles were assigned to MoO_3, as previously reported by *Tariq et al.,*[21] and recently by *Zhang et al.,*[20] at sintered temperature of 550 °C. The different porous microspheres with various shapes like spheroidal or donut-like morphology were assigned to $Ir_{0.5}Mo_{0.5}O_2$ particles since they are also present in single phases of 10, 30 and 50-Mo compounds. Also, the formation of MoO_3 is reported to occur above 300 °C,[30] explaining the presence of this in sample 70-Mo, and the absence of the plate-like morphology at 800° C can be attributed to the fact that sublimation of MoO_3 in air starts at temperatures between 500 and 700 °C,[30, 31] therefore at 800 °C single phase $Ir_{0.3}Mo_{0.7}O_2$ is formed. On the other hand, the surface morphology and XRD patterns of 10, 30 and 50-Mo sintered at different temperatures are shown in Figure 2.5. Overall, the materials showed high porosity and present different shapes like spheroidal, donut-like and buckled morphology as in 70-Mo, which is a main characteristic of porous materials prepared by spray drying.[10, 24, 32] Also, the cavities around 200-300 nm constitute the spheres walls with large pores in the center, and those vary as the temperature increases.

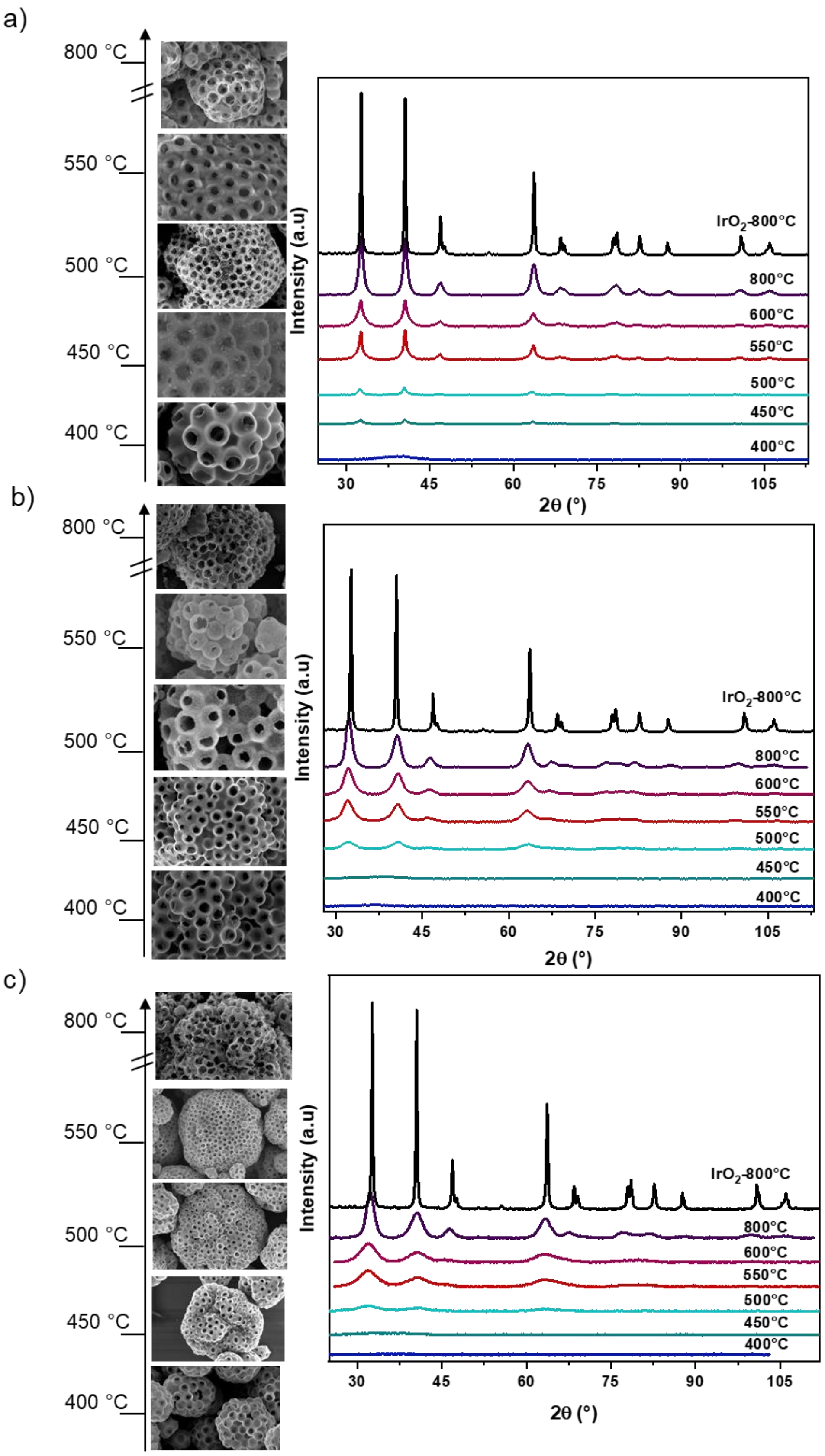

Figure 2.5 SEM and XRD patterns of a) 10-Mo, b) 30-Mo and c) 50-Mo samples calcined at different temperatures in air.

XRD patterns exhibited the formation of single phase as shown in Figure 2.5, and the corresponding SEM micrograph at each temperature are presented. All XRD patterns were indexed in a rutile IrO_2-type structure (ICSD 98-008-4577) with a tetragonal unit cell with *P42/mnm* space group when possible since amorphous structures were present at low temperatures (400 and 450°C) where XRD patterns do not present any distinguishable peaks. This behaviour is independent from the synthesis route, since *Liu et al.,*[33] reported the transition from amorphous to rutile phase of IrO_2 obtained by Adams fusion around the same temperatures. At a first look, the introduction of molybdenum into the mixed oxide delays the crystallization temperature. In the 10-Mo series, the samples heated at 450 and 500 °C presented the formation of needle-like particles. This particle formation was not associated to the formation of any secondary phase, on the contrary, it was determined the coexistence of amorphous and crystal particles in 10-Mo series since is at 450 °C reported by *Faustini et al.,*[10] that pure IrO_2 forms and exhibits the formation of needle-like particles. Also, these were no longer present in the range 550 - 800°C.

The series of 30 and 50-Mo are presenting a higher porosity which is reflected by broader and distorted peaks above 70° in the XRD patterns. For 30 and 50-Mo series, the crystallization of iridium-molybdenum oxide starts at 500 and 550 °C, respectively, since characteristic peaks only appeared at these temperatures. No crystal particles were detected on these samples as observed in the SEM micrographs in Figure 2.5b and c. Moreover, SEM micrographs at low calcination temperatures are presenting a homogeneous surface (i.e., soft, flat) and as temperature increases it is possible to observe roughness (i.e., crystallites). In the case of samples calcinated at 800 °C, in all compositions, the walls of those porous microspheres are slightly damaged with respect to other temperatures, probably due to the growth of needle-like morphology in the walls since IrO_2 tends to crystallize in this form.

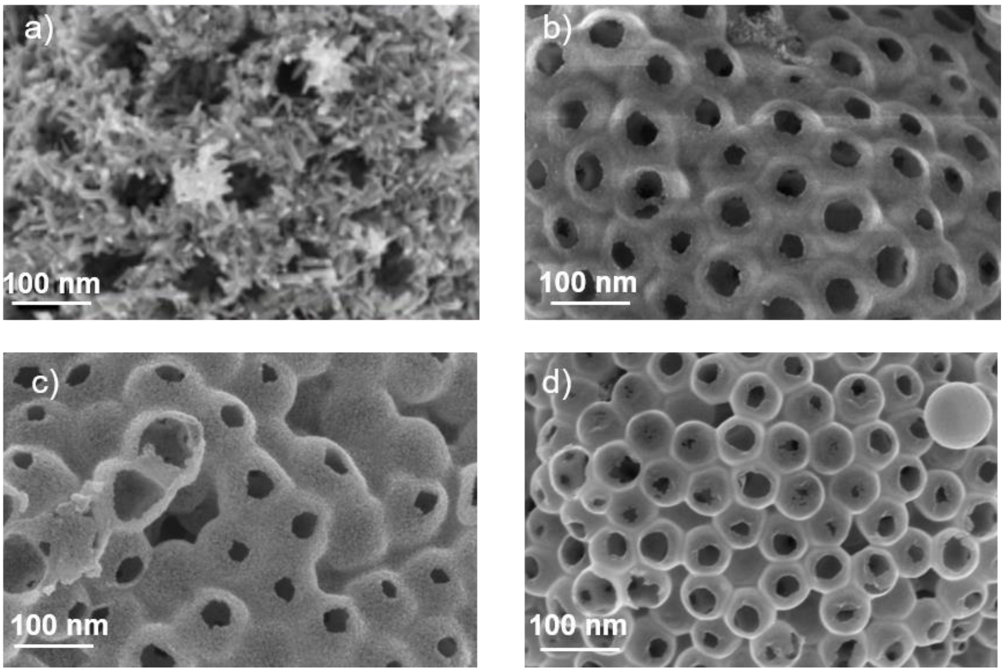

Figure 2.6 Comparison of SEM micrographs at 550° C between a) IrO_2[10], b) 10-Mo, c) 30-Mo and d) 50-Mo.

In addition, when comparing the SEM images with pure IrO_2 at 550 °C from the paper of *Faustini et al.,*[10], the morphology of the $Ir_{1-x}Mo_xO_2$ particles differs drastically to pure IrO_2. IrO_2 crystallizes into strongly anisotropic structures (nanoneedles) surrounding isotropic nanoparticles which compose the walls of the porous microspheres, these isotropic nanoparticles are present in our mixed oxide suggesting isotropic shape (Figure 2.6). This isotropic shape is also observed when comparing XRD patterns of the samples at the same calcination temperature (Figure 2.7d) where broader peaks are obtained with higher Mo content (yellow and purple lines). Also, a shift of the characteristic peaks (2θ = 30° - 45°) to the left or right against pure IrO_2 suggests an isotropic shape as well. For instance, Figure 2.7d highlights the shift of the (110) and (011) reflection peaks of 10, 30 and 50-Mo catalyst with increasing Mo content at 550° C when comparing to pure IrO_2. The arrows are indicating the shift direction in the peak position, (110) peak shifts towards lower values of 2θ values as the molybdenum content increases in the mixed oxide, while the (011) peak shifts towards higher values of 2θ. This change is clearly evidenced by an increase of the *a*-parameter associated to a decrease in the *c*-parameter as depicted in Figure 2.7a and b.

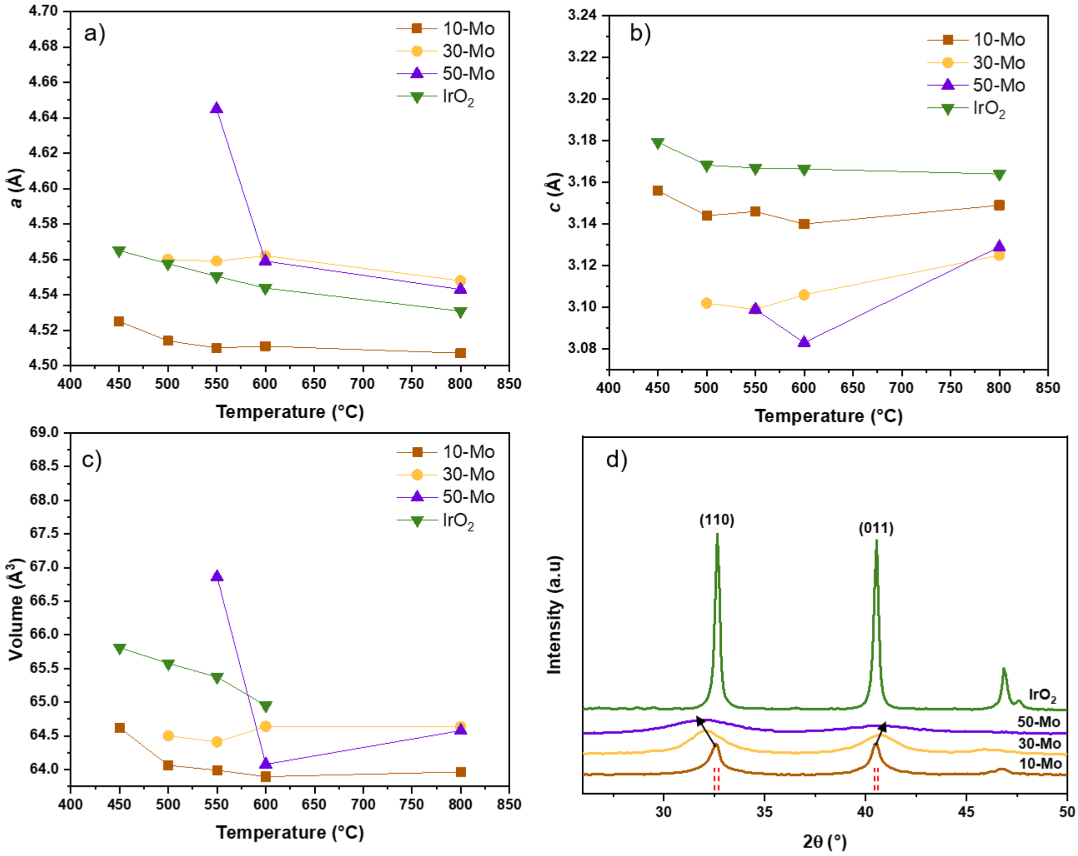

Figure 2.7 a-c) Evolution of cell parameters of Ir1-xMoxO2 (x = 0, 0.1, 0.3, 0.5), and d) Zoom of XRD patterns of samples calcined at 550° C highlighting the (110) and (011) reflection peaks.

The evolution of the cell parameters of 10, 30 and 50-Mo samples as temperature is increased is displayed in Figure 2.7, while taking as a reference pure IrO_2.[10] As observed in Figure 2.7a and c, the *a*-parameter and lattice volume progressively increase with the molybdenum concentration, while the *c*-parameter decreases. The main oxidation state present on the mixed oxides regarding iridium is depicted in Figure 2.8 and is obtained by XPS (focus on the surface) and XANES (focus on the bulk) spectra, both techniques demonstrating that the same oxidation state is present in the surface as in the bulk. Based on this, the slight change of the parameters and lattice volume as the calcination temperature increases (despite the molybdenum content) can be explained by the substitution of Ir^{3+}/ Ir^{4+} or Ir^{4+} ($R^{VI}_{Ir^{3+}}$ = 0.82 Å; $R^{VI}_{Ir^{4+}}$ = 0.765 Å[34]) for Mo^{6+} ($R^{IV}_{Mo^{6+}}$ = 0.55 Å[34]), Mo^{5+} ($R^{IV}_{Mo^{5+}}$ = 0.60 Å[34]) or Mo^{4+} ($R^{VI}_{Mo^{4+}}$ = 0.79 Å[34]).

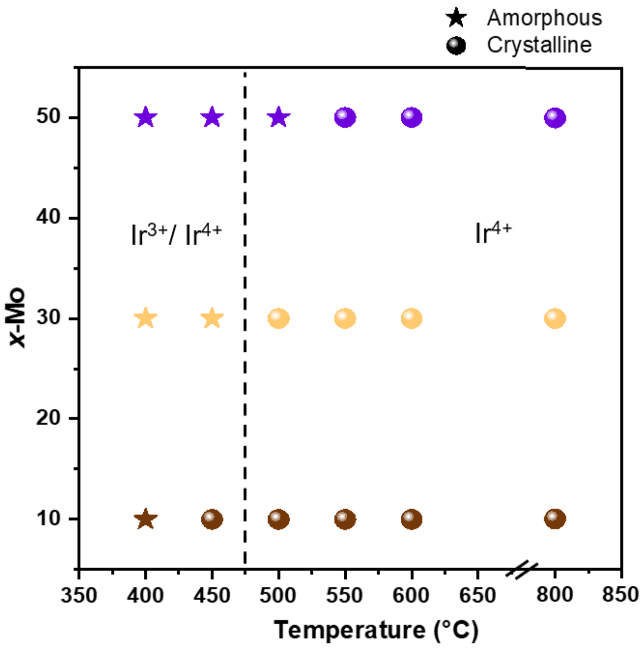

Figure 2.8 Graphical representation of Ir main oxidation state and identification of amorphous and crystalline samples for the x-Mo content as a function of calcination temperature.

Overall, the percentage of variation of *a*-parameters with respect to pure IrO_2 for 10-Mo is in the decrease in the range 0.8-0.5%, for 30-Mo an increase between 0.1-0.5%, and for 50-Mo an increase of 2.1-0.9% as temperature increases. On the other hand, the percentage of variation of *c*-parameters are all in a decrease with respect to pure IrO_2 for 10-Mo in the range 0.7-0.5%, for 30-Mo between 2.2-1.2%, and for 50-Mo between 2.6-1.1% as temperature increases (Table 2.1). However, the decrease in the volume as temperature increases (despite the molybdenum percentage), is mainly influenced by the slight decrease of the *a*-parameter, for instance at 10-Mo from 4.52 to 4.50 Å, while the *c*-parameters remain almost constant. This behaviour is congruent by the previously reported material by *Faustini et al.*,[10] In the case of 70-Mo (Table 2.1), despite of presenting the coexistence of two phases in the range 400-600° C the *a* and *c*-parameters remain constant, except at 800° C where an increase of 0.45% in the *a*-parameter, and a decrease of 1.3% in the *c*-parameter are observed with respect to pure IrO_2.

***a*-parameter (Å)**						
		Temperature (°C)				
Samples	**x**	**450**	**500**	**550**	**600**	**800**
IrO$_2$[10]	**0**	4.565	4.5576	4.5505	4.5438	4.5308
10-Mo	**0.1**	4.525	4.514	4.51	4.511	4.507
30-Mo	**0.3**	-	4.56	4.559	4.562	4.548
50-Mo	**0.5**	-	-	4.645	4.559	4.543
70-Mo	**0.7**	4.505	4.505	4.505	4.505	4.551
***a*-parameter variation %**	**0.1**	0.88	0.96	0.89	0.72	0.53
	0.3	-	0.05	0.19	0.40	0.38
	0.5	-	-	2.1	0.3	0.3
	0.7	1.31	1.15	1.00	0.85	0.45

***c*-parameter (Å)**						
		Temperature (°C)				
Samples	**x**	**450**	**500**	**550**	**600**	**800**
IrO$_2$[10]	**0**	3.1793	3.1683	3.1669	3.1664	3.164
10-Mo	**0.1**	3.156	3.144	3.146	3.14	3.149
30-Mo	**0.3**	-	3.102	3.099	3.106	3.125
50-Mo	**0.5**	-	-	3.099	3.083	3.129
70-Mo	**0.7**	3.159	3.159	3.159	3.159	3.123
***c*-parameter variation %**	**0.1**	0.73	0.77	0.66	0.83	0.47
	0.3	-	2.09	2.14	1.91	1.23
	0.5	-	-	2.14	2.63	1.11
	0.7	0.64	0.29	0.25	0.23	1.30

Volume (Å^3)						
		Temperature (°C)				
Samples	**x**	**450**	**500**	**550**	**600**	**800**
IrO$_2$[10]	**0**	66.25	65.81	65.58	65.37	64.95
10-Mo	**0.1**	64.62	64.06	63.99	63.90	63.97
30-Mo	**0.3**	-	64.50	64.41	64.64	64.64
50-Mo	**0.5**	-	-	66.86	64.08	64.58
70-Mo	**0.7**	64.11	64.11	64.11	64.11	64.68

Table 2.1. Structural parameters for Ir$_{1-x}$Mo$_x$O$_2$ (x = 0, 0.1, 0.3, 0.5, 0.7) calculated by Rietveld refinement from X-ray diffraction data (space group *P42/mnm*).

Figure 2.9 presents the crystallite size, determined from Rietveld refinement when possible, for each composition and each calcination temperature. As mentioned earlier, when comparing samples at the same calcination temperature, broader peaks are obtained with higher Mo content, i.e. broader peaks are equivalent to smaller crystallites. Therefore, for a same calcination temperature, smaller crystallites are expected as the molybdenum content increases. For instance, at 500 °C, the crystallite size decreases with increasing molybdenum content as follow: 9.9 > 7 > 2 > 1 ≥ 1 nm for IrO_2, 10-Mo, 30-Mo, 50 and 70-Mo, respectively. This was also reported by *Cheng et al.,*[7] where a decrease in crystallite size from 4.2 nm to 2.1 nm was obtained when molybdenum was introduced to the $Ir_{0.4}Ru_{0.6}O_2$ composite. On the other hand, in the whole range of temperature studied, as the temperature of calcination increases the crystallite size increases as well, since diffraction peaks become narrow due to sintering effects, as in the case of 10-Mo passing from 2 nm at 450 °C to 11 nm when the temperature reaches 800 °C. In addition, to understand the behavior of 70-Mo, the crystallite size was compared to the one of the single phases MoO_3 sintered independently in the range of temperatures 400 – 600 °C. These temperatures were selected since the MoO_3 phase forms when sintering 70-Mo at these temperatures. From Figure 2.9b, both materials present almost the same crystallite size suggesting that the molybdenum in excess present in the IrO_2 phase exhibits the same crystallite behavior as the 100-Mo.

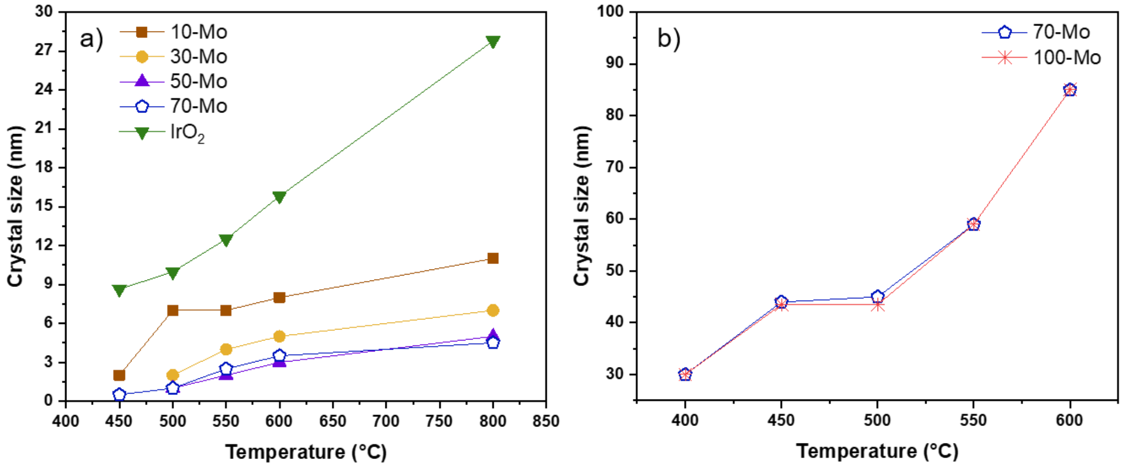

Figure 2.9 a) Evolution of the crystallite size of $Ir_{1-x}Mo_xO_2$ phase as a function of temperature. b) MoO_3 crystallite size evolution as function of temperature.

2.3. Conclusion

In this chapter, a series of $Ir_{1-x}Mo_xO_2$ oxides across the composition range x = 0, 0.1, 0.3, 0.5, 0.7 and 1 have been prepared using an aerosol route synthesis, the spray-drying technique. XRD Rietveld refinements indicated that the oxide powders are presenting a single rutile phase with space group *P42/mnm*, except 70-Mo where an additional phase of MoO_3 appears in an orthorhombic unit cell with *Pnma* space group. Single phases compounds were obtained for x = 0.1, 0.3 and 0.5 starting from the sintering temperatures of 450, 500 and 550 °C, respectively. This showed that the addition of molybdenum delays the crystallization while, in contrast, samples with x = 0.7 present the coexistence of $Ir_{1-x}Mo_xO_2$ and MoO_3 phases at any sintering temperature. In addition, SEM analysis showed that all compositions presented a smooth transition from amorphous surface at low temperatures with high porosity, to particle-like morphology at high temperatures. Samples with Mo > 10% do not present needle like particles, and clear MoO_3 crystals (platelet form) are observed only at 70-Mo in the range 400 – 600°C. Finally, XRD analysis also showed that the crystallite size increases with temperature but decreases with molybdenum content.

The success in producing single phases in the $Ir_{1-x}Mo_xO_2$ series and the physical characterizations allowed to continue with the electrochemical measurements presented in chapter 3 and chapter 4 allowing to understand the behavior when subjecting the samples to electrochemical characterizations.

2.4. References

1. Larissa, B., Copper(I) complexes as emitting materials. In *New Emitters for OLEDs: The coordination- and photo-chemistry of mononuclear neutral copper(I) complexes*, Logos Verlag Berlin GmbH: Berlin, 2016.
2. Kasian, O., et al., On the Origin of the Improved Ruthenium Stability in RuO_2–IrO_2 Mixed Oxides. *J. Electrochem. Soc.*, 2016, *163* (11), F3099-F3104.
3. Audichon, T., et al., Effect of Adding CeO_2 to RuO_2–IrO_2 Mixed Nanocatalysts: Activity towards the Oxygen Evolution Reaction and Stability in Acidic Media. *ChemElectroChem*, 2015, *2* (8), 1128-1137.
4. Kim, Y. T., et al., Balancing activity, stability and conductivity of nanoporous core-shell iridium/iridium oxide oxygen evolution catalysts. *Nat Commun*, 2017, *8* (1), 1449.
5. Kripasindhu Sardar, et al., Bismuth iridium oxide oxygen evolution catalyst from hydrothermal synthesis. *Chem. Mater.*, 2012, *24*, 4192-4200.
6. Morimitsu, M.; Oshiumi, N., Accelerated Oxygen Evolution and Suppressed MnOOH Deposition on Amorphous IrO_2–Ta_2O_5 Coatings. *Chem. Lett.*, 2009, *38* (8), 822-823.
7. Jinbin Cheng, et al., Preparation of $Ir_{0.4}Ru_{0.6}Mo_xO_y$ for oxygen evolution by modified Adams' fusion method. *Int. J. Hydrogen Energy*, 2009, *34*, 6609-6613.
8. Audichon, T., et al., Preparation and characterization of supported $Ru_xIr_{(1-x)}O_2$ nano-oxides using a modified polyol synthesis assisted by microwave activation for energy storage applications. *Appl. Catal. B*, 2017, *200*, 493-502.
9. Fiévet, F., et al., The polyol process: a unique method for easy access to metal nanoparticles with tailored sizes, shapes and compositions. *Chem. Soc. Rev.*, 2018, *47* (14), 5187-5233.

10. Faustini, M., et al., Hierarchically Structured Ultraporous Iridium-Based Materials: A Novel Catalyst Architecture for Proton Exchange Membrane Water Electrolyzers. *Adv. Energy Mater.*, 2019, *9* (4), 1802136.
11. Indra, A., et al., Unification of Catalytic Water Oxidation and Oxygen Reduction Reactions: Amorphous Beat Crystalline Cobalt Iron Oxides. *J. Am. Chem.Soc*, 2014, *136* (50), 17530-17536.
12. Otogawa, R., et al., Effects of microstructure of IrO_2-based anodes on electrocatalytic properties. *Electrochim. Acta*, 1998, *44* (8), 1509-1513.
13. Blakemore, J. D., et al., Comparison of amorphous iridium water-oxidation electrocatalysts prepared from soluble precursors. *Inorg. Chem.*, 2012, *51* (14), 7749-63.
14. Blakemore, J. D., et al., Characterization of an amorphous iridium water-oxidation catalyst electrodeposited from organometallic precursors. *Inorg. Chem.*, 2013, *52* (4), 1860-71.
15. Smith, R. D. L., et al., Facile Photochemical Preparation of Amorphous Iridium Oxide Films for Water Oxidation Catalysis. *Chem. Mater.*, 2014, *26* (4), 1654-1659.
16. Anantharaj, S.; Noda, S., Amorphous Catalysts and Electrochemical Water Splitting: An Untold Story of Harmony. *Small*, 2020, *16* (2), e1905779.
17. Peng, K., et al., Emerging hierarchical ternary 2D nanocomposites constructed from montmorillonite, graphene and MoS_2 for enhanced electrochemical hydrogen evolution. *Chem. Eng. J.*, 2020, *393*.
18. Ren, J.-T., et al., Molybdenum-based nanoparticles (Mo_2C, MoP and MoS_2) coupled heteroatoms-doped carbon nanosheets for efficient hydrogen evolution reaction. *Appl. Catal. B: Environmental*, 2020, *263*.
19. Li, Y., et al., Current progress of molybdenum carbide-based materials for electrocatalysis: potential electrocatalysts with diverse applications. *Mater. Today Chem.*, 2021, *19*.
20. Zhang, M., et al., Porous molybdenum trioxide as a bifunctional electrocatalyst for oxygen and hydrogen evolution. *J. Electroanal. Chem.*, 2019, *836*, 102-106.
21. Tariq, M., et al., Unraveling the Beneficial Electrochemistry of IrO_2/MoO_3 Hybrid as a Highly Stable and Efficient Oxygen Evolution Reaction Catalyst. *ACS Sustain. Chem. Eng.*, 2018, *6* (4), 4854-4862.
22. Shi, Q., et al., Robust noble metal-based electrocatalysts for oxygen evolution reaction. *Chem. Soc. Rev.*, 2019, *48* (12), 3181-3192.
23. Saji, V. S.; Lee, C. W., Molybdenum, molybdenum oxides, and their electrochemistry. *ChemSusChem*, 2012, *5* (7), 1146-61.
24. Odziomek, M., et al., Aerosol synthesis of thermally stable porous noble metals and alloys by using bi-functional templates. *Materials Horizons*, 2019, *in press*.
25. Zhou, Z., et al., Cultivating crystal lattice distortion in IrO_2 via coupling with MnO_2 to boost the oxygen evolution reaction with high intrinsic activity. *Chem. Commun.*, 2018, *54* (39), 4959-4962.
26. Wang, S.; Langrish, T., A review of process simulations and the use of additives in spray drying. *Food Res. Int.*, 2009, *42* (1), 13-25.
27. Peron, J., et al., Hollow iridium-based catalysts for the oxygen evolution reaction in proton exchange membrane water electrolyzers. *ECS Trans.*, 2017, *80* (8), 1077-1084.
28. Debecker, D. P., et al., Aerosol processing: a wind of innovation in the field of advanced heterogeneous catalysts. *Chem. Soc. Rev.*, 2018, *47*, 4112-4155.
29. Lutterotti, L., et al., MAUD: a friendly Java program for material analysis using diffraction. *IUCr: Newsletter of the CPD*, 1999, *21*, 14-15.
30. Ferroni, M., et al., Selective sublimation processing of a molybdenum–tungsten mixed oxide thin film. *J. Vac. Sci. Technol.*, 2003, *21* (4).
31. Medvedev, A. S.; Malochkina, N. V., Sublimation of molybdenum trioxide from exhausted catalysts employed for the purification of oil products. *Russ J. Non-Ferr Met*, 2007, *48* (2), 114-117.

32. Boissiere, C., et al., Aerosol Route to Functional Nanostructured Inorganic and Hybrid Porous Materials. *Adv. Mater.*, 2011, *23* (5), 599-623.
33. Liu, Y., et al., Investigation of high-performance IrO_2 electrocatalysts prepared by Adams method. *Int. J. Hydrogen Energy*, 2018.
34. Shannon, R. D., Revised effective ionic radii and systematic studies of interatomic distances in halides and chalcogenides. *Acta Cryst. A*, 1976, *32* (5), 751-767.

CHAPTER 3. ELECTROCATALYTIC PERFORMANCES OF $Ir_{1-x}Mo_xO_2$ AS ANODE MATERIAL

Following the structural and morphological study of the $Ir_{1-x}Mo_xO_2$ (x = 0, 0.1, 0.3, 0.5, 0.7 and 1) family presented in chapter 2, this chapter describes the electrochemical performances of all Ir-Mo oxides as electrocatalyst materials for proton exchange water electrolyzers. The first part concerns the description of the electrochemical characterization techniques and parameters, as well as a brief description of the rotating disk electrode (RDE) device as a tool to run these techniques. In the second part, cyclic voltammetry (CV) and chronopotentiometry tests are used to evaluate the electrochemical behavior of Ir-Mo oxides in acidic solution as function of the catalyst calcination temperature and composition.

3.1. Introduction

Research on PEMWE is extensive, and their development has been continuous, firstly because such technology offers a high efficiency in H_2 production for further being used in electricity storage and generation applications. However, despite some remarkable advantages, the large-scale development of PEMWE as commercial devices depends strongly on the costs of the electrolyzer and reducing them is necessary. Therefore, to improve the devices it is important to go further in technological advances, such as the field of material science (i.e., electrocatalysts), to understand the catalytic reactions and to design new catalysts in order to offer more durability and develop cost-effective PEM electrolysis.[1, 2]

One key problem is the performance of the electrocatalysts, and notably the materials that carries out the OER, since the anode reaction is kinetically much slower than the cathode reaction, requiring greater overpotentials to drive the OER. The thermodynamics presented on chapter 1 give only the minimum potential required to carry out the process, but due to the reaction kinetics (i.e., mass transfer of reactants/products, electron transfer, chemical reaction, etc.) a higher potential is required for the reactions to carry on. This excess of energy is called the overpotential (η). Furthermore, the electrolyte presents ohmic voltage drops which arise from different factors: limitations in the cell design, electrolyte conductivity, distance between the electrodes.[3] The overpotential as well as the ohmic drop vary with current density, the ohmic losses increase linearly with the applied current, and the overpotential depends on both the slow mass transfer of reactants/products in the electrolyte and electron transfer limitations.[4, 5]

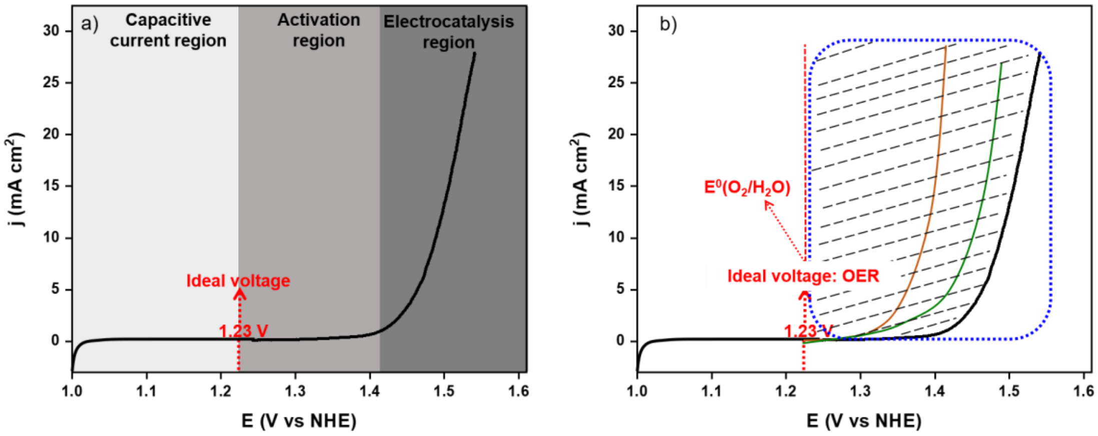

Figure 3.1 a) Schematic representation of a polarization curve in a water electrolyzer, and b) Graphical comparison of the optimal polarization curve of OER (red dotted line) with real polarization curves (brown, green and black lines).

Figure 3.1a represents a typical polarization curve for a water electrolyzer, where voltage (E) versus current density (j) of an electrochemical system is depicted. As the potential is applied, no current is detected up to 1.23 V (theoretical electrolysis voltage for water oxidation). At this point an additional voltage is required to overcome the resistances present in the system such sluggish reaction kinetics, losses due to ionic/electronic conduction (ohmic resistance) and mass transport. As η increases, the activation energy barrier is crossed, and the polarization curve becomes linear.[6, 7] On the other hand, in Figure 3.1b the blue square filled with black dashed lines represent the anodic overpotential. The current taken as reference to know this overpotential is 10 mA cm^{-2}, which is used as a requirement since it is the current density expected at the anode in a 10% efficient solar water splitting device.[8] Minimizing the overpotential value is crucial and is directly linked to the catalyst activity (i.e., catalyst type, loading, electrochemical surface area and stability). Then, the easiest way to compare different catalyst materials is to compare their polarization curves as in Figure 3.1b. A good catalyst will exhibit higher current density values, which translates as being more active at the desired potential for the electrode process.[6, 7, 9] Thus, accurate measurements for the OER activity of different materials is necessary.

3.1.1. Rotating disk electrode (RDE)

A powerful way for evaluating electrochemical reactions in a liquid environment that involves mass transport is by forcing convection under control conditions while rotating the electrode used. This device is called a rotating disk electrode (RDE), and it can provide a steady-state mass transport regime.[10, 11]

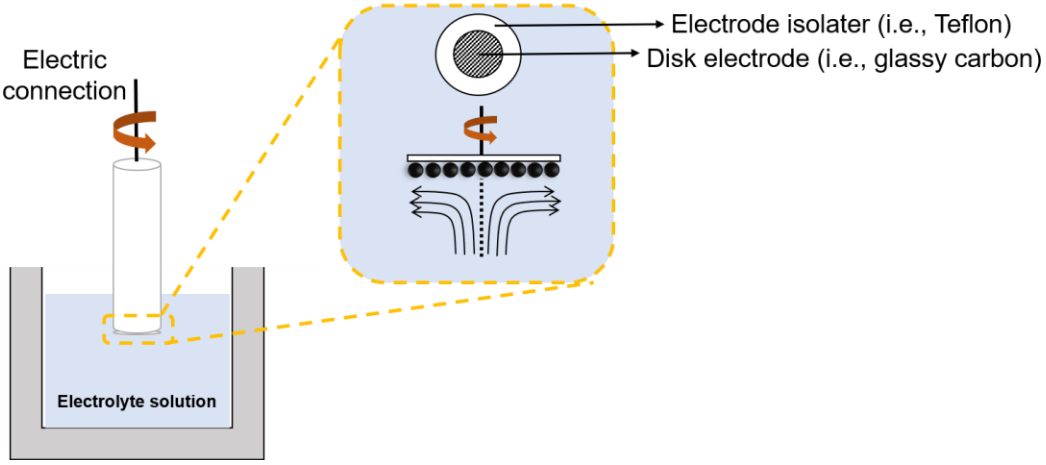

Figure 3.2 Scheme of a rotating disk electrode (RDE) and solution flow pattern near the disk electrode surface.

In a RDE experiments, as in Figure 3.2, the electrode surface is submerged in the electrolyte solution, and as the electrode starts to rotate the electrolyte is dragged up and by centrifugal force the solution flushed radially outwards across the surface of the disk.[12] This dragging motion and centrifugal force assures reproducibility of measurements since the convection, which depends on the rotation rate, makes it possible (only if the rotation rate is the same for each measurement). Another advantage is that by rotating the electrode the removal of gas products (i.e., bubbles of O_2 in our case) is efficient. However, if the gas bubble is not removed an effect of it is visible in the overpotential, which is attributed to an ohmic resistance, since the bubble is blocking the active surface area and results in limiting the current.[13] Electrochemical measurements using the RDE device involve steps such as electrode preparation, data collection and analysis as described in the following sections.

3.1.1.1. *Electrode preparation for OER measurements*

To evaluate the activity of the catalysts for OER, a glassy carbon (GC) electrode is usually employed, on which an electrocatalytic film is deposited from an ink, and a three-electrode cell setup is employed.

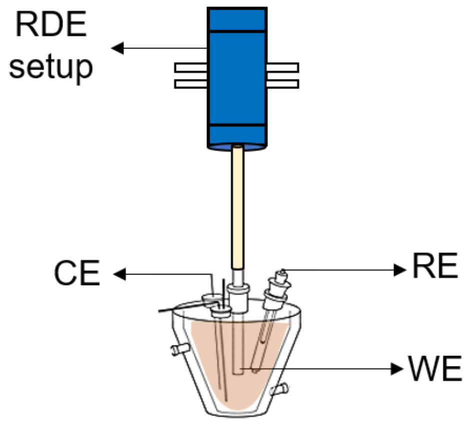

Figure 3.3 Schematic representation of the three-electrode cell

In a RDE electrochemical cell, the working electrode (WE) is rotating at the desired rotation rate and located in the middle of the electrolyte container. The cell presented in Figure 3.3, has three electrodes: (1) a GC working electrode coated with the catalyst of study, (2) a counter electrode (CE), typically platinum, and (3) a reference electrode (RE) such as normal hydrogen electrode (NHE), saturated calomel electrode (SCE) and others. All three electrodes are electrically connected through the potentiostat.[12, 14] The WE needs to be carefully prepared since a smooth surface is desired to deposit the electrocatalytic film. This is achieved by conscientious polishing (see chapter 6 for further explanation and detailed procedures).

a) Ink formulation, preparation, and deposition on WE

There are two major steps to coat the RDE: the preparation of the catalyst ink, followed by the coating of the catalyst on the surface of the glassy carbon electrode. The catalyst ink is the most important component when using RDE since the measurements depend strongly on the composition and quality of the film despite the functioning of the device. Typically, the catalyst ink contains the catalyst, the perfluorosulfonic acid (PFSA) ionomer, and a mixture of water and alcohol (dispersion solvent).[15] In order to formulate a proper ink, factors such as viscosity, evaporation rate, surface tension and homogeneity have to be taken into account to achieve the ink stability and obtain an homogenous film surface. The stability of the colloidal suspension is crucial for the particles to remain dispersed in the solvent, and this will be dictated by the concentration of ionomer, since a total coverage of the surface of the GC is needed. Interestingly, when comparing electrochemical performances that presented same ink components but different dispersion solvent showed that nature of the solvent affects the electrochemical response of the catalyst.[16] Once the catalyst ink complies with the aforementioned, a small amount of ink is pipetted and drop-casted onto the disk electrode surface. Then the coated electrode is left to dry under the conditions desired.[17]

3.2. Electrochemical techniques

When studying electrochemical reactions, a wide range of characterizations techniques can be used in order to obtain certain information such as kinetic parameters, thermodynamic of the reaction, redox couple actives, stability and activity as function of time, among others. The techniques used to obtain those, as mentioned previously and discuss in this thesis, are usually conducted in a three - electrode cell configuration.

3.2.1. Cyclic voltammetry (CV)

CV is one of the most frequently electrochemical technique employed in catalyst activity characterization, since it offers a wide range of experimental information. Furthermore, it is one of the most accessible techniques to employ since the acquisition and interpretation of the data only requires just a modest amount of time and ability.[18] For instance, it can quickly provide qualitative information such as the interaction of the catalyst with the electrolyte, reversibility of reactions, electrocatalytic processes, and others. The application of this technique in OER is very common as it can drive the reaction under different experimental conditions.[19] Figure 3.4a presents the potential wave of a CV measurement as function of time. The potential is swept linearly over time creating a slope, the scan rate, as the potential is swept between a lower potential, E_1, and an upper potential, E_2, while the current is recorded at the same time. For completing one cycle, the scan is reversed in order to reach E_1 again.[20]

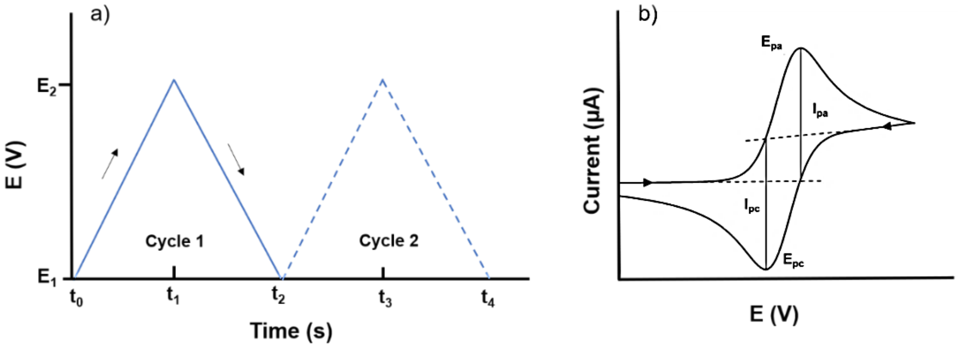

Figure 3.4 a) Typical waveform of the variation of potential as function of time during a CV and b) General CV of a species in solution (taken and modified from[21])

Figure 3.4b is the resulting graph, called cyclic voltammogram, of the current at the WE during the potential scans where the forward scan (left to right) and backward scan (right to left) curves are observed. In this case, the plot corresponds to a reversible oxidation-reduction system with electroactive species in solution, in which the upward peak indicates the oxidation of species and the downward peak indicates the reduction process.[20, 21] In addition, CV can also be used to characterize materials that are deposited on the surface of the WE. In this case, the cyclic voltammogram will show the current for double layer charging as well as the formation and dissolution of hydride and oxide layers on WE surface. Figure 3.5, gives an example of cyclic voltammograms of materials used for OER, such as IrO_2, RuO_2 and mixed Ir-Ru oxides.

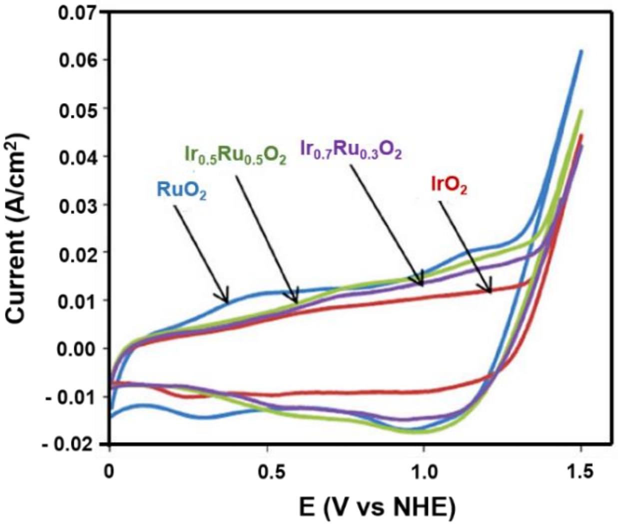

Figure 3.5 Typical CVs for IrO_2 and RuO_2, and mixed oxides $Ir_xRu_{1-x}O_2$ in 0.5 M H_2SO_4 at a scan rate of 50 mV s^{-1} (taken and modified from[22])

The materials in Figure 3.5 were prepared by hydrolysis method in alkali medium and deposited as thin-film layers onto the GC electrode to be tested in the potential range from 0 to 1.5 V vs NHE. The oxidation region also called catalytic region is found at potentials higher than 1.2 V vs NHE, where OER occurs. In addition, the peaks observed between 0 to 1.2 V vs NHE are consequences of the redox transitions of the iridium or ruthenium oxygen species adsorbed on the surface which leads to the ejection of protons and electrons.[22] Furthermore, it can be observe that cyclic voltammograms depend strongly of the material compositions as well as of the nature of the electrolyte in which they are submerged and the pH value of the media.

3.2.2. Polarization curves

Polarization curves are usually obtained by linear sweep voltammetry (LSV), as in a CV measurement, a constant potential sweep rate is applied, and the current is recorded. In contrast to CV, LSV commonly works at slow scan rates since steady-state conditions are desired.[18] The potential in this case starts where no electrode reaction occurs and moves towards catalytic potentials. Figure 3.6a shows as in CV that the potential changes linearly with time from E_1 to E_2, and the current-potential curve displays the shape of an exponential curve as in Figure 3.6b.[23]

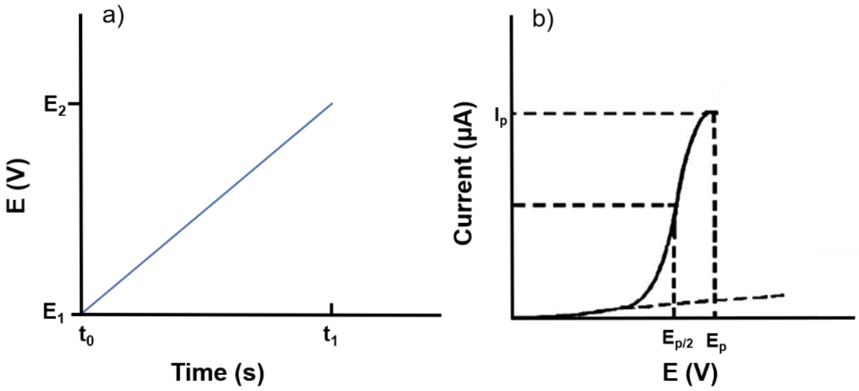

Figure 3.6 a) Typical waveform of the variation of potential as function of time during a LSV and b) General LSV current-potential plot (taken and modified from[23]).

LSV curves, as mentioned previously in section 3.1, are useful to compare different catalyst materials as in Figure 3.7a. An extension of LSV, is the Tafel equation. It is obtained when the net current follows the Butler-Volmer equation (Eq. 3-1), meaning that the kinetics of the reaction are determining the overpotential:[24]

$$i = i_c + i_a = i_0\left(e^{-\frac{\alpha_c nF}{RT}\eta} - e^{\frac{\alpha_a nF}{RT}\eta}\right) \qquad \textit{(Eq. 3-1)}$$

The subscripts *c* and *a* refers to cathodic and anodic, respectively, and α is the charge transfer coefficient. When large overpotentials are present, the smaller contribution of either part cathodic or anodic currents can be neglected. For instance, the anodic reaction total current can be written as Eq. 3-2 and simplified to Eq. 3-3:[24]

$$i = i_a = i_0\left(e^{\frac{\alpha_a nF}{RT}\eta}\right) \qquad \textit{(Eq. 3-2)}$$

$$\eta = b \log\left|\frac{i}{i_0}\right| = a + b\log|i| \qquad \textit{(Eq. 3-3)}$$

Eq. 3-3 is the Tafel equation, and can be used in a LSV since in the linear part present on the polarization curves follows Eq. 3-3.[25] This equation is a linear correlation between log |i| and the overpotential (η), where *b* is the Tafel slope. Thus, the Tafel slope can be easily determined, and plotted as potential versus the logarithm of the current (Figure 3.7b). Also, i_0 or j_0, is a measure of the catalytic activity, a high value of i_0 corresponds to high electrocatalytic activity. However, sometimes it can be difficult to determine.

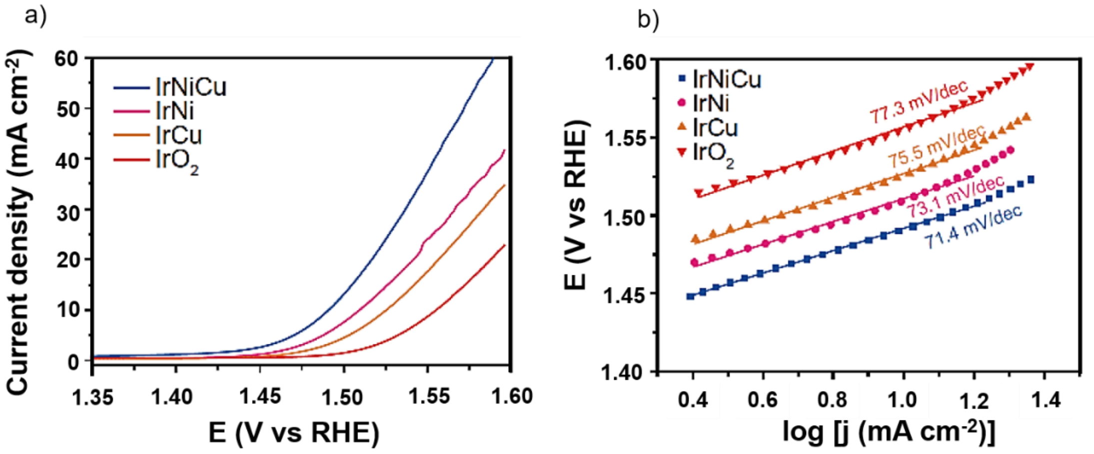

Figure 3.7 a) LSV curves for OER performance and b) Tafel plots of different iridium-based multimetallic alloy (taken and modified from[26]).

From Figure 3.7, the LSV curves and Tafel slopes correspond to the OER activity of different iridium-based metal alloys compared versus state-of-art IrO_2 materials. It can be seen from Figure 3.7a that IrNiCu and IrCu are the ones presenting the lowest η_{10} = 262 mV and highest η_{10} = 296 mV overpotentials, respectively. Also, all the materials exhibit a better performance than that of commercial IrO_2 (η_{10} = 326 mV). As complementary in Figure 3.7b, IrNiCu exhibits the lowest Tafel slope of 71.4 mV/dec. Therefore, it can be easily implied that among all, IrNiCu confirms its high OER electrocatalytic activity since it presents low Tafel slope value and high exchange current densities at low overpotential.[26] On the other hand, as a limitation, Tafel slopes are only reliable for comparison if the materials are measured under the same conditions (i.e., electrolyte composition, electrode geometry, etc).[25]

3.2.3. Step voltammetry technique

In step voltammetry, chronoamperometry (CA) and chronopotentiometry (CP) are used in electrochemical characterization of catalysts to observe their activity and/or stability as function of time while applying a constant current or potential as they operate under OER (or HER) conditions. In CA, the current is measured as function of time as the potential step takes place (Figure 3.8a), which means holding the potential of the WE constant. For CP, as a current step is applied, the current is maintained and the change of potential is recorded with time (Figure 3.8b).[27] The desired potential to apply during a CA should be extracted from CV/LSV measurements while for CP the current to apply is presumably known and should be able to deliver a potential without forcing the electrodes (i.e., 10 mA cm^{-2} for OER).[28]

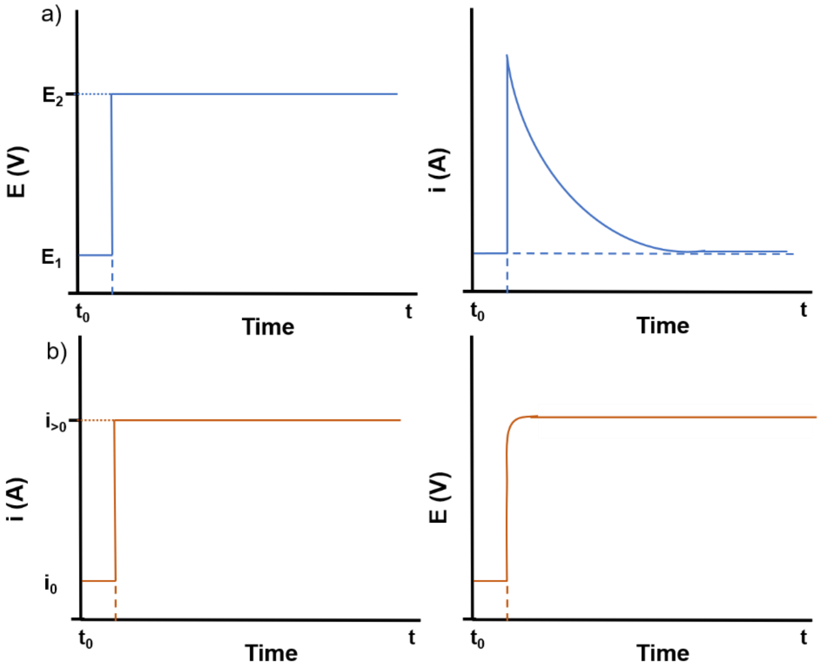

Figure 3.8 a) Waveform of a potential step with its respective chronoamperometry response, and b) Waveform of a current step with the corresponding chronopotentiometry response.

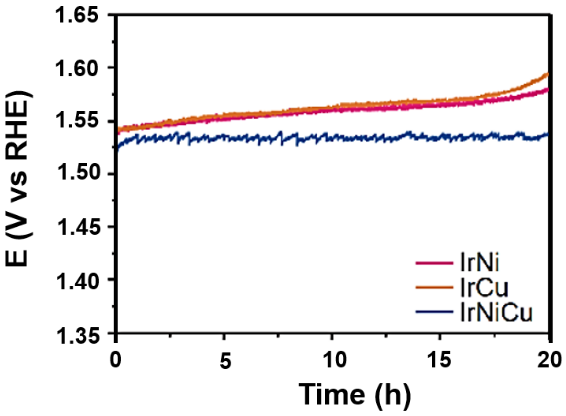

Figure 3.9 Chronopotentiometry curves of different iridium-based multimetallic alloy at constant current density (taken and modified from[26]).

Chronoamperometry and chronopotentiometry find their applicability in processes like electrolysis, and study of stability over time of electrochemical systems. However, most of the stability measurements in literature are performed by CA, but CP is still used as well.[28] The use of each technique relays on the information that wants to be extracted such for how long the catalyst can hold a potential to show a desired current or for how long the catalyst can exhibit the same voltage while holding a known current. An example of chronopotentiometry is presented by *Zhang et al.,*[26] in Figure 3.9 to show the stability of some catalysts. It is shown that after 20 h it is possible to observe that the voltage is increased for IrCu and IrNi as compared to IrNiCu, which can be interpreted as IrNiCu exhibits acceptable durability in the solution (acidic conditions in this case).

3.3. Electrochemical characterization

Based on the above, this section presents the following experimental conditions that were taken into account to test the performance of the synthesized materials presented in chapter 2, Ir-Mo oxides, as anode materials for PEMWE. The electrochemical characterizations were performed by CV and chronopotentiometry tests to determine the best catalyst among the $Ir_{1-x}Mo_xO_2$ family.

3.3.1. Experimental section

For all electrochemical measurements, a three-electrode set up was employed with a RDE. The WE was a glassy carbon (GC) electrode with a surface are of 0.1963 cm^2 (5 mm in diameter), a saturated calomel electrode (SCE) as the RE and a Pt wire as the CE. All three were submerged in a 0.05 mol L^{-1} H_2SO_4 solution as supporting electrolyte. The collection of data was done using a potentiostat Autolab PGSTAT 12 (see chapter 6 for further specifications). All graphs are reported in V vs normal hydrogen electrode (NHE) applying a correction of +0.242 V as compared to the measured potential vs SCE.

3.3.1.1. Ink formulation and electrode coating

The inks for coating the electrode were prepared by mixing the corresponding $Ir_{1-x}Mo_xO_2$ powder (1 mg) with (2 mg) Vulcan carbon, (250 µL) deionized water and (250 µL) nafion solution. This solution is mixed in an ultrasonic bath for 30 minutes to form a homogenous suspension. 8 µL of the ink was drop-casted onto the GC electrode surface by a volumetric pipette and left to dry in air until no wet finish was observed. Finally, the electrode was placed in an oven at 60 °C for 30 minutes. Prior to the ink coating, the GC electrode was polished to a mirror finish with different diamond suspensions and washed in an ultrasonic bath between experiments.

3.3.1.2. CV measurements

For each catalyst, the following experimental procedure was employed:

i. iR-drop compensation was measured by potential feedback. A value of ca. 30 Ω was obtained and compensated in all cases.
ii. The catalyst was cycled between -0.2 and 1.2 V vs NHE at a scan rate of 200 mV s^{-1}, typically 50 times.
iii. A forward scan, following the 50th scan, between 1.24 and 1.54 V vs NHE at scan rate of 10 mV s^{-1} was obtained to measure the OER.
iv. Step (i) and (ii) were repeated until the CV curve started to drop.

During these measurements, the electrode was rotate at 1600 rpm, and for reproducibility, the measurements were done at least 4 independent times for each sample.

3.3.1.3. Stability measurements

The chronopotentiometry technique was used as stability test. A constant current of 1 mA (corresponding to a current density of 5.09 mA cm^{-2}) was held for 12 hours for catalysts that exhibit favorable OER responses.

3.4. Results and discussion

3.4.1. Influence of catalyst ink parameters towards OER.

The OER catalytic activities of new electrocatalysts are usually screened by drop-casting thin-films on RDE. The usefulness of this methodology is that small amounts of catalyst can be rapidly tested and compared with different materials. Therefore, obtaining reliable results are necessary, which are strongly depending on the uniformity of the thin-films. Then, producing high quality catalyst films onto the surface of the WE are essential. The electrocatalytic films are made by casting a suspension of the catalyst onto a GC disk electrode and dried by a stationary method (i.e., covering with a beaker, drying under low flow of N_2, or placed directly in an oven). As the ink is drying, properties such as evaporation must be taken into account since it is link to the solvent content of ink.[29]

Based on the above and on the components that make up an ink mentioned in chapter 6, to achieve high quality catalyst films of $Ir_{1-x}Mo_xO_2$ the following parameters were considered: solvent/Nafion ratio, drying temperature, and time in the oven. These parameters were chosen based on the conditions used by *Faustini et al.,[30]* since the Ir-Mo particles were obtain by the same route of synthesis. Thus, these conditions are used as a reference: 1 mg of catalyst, 2 mg of Vulcan carbon XC72R, 250 µL of Nafion solution, and 250 µL of deionized water. The latter was then sonicated, and 8.8 µL of this suspension were deposited on the electrode surface, let dried in air and placed for 30 minutes at 100 °C in an oven.

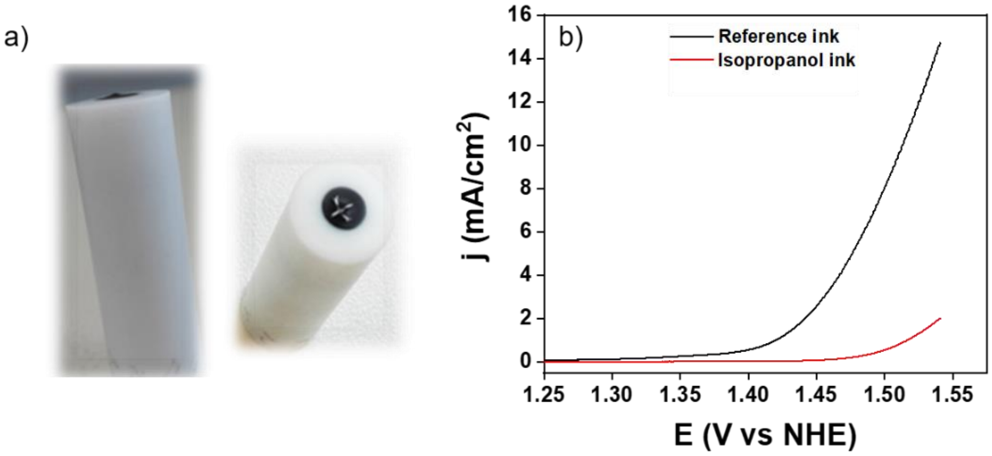

Figure 3.10 a) Surface of GC with nafion ink and b) Comparison between reference ink[30] and the ink that contains isopropanol.

As a first approach since catalysts are typically dispersed in a water/alcohol/ionomer,[31] the first test was to disperse the commercial IrO_2 in just 250 µL of Nafion. Isopropanol was not considered since the Nafion solution already contains some, however, it was not possible to perform any measurement due to the cracking and peeling off the film while it was drying as observed in Figure 3.10a. This proved that the addition of a solvent is compulsory, thus, 250 µL of isopropanol was added in order to maintain the same ratio as found in the literature. From Figure 3.10b, while keeping drying conditions the same, the ink that contains the alcohol exhibit a lower OER performance compared against the original ink from *Faustini et al.,*[30]*.* Therefore, the ink formulation was not modified and was kept the same for further measurements.

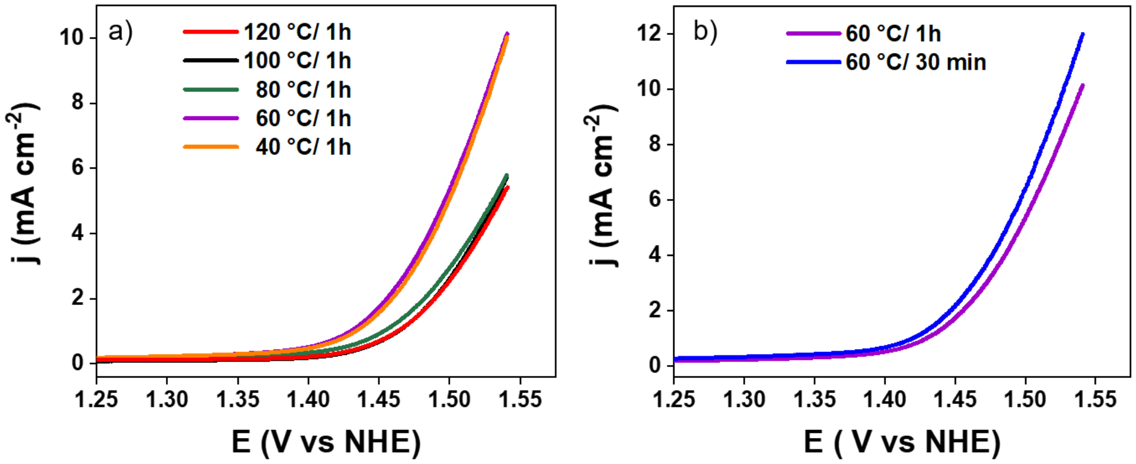

Figure 3.11 Cyclic voltammograms recorded at 10 mV s^{-1} of commercial IrO_2 a) different drying temperatures and b) comparison at 60 ºC with different drying time.

Based on those conclusions, the second test was to determine the optimum drying temperature and time of the electrode in the oven. For this, the 100 ºC/30 min employed by *Faustini et al.*,[30] was used as a reference. Firstly, the temperature was increased every 20 ºC starting from 40 ºC until reaching 120 ºC, and the time in the oven was increased from 30 min to 1 hour. As observed in Figure 3.11a, from all the measurements the films dried at low temperature such as 40 and 60 °C were the ones that exhibit the best performance towards OER. These temperatures are commonly used for drying films and agrees with *Garsany et al.,*[31] while other authors let the electrode dry at room temperature.[26, 32] In addition, to observe the influence of the drying time in the oven, the 60 ºC temperature was selected to be tested for 30 min. As observed in Figure 3.11b with less drying time in the oven an enhance of the OER was obtained decreasing at least in 12 mV the overpotential.

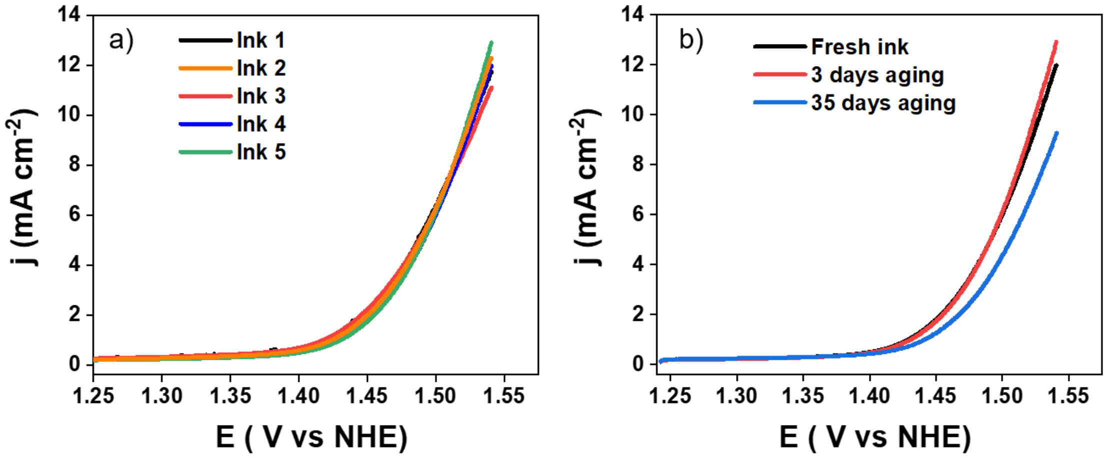

Figure 3.12 a) Comparison at 3 days of aging between five inks with the same composition and electrode preparation and b) Comparison between the first day preparation, 3 and 35 days of aging using the same ink and electrode preparation.

In addition, the aging of the ink to make reproducible tests was studied. For this, five inks were prepared the same day and measured after 3 days (Figure 3.12a) and one of them after 35 days (Figure 3.12b). This procedure was used to know how many times an ink could be used to make measurements and be comparable to each other, thus a daily ink preparation would not be necessary. From Figure 3.12, is possible to observe that a fresh ink is good to be used up to for 3 days in row to ensure good reproducibility. Therefore, using these experimental parameters we proceeded to test the $Ir_{1-x}Mo_xO_2$ samples using the ink formulation by *Faustini et al.,*[30] and for reproducibility tests the ink was used within 3 days.

3.4.2. Electrochemical evaluation

As in chapter 2, the mixed oxides are labelled as *x*-Mo@*T*, where *x* corresponds to the mole percentage content of molybdenum in the sample, and *T* represents the calcination temperature that corresponds to that *x* content. Commercial IrO_2 (IrO_2, 99.99%, Alfa Aesar) and pure IrO_2 prepared by spray drying were selected to provide a baseline for studying the performance of the Ir-Mo oxides catalysts. In the first part of the study, CV was used to characterize the current-voltage performance of the catalysts towards OER. The focus of the second part was on constant current electrolysis on the best catalysts from the CV analysis with the aim to determine their stability.

3.4.2.1. *CV analysis*

All the samples are compared to the OER activity of commercial IrO_2 since it is widely used for PEMWE as well as pure IrO_2 spray material calcined at 450 °C.[30] When studying OER, the lower the potential at a current density of 10 mA cm^{-2} the better the catalyst performance is as mentioned in section 3.1.

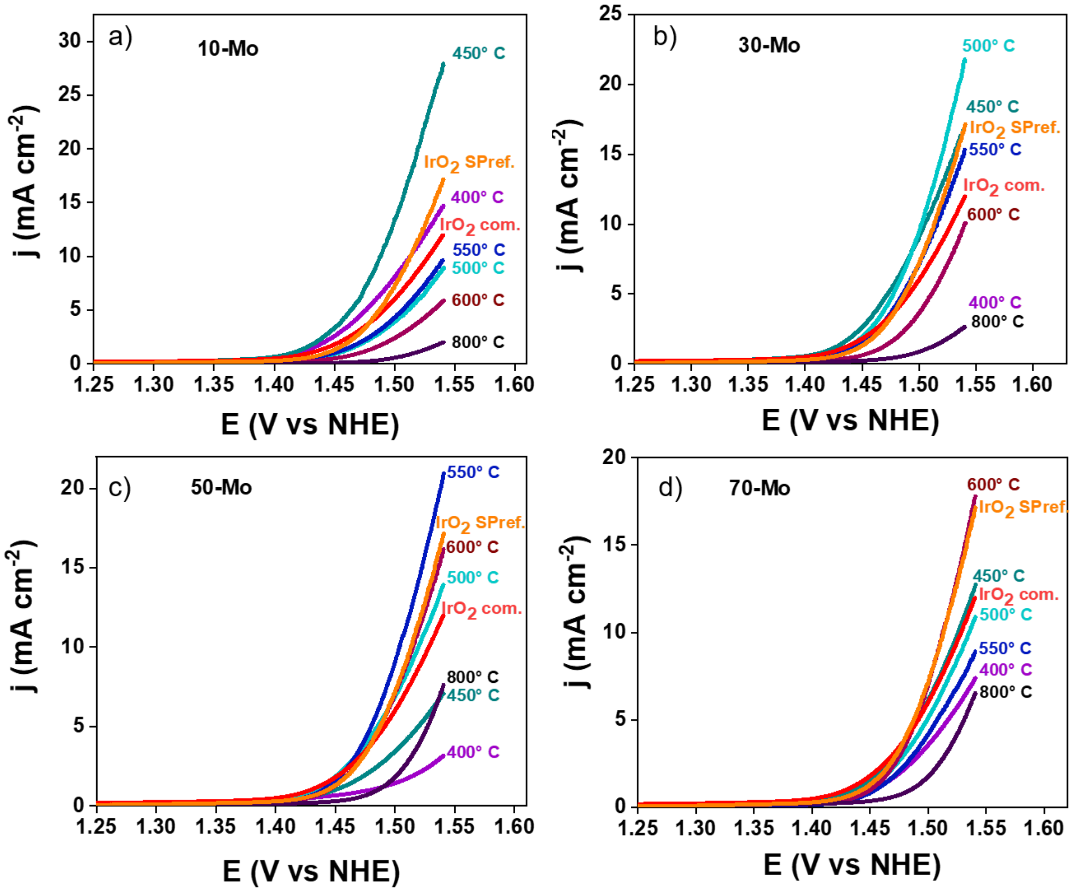

Figure 3.13 Cyclic voltammograms forward scan recorded at 10 mV s^{-1} of $Ir_{1-x}Mo_xO_2$ samples obtained after calcination in air at different temperatures.

All catalysts used in this part were characterized in 0.05 M H_2SO_4 by cyclic voltammetry. Cyclic voltammograms for all four molybdenum compositions are all given in Figure 3.13. The behavior observed in Figure 3.13a is in agreement with *Faustini et al.,*[30] for pure iridium oxide, where the calcination temperature strongly influences electrochemical performances, the lower calcination temperature leading to more active materials. In this case, the pure IrO_2 porous microspheres calcined at 400 and 450 °C were the ones that showed the highest activity towards OER. Furthermore, it is possible to observe that among all the samples, 10-Mo (Figure 3.13a) resembles the behavior reported for pure IrO_2 being 10-Mo@450 the one with the highest activity, and that at higher calcination temperatures the catalytic performance lowered gradually. *Cherevko et al.,*[33] reported the same trend for IrO_x films onto Ti substrate when calcined between 250 and 550 °C, and in this case the one calcined at 250 °C was found to be the most stable and active.

On the other hand, when observing 30-Mo (Figure 3.13b), 50-Mo (Figure 3.13c) and 70-Mo (Figure 3.13c), the trend changed compared to 10-Mo. The best performances in these cases are not the samples calcined at 400 or 450 °C, it is the opposite where the temperature at which each molybdenum content (above 10%) exhibited high activity was found to increase every 50 °C. Therefore, for samples 30, 50 and 70-Mo the best performances are at 500, 550 and 600°C, respectively. When observing carefully the samples calcined at 400 °C, for 30, 50 and 70-Mo, the activity dropped drastically when compared to 10-Mo@400, these samples performing poorly not even reaching 10 mA cm^{-2}. All samples calcined 800°C, despite the molybdenum content, did not reach either this value of current density. Thus, these samples were discarded for further studies.

When looking at each temperature individually it is visible that they behave differently as molybdenum content is increased. For instance, samples heated at 600 °C with Mo > 10%, performed better than at lower molybdenum content, reaching at least 10 mA cm^{-2} or higher. On the other hand, 500 and 550 °C seem to be temperatures at which mostly all the samples showed a good or acceptable activity towards OER.

To further understand the above behavior, and continuing with 10, 30 and 50-Mo series, we compared the OER activity at 1.5 V vs NHE as function of calcination temperature as depicted in Figure 3.14a. No further analysis was done on samples with 70-Mo, despite the good performances towards OER, since those materials present a mixture of phases as mentioned previously in chapter 2.

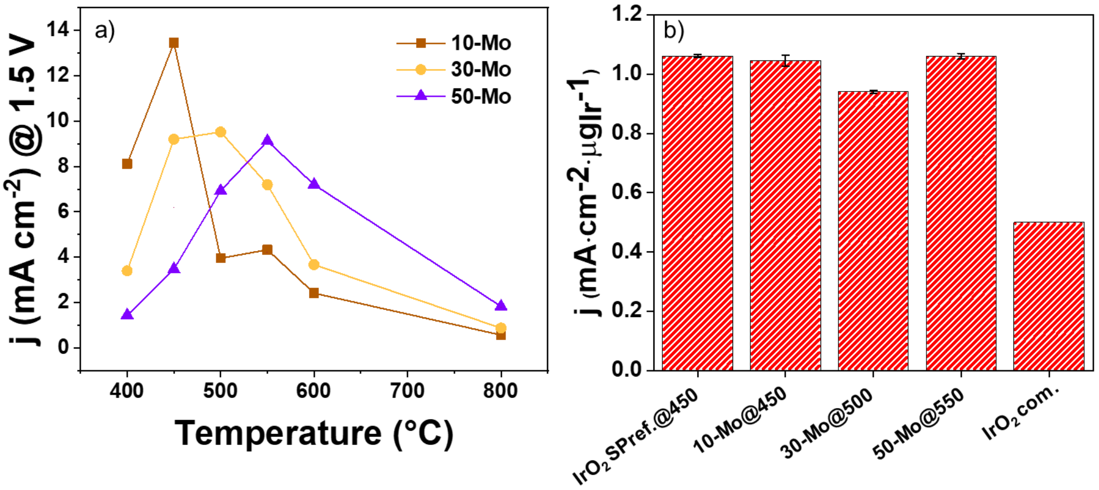

Figure 3.14 a) Evolution of the current densities values recorded at 1.5 V for samples prepared with 10, 30 and 50% Mo as a function of temperature of calcination and b) Mass activity at the optimal calcination temperature at 1.5 V.

From Figure 3.14a, we can observe that as the sample reached the optimal calcination temperature the activity of the various materials decreased with increasing Mo content. However, the activity reported to the actual mass of iridium remains almost constant, and even higher than commercial IrO_2 by almost the double as depicted in Figure 3.14b. This can be explained by the fact that molybdenum does not affect the intrinsic activity that iridium exhibits by itself, but it rather modifies the crystallization temperature at which iridium oxide is the most active. Now, as observed in Figure 3.15a when comparing all the samples at which they performed best, it is possible to deduct that lower temperature treatment enhance the oxygen evolution reaction activity as discussed above. Taking 10 mA cm^{-2} as reference, based on section 3.1, samples showed an overpotential between 260 – 273 mV, a significant improvement of 40 to 30 mV as compared to commercial IrO_2 which overpotential is η_{10} = 300 mV. Notably, those materials compare very favorably with values reported in the literature, such as pure IrO_2 (η_{10} = 280 mV) by spray-drying technique,[30] Ir-Ru alloys (η_{10} = 294 - 338 mV),[34] or related materials reported by *Tariq et al.,*[35] with molybdenum contents of 70% (η_{10} = 270 mV).

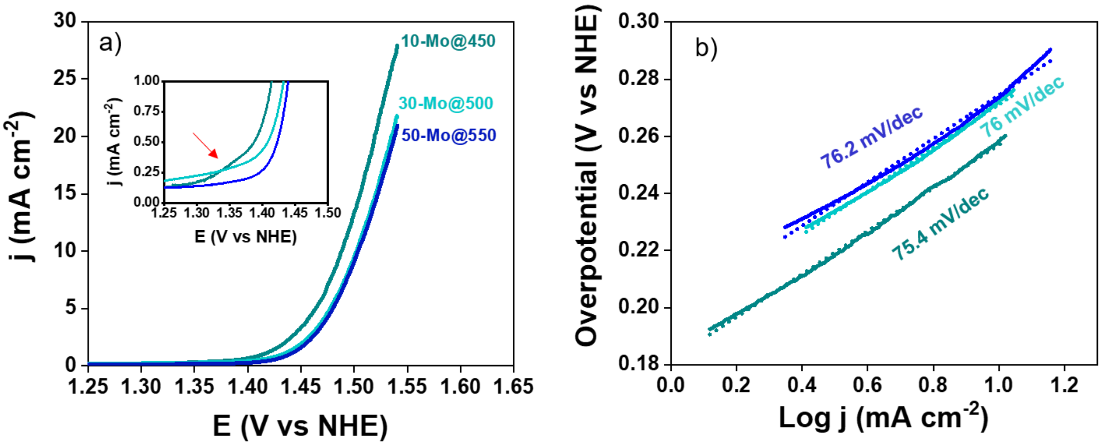

Figure 3.15 a) $Ir_{1-x}Mo_xO_2$ as a function of Mo content at the best OER performance (inset catalytic wave) and b) Tafel slopes of $Ir_{1-x}Mo_xO_2$ at the best OER performance.

In addition, as mention in section 3.2.2, a Tafel plot can be obtained from polarization curves as in Figure 3.15b which presents the Tafel slopes extracted from Figure 3.15a. From Figure 3.15b, the Tafel slopes are in the range of 75 to 76 mV dec^{-1}, these values are slightly higher than the ones reported for pure iridium oxide synthesized by anodic oxidation of metallic iridium (40 mV dec^{-1}),[36] and iridium based alloys nanowires (56 to 70 mV dec^{-1}).[37] On the other hand, the Tafel slopes from the Ir-Mo mixed oxides are congruent with spray-drying pure iridium oxides (70 to 117 mV dec^{-1}),[30] and iridium based multimetallic alloys (71 to 75 mV dec^{-1}).[26] However, knowing complexity of the 4-electrons transfer for water oxidation, and despite of the Tafel slope being considered as an important kinetic parameter to evaluate the OER activity, it is visible that its value is strongly influenced by the synthesis of the catalyst, ink formulation and electrolyte where the sample is assess. Therefore, other tests are necessary to further understand the electrochemical behavior of the mixed oxides and the underlying mechanism for OER.

On the other hand, interestingly, 10-Mo@450 is the only one that showed a catalytic wave at ~ 1.35 V (inset Figure 3.15a) as for pure IrO_2 [30] by spray-drying. Also, *Ahmed et al.,*[38] observed at 1.4 V this peak in IrO_2 NRs and they attribute this to the transformation of Ir^{3+} to Ir^{4+} since previously *Lee et al.,*[39] and *Smith et al.,*[40] presented it as well despite the electrolyte solution. This wave can be associated to changes at the surface of the catalyst under the electrocatalytic conditions, and thus, XPS and XAS (in situ techniques) become useful to understand and establish structure, activity, and stability relationships. XPS technique is used to probe surface oxidation states while XANES follows the evolution of oxidation state in the bulk of the sample. In chapter 2, it was stated that both techniques demonstrated that the same oxidation state is present in the surface as in the bulk. However, is necessary to correlate those results with OER activity. All three samples at the different calcination temperatures were measured by both techniques.

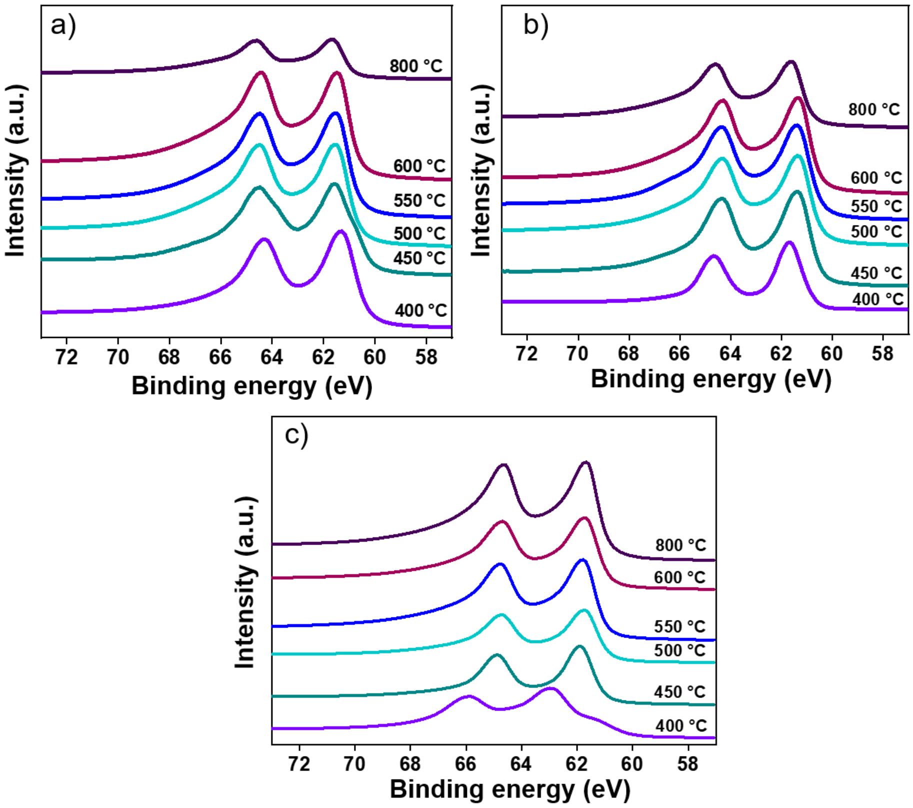

Figure 3.16 XPS spectra in the Ir 4f region of samples prepared with (a) 10-Mo, (b) 30-Mo and (b) 50-Mo calcined from 400 to 800°C.

The Ir-Mo XPS spectra was divided into three regions: Ir-4f, O 1s, and Mo-3d. Firstly, in the 4f region (characteristic of rutile type structure) depicted in Figure 3.16, main peaks located between 62.3 and 65.3 eV for Ir-4f$_{7/2}$ and Ir-4f$_{5/2}$, respectively, can be attributed to the presence of Ir^{3+} for all samples calcined at 400 °C.[41] At this temperature 10, 30 and 50-Mo samples are considered to be amorphous, therefore, the presence of Ir^{3+} is probably a result of surface hydroxide species, which have been shown to be present in amorphous IrO_x as reported previously by *Pfeifer et al.*[42] and *Smith et al.*[40] assigning this to the synthesis process. On the other hand, as the temperature of calcination increased, a shift (Figure 3.16) is detected and the peaks are located now at 61.7 and 64.7 eV for Ir-$4f_{7/2}$ and Ir-$4f_{5/2}$, respectively. These positions have been reported for pure IrO_2 materials sintered by different routes calcined in the range 450 – 800 °C [35, 41, 43, 44] as well as commercial IrO_2,[45] Moreover, other studies of mixed oxides, such as $Cu_{0.3}Ir_{0.7}O_{\delta}$,[44] $Ir_{0.3}Mo_{0.7}O_{\delta}$,[35] $Ru_xIr_{1-x}O_2$,[46] and others,[47] have attributed this shift to the change of Ir^{3+} to Ir^{4+} or mainly the presence of species of Ir^{4+}.[48] In the case of this study, 10, 30 and 50-Mo samples, the only iridium species present is Ir^{4+} when the samples are calcined at ≥500 °C.

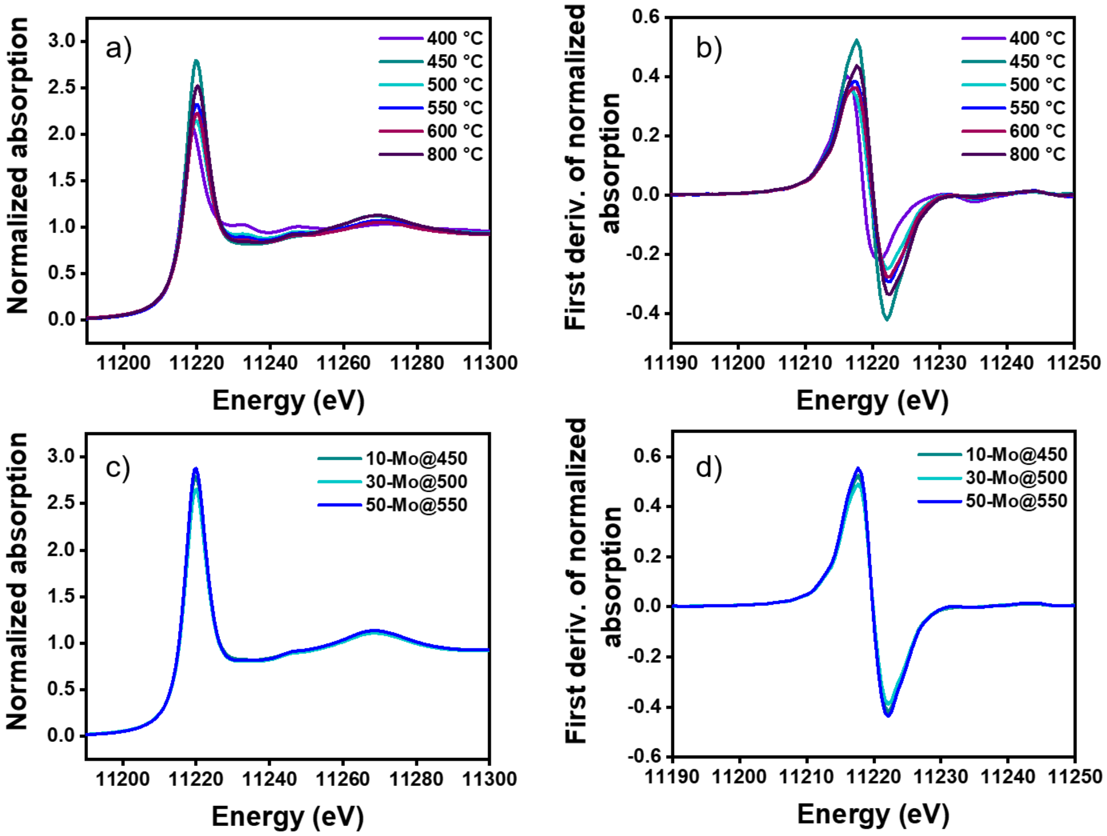

Figure 3.17 XANES spectra at Ir L_{III} edge and the corresponding first derivative of samples prepared with (a,b) 10- Mo calcined from 400 to 800°C, and (c,d) best OER samples.

In addition, when analyzing the O 1s region at the samples calcined at 400 °C and 450 °C (where the transition from $Ir^{3+} \rightarrow Ir^{4+}$ takes place), the change in the peak intensities located at 531 eV (M-OH bonds) and 530 eV (M-O bonds) might be influenced by the transition of Ir oxidation state. These binding energies are in good agreement with the literature for pure IrO_2 materials, but they have also been associated with the presence of O^{I-} and O^{II-} electrophilic species in mixed oxides where these species by electrophilic attack improve the electrochemical nature of the samples.[35, 42, 49, 50] However, as the calcination temperature is increased the ratio of intensity of those two peaks does not change significantly. Therefore, they cannot be related to the OER performance of Ir-Mo oxides. Lastly, from XPS measurements, in the Mo-3d region, the two peaks located at 232.5 and 235.7 eV which are attributed to $3d_{5/2}$ and $3d_{3/2}$, respectively, are characteristic of binding energies of Mo^{6+} when samples are calcined at low temperatures,[35, 51] in our case 400 °C. Upon heating, the two peaks move to slightly lower values, more precisely 231.5 eV ($3d_{5/2}$) and 234.7 eV ($3d_{3/2}$), and these values are associated with Mo^{5+}, as previously reported by *Vasilopoulou et al.,*[52] for molybdenum oxides. Thus, this shift suggests a reduction in oxidation state and is attributed to the change of Mo^{6+} to Mo^{5+} when passing from 400 to 500 °C up to 600 °C while at 800 °C a very small peak corresponding to 230 eV for $3d_{5/2}$ is associated with Mo^{4+} along with a higher contribution of Mo^{5+} peaks.[52]

As complementary, XAS measurements (Figure 3.17) were considered to observe the behavior in the bulk. In this case, despite molybdenum content, the Ir-L_{III} revealed that the transition from $Ir^{3+} \rightarrow Ir^{4+}$ occurs between 450 and 500 °C, instead of 400 and 450 °C in XPS. Thus, iridium oxidation at the surface and in the bulk occurs almost simultaneously at the same temperature with a slight delay in XANES. Now, based on the above and incorporating the results with OER in Figure 3.13 the predominant oxidation state of iridium is Ir^{4+}, whereas the most active electrocatalysts from the 30 and 50-Mo series are those calcined at 500 °C and 550 °C, respectively. On the other hand, when observing Figure 3.15a, 10-Mo@450 exhibits a better performance towards OER, however, this shows that mixture of Ir^{3+}/Ir^{4+} or just the presence of Ir^{3+} species at the material surface does not affect the activity of the electrocatalysts.

Following the results introduced in chapter 2 with the ones obtained in this chapter, curiously, the best OER performance of the Ir-Mo oxides does not correspond directly to the lower calcination temperature. It rather moves towards higher temperatures as the Mo content in the material increases, similar to the behavior observed by XRD in chapter 2. Thus, to better understand this behavior it is necessary to relate the results found on chapter 2 regarding the morphology and the XRD data with the optimal calcination temperatures.

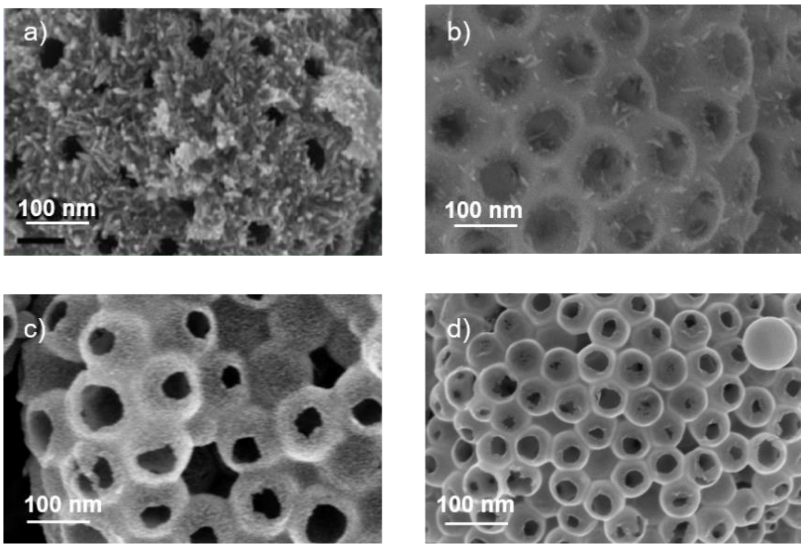

Figure 3.18 Comparison of SEM micrographs at the optimal calcination temperature between a) IrO_2@450 (taken from[30]), b) 10-Mo@450, c) 30-Mo@500 and d) 50-Mo@550.

Firstly, the morphology observed on the SEM images (Figure 3.18) from 10 to 50-Mo, showed that the materials are very similar to pure IrO_2 porous microspheres at the same low temperatures in terms of porosity, especially 10-Mo@450 since it shows the needle-like particle. Based on this comparison, is possible to associate the porosity of Ir-Mo oxides to the enhanced OER activity presented in this work. Similarly, *Faustini et al.,*[30] have reported the influenced of the porogen to OER activity in which as the temperature increased the porogen size was lost, as observed in Ir-Mo oxides in Figure 3.19, leading to a decrease in OER activity.

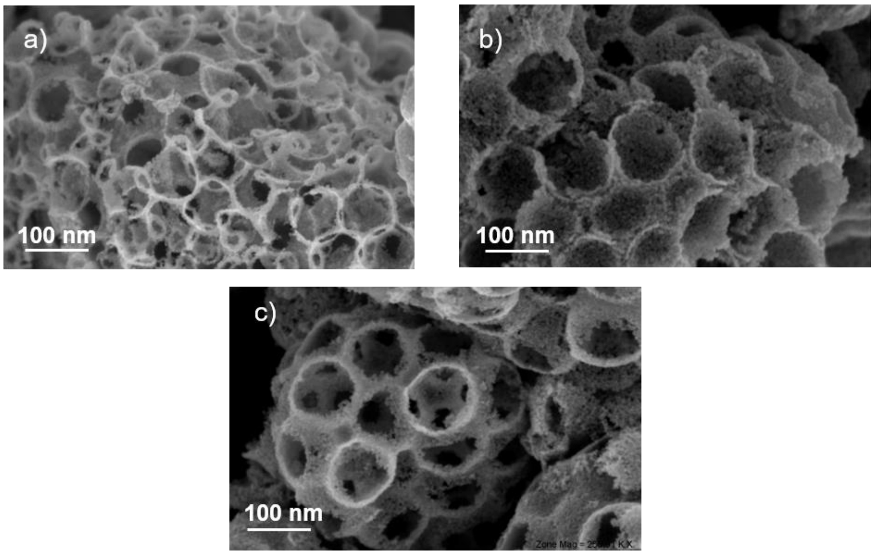

Figure 3.19 SEM micrographs calcined at 800 °C between a)10-Mo, b) 30-Mo and c) 50-Mo.

Now, when observing the OER results in Figure 3.13, it is clear that the electrochemical activity of the oxide during OER is strongly dependent on the calcination temperature, which may be due to an effect of the oxide structure, amorphous or crystalline.[40] At high calcination temperatures, sintering effects begin to occur resulting in fully crystalline material (well-defined peaks in XRD). Meanwhile, at lower temperatures or when characteristic peaks appear in XRD pattern, the results are either not fully or full amorphous materials. Thus, as complementary, XRD results were considered.

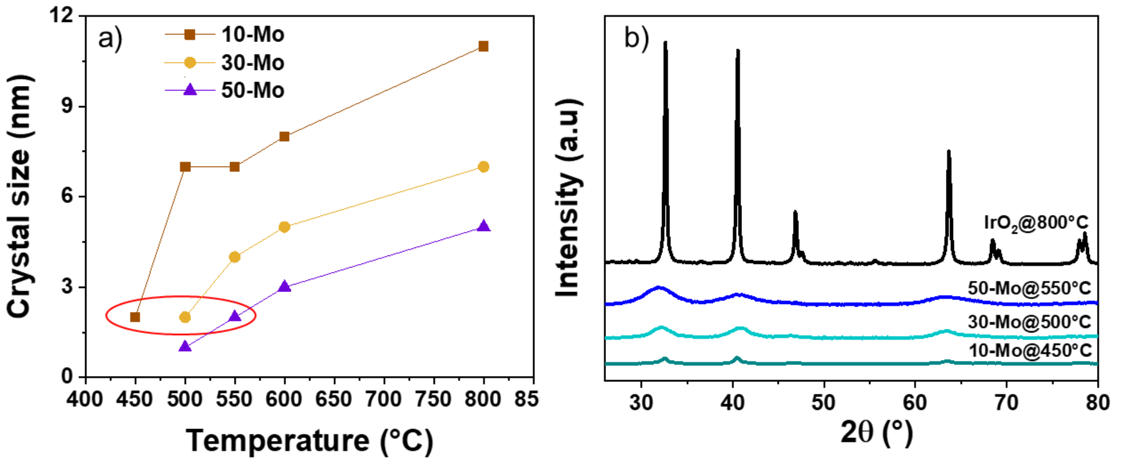

Figure 3.20 a) Evolution of the crystallite size of $Ir_{1-x}Mo_xO_2$ (x = 0.1, 0.3 and 0.5) phase as a function of temperature and b) Comparison between the XRD patterns at which the samples exhibited a good activity towards OER.

As observed in Figure 3.20a, when looking at the temperature at which each composition is more active (red circle), interestingly, small crystallite size of 2 nm is present in all. Also, a common feature when comparing the XRD patterns (Figure 3.20b) at the optimal calcination temperature, all present broader peaks (key characteristic to present small crystallite size) in contrast to the narrow peaks of pure IrO_2. Moreover, the crystallite size of the Ir-Mo oxides is in agreement with *Abbott et al.,*[41] where very active iridium oxide synthesized at 350 °C by modified Adams fusion method, small crystallite size was present (1.7 ± 0.4 nm) as well. Similar values and good activity, despite the different route of synthesis, reported small particle size such as $Ir_xRu_yTa_zO_2$,[53] mesoporous IrO_x films,[54] among others.[39, 55, 56]

In addition, it is noticeable that in samples such as 30-Mo and 50-Mo, calcined both at 400 °C, crystallite size is not present due to the fact that Rietveld refinement was not possible since at these temperatures those samples are fully amorphous. The full amorphization of those samples and the uncomplete formation of the mixed oxide at this temperature explains the poor performance towards OER in Figure 3.13b (30-Mo) and Figure 3.13c (50-Mo). On the other hand, the crystallite size increased in all samples when calcined at 800 °C, confirming that the crystallinity of the samples (also visible in SEM micrographs Figure 3.19) probably influences the catalytic activity resulting in a poor performance towards OER. In the literature, various reports indicated that alloys (i.e., Ni Fe),[57] oxides (i.e., RuO_2)[58] and perovskites (i.e., $CaCu_3Fe_4O_{12}$)[59] have shown the amorphous versus crystallinity material performance towards OER, concluding that the amorphous forms of those materials outstand in performance their crystalline forms. A particular example for iridium is the one presented by *Smith et al.,*[40] when comparing amorphous IrO_x films with its crystalline form, showing that the amorphous films exhibited a better OER by decreasing the overpotential by 100 mV. In addition, SEM morphologies confirm the structural similarities between the most active materials, regardless of the composition, and agrees as well with how the activity of pure IrO_2 works.[30]

3.4.2.2. *Stability test*

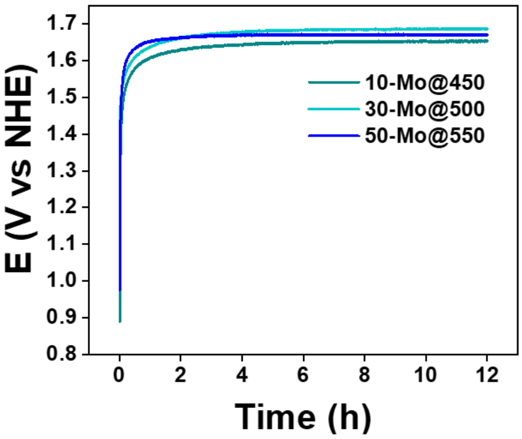

Figure 3.21 Chronopotentiometry measurements at 1 mA for 12 hours.

As complementary, chronopotentiometry measurements (Figure 3.21) for 12 hours were performed to 10, 30 and 50-Mo calcined at 450, 500, and 550°C, respectively, and the current was set at 1 mA (i.e., 5 mA cm^{-2}). A couple of hours were generally necessary to reach a constant potential between 1.6 – 1.7 V over the course of a 12 h test. This suggests that the porous $Ir_{1-x}Mo_xO_2$ phases possess a good stability while the OER process is taking place.

In addition, even though there is a little difference between the potentials, it can be said that 10-Mo@450 needed a lower potential to maintain the current. This is due to the fact that the calcination temperature influences the stability of the oxide during OER. This behavior has been reported previously by various authors, for instance *Cherevko et al*.,[33] showed that for IrO_x/Ti films calcined at 250 and 350 °C maintained the given current density (1 mA cm^{-2} followed by 2 mA cm^{-2}) at lower potential, around 1.4 V vs RHE, in contrast to the 1.6 V that samples 450 and 550 °C exhibited. On the other hand, when comparing Ir-Mo oxides to MoO_3 stability, *Zhang et al.,*[60] reported a chronoamperometry where porous MoO_3 showed a good stability for 24 h at 1.68 V vs RHE while maintaining a current density at 4 mA cm^{-2}, similarly to results in Figure 3.21. Also, Ir-Mo oxides stability behavior agrees with other iridium base materials such as IrNi or IrNiCu [26] with voltages around 1.5 – 1.7 V at a constant current density of 10 mA cm^{-2}, and NiIrRuAl with similar values at 5 mA cm^{-2}.[61]

Differently, chronocoulometry is another way of presenting chronoamperometry measurements, where the charge is plotted as a function of time.[27] Recently, *Wu et al.,*[62] have used of this technique on $Ru_xSn_{1-x}O_2$ to compare the passage of electric charge among the different catalysts. Moreover, tests on PEM water electrolysis cells under galvanostatic conditions (usually at 80 °C) where the cell voltage versus current density is plotted, is commonly reported in the literature.[63] For instance, *Faustini et al.,*[30] presented the polarization curves of pure IrO_2 and $Ir_{0.7}Ru_{0.3}O_x$, showing the agreement with ex-situ electrochemical studies. However, testing materials stability in an electrolyzer, despite of being tested under real dynamic conditions, the results can be misleading and not reflect the actual performance of the electrocatalyst since several factors affect the measurements such as leaking, gas bubbles, not correct placement of the electrocatalyst coating onto the MEA, the need of higher amount of electrocatalyst to carry the stability test, not well stacking of the components, among others.[64, 65] Thus, measurements by the three-electrode set up are useful, since lower quantities and less factors that can interfere in the measurements can be controlled.

Furthermore, other ways for investigating the stability aspect of electrocatalysts involve the quantification by degradation/dissolution of products, this receives the name of accelerated durability tests (ADT), and a new independent metric called stability number (SN).[66, 67] *Delgado et al.,*[68] and *Lee et al.,*[69] have made use of ATDs consisting on several dynamic conditions i.e., cycling of the electrode in the electroactive region, while *Geiger et al.,*[66] presented the amount of dissolved metal in relation to the evolved oxygen as SN aiming at estimating the lifetime of the investigated materials i.e., perovskites, amorphous IrO_x and others. However, further research in understanding dissolution and degradation processes is essential since assessing stability for the OER, has serious limitations that have arisen when comparing the performance in electrochemical cells to PEMWE assemblies, specifically the membrane electrode assemblies (MEAs).[70]

3.5. Conclusion

In this chapter, the series of $Ir_{1-x}Mo_xO_2$ oxides across the composition range x = 0, 0.1, 0.3, 0.5, 0.7 and 1 have been tested by a typical three-electrode electrochemical setup. The electrochemical study showed that the OER activity decreases dramatically when the sintering temperature is increased, due to crystallinity and loss in porosity when observing SEM images at higher temperatures. Samples heated between 450 – 550 °C presented the best performances as compared to commercial IrO_2, and the intrinsic activity is similar among the different series since it depends strongly on the material structure (i.e., the crystallite size). Therefore, not fully amorphous materials are the most active. Furthermore, XPS and XANES measurements showed that when observing the oxidation state of iridium at these temperatures (450 – 550°C) the three main compositions evidenced Ir^{4+} or the transition from Ir^{3+} to Ir^{4+}. Therefore, it can be postulated that the oxidation state is not the one ruling over OER performances. Finally, $Ir_{0.9}Mo_{0.1}O_2$, $Ir_{0.7}Mo_{0.3}O_2$ and $Ir_{0.5}Mo_{0.5}O_2$ compositions were selected to be further studied in view of the stability, where the three compounds maintained a constant potential over the course of several hours, suggesting that these oxide series possess a good stability during the oxygen evolution reaction process.

3.6. References

1. Maric, R.; Yu, H., Proton Exchange Membrane Water Electrolysis as a Promising Technology for Hydrogen Production and Energy Storage. 2019.
2. Borup, R., et al., Scientific Aspects of Polymer Electrolyte Fuel Cell Durability and Degradation. *Chem. Rev.*, 2007, *107* (10), 3904-3951.
3. Sillanpää, M.; Shestakova, M., Introduction. In *Electrochemical Water Treatment Methods*, 2017; pp 1-46.
4. Guerrini, E.; Trasatti, S., Electrocatalysis in Water Electrolysis. 2009; pp 235-269.
5. Trasatti, S., Electrochemical Theory | Oxygen Evolution. 2009; pp 49-55.
6. Peng, L.; Wei, Z., Catalyst Engineering for Electrochemical Energy Conversion from Water to Water: Water Electrolysis and the Hydrogen Fuel Cell. *Engineering*, 2020, *6* (6), 653-679.
7. Bladergroen, B., et al., Overview of Membrane Electrode Assembly Preparation Methods for Solid Polymer Electrolyte Electrolyzer. In *Electrolysis*, 2012.
8. McCrory, C. C., et al., Benchmarking heterogeneous electrocatalysts for the oxygen evolution reaction. *J. Am. Chem. Soc.*, 2013, *135* (45), 16977-87.
9. Feng, Q., et al., A review of proton exchange membrane water electrolysis on degradation mechanisms and mitigation strategies. *J. Power Sources*, 2017, *366*, 33-55.
10. Kroschel, M., et al., Analysis of oxygen evolving catalyst coated membranes with different current collectors using a new modified rotating disk electrode technique. *Electrochim. Acta*, 2019, *317*, 722-736.
11. Millet, P., Characterization Tools for Polymer Electrolyte Membrane (PEM) Water Electrolyzers: Principles and Applications. 2015; pp 179-217.
12. Du, C., et al., Rotating Disk Electrode Method. In *Rotating Electrode Methods and Oxygen Reduction Electrocatalysts*, 2014; pp 171-198.

13. Kuznetsova, E., et al., Identification of the byproducts of the oxygen evolution reaction on Rutile-type oxides under dynamic conditions. *J. Electroanal. Chem.*, 2014, *728*, 102-111.
14. Guy Denuault, M. S., Kristy-Jo Williams, Classical experiments. In *Handbook of Electrochemistry*, Zoski, C. G., Ed. Elsevier: 2007; pp 431 - 469.
15. Orfanidi, A., et al., Ink solvent dependence of the ionomer distribution in the catalyst layer of a PEMFC. *J. Electrochem. Soc.*, 2018, *165* (14), F1254-F1263.
16. Shukla, S., et al., Experimental and theoretical analysis of the ink dispersion stability for polymer electrolyte fuel cell applications. *J. Electrochem. Soc.*, 2017, *164* (6), F600-F609.
17. Filimonenkov, I. S., et al., Rotating ring-disk electrode as a quantitative tool for the investigation of the oxygen evolution reaction. *Electrochim. Acta*, 2018, *286*, 304-312.
18. Bontempelli, G.; Toniolo, R., Measurement methods | Electrochemical: Linear sweep and cyclic voltammetry. *Encyclopedia of Electrochemical Power Sources*, 2009, 643-654.
19. Li, S.; Thomas, A., Emerged carbon nanomaterials from metal-organic precursors for electrochemical catalysis in energy conversion. In *Advanced Nanomaterials for Electrochemical-Based Energy Conversion and Storage*, 2020; pp 393-423.
20. Zhang, J., et al., Techniques for PEM Fuel Cell Testing and Diagnosis. In *PEM Fuel Cell Testing and Diagnosis*, 2013; pp 81-119.
21. Martos-Maldonado, M. C., et al., Electrochemical detection of glutathione S-transferase: an important enzyme in the cell protective mechanism against oxidative stress. *Methods Mol Biol*, 2015, *1208*, 123-38.
22. Pham, H. H., et al., Nanosized $Ir_xRu_{1-x}O_2$ electrocatalysts for oxygen evolution reaction in proton exchange membrane water electrolyzer. *Advances in Natural Sciences: Nanoscience and Nanotechnology*, 2015, *6* (2), 025015.
23. Bontempelli, G., et al., Polarography/Voltammetry. In *Reference Module in Chemistry, Molecular Sciences and Chemical Engineering*, 2018.
24. Dickinson, E. J. F.; Wain, A. J., The Butler-Volmer equation in electrochemical theory: Origins, value, and practical application. *J. Electroanal. Chem.*, 2020, *872*.
25. Fang, Y.-H.; Liu, Z.-P., Tafel Kinetics of Electrocatalytic Reactions: From Experiment to First-Principles. *ACS Catal.*, 2014, *4* (12), 4364-4376.
26. Zhang, J., et al., Hierarchical iridium-based multimetallic alloy with double-core-shell architecture for efficient overall water splitting. *Sci. China Mater.*, 2019, *63* (2), 249-257.
27. Inzelt, G., Chronoamperometry, Chronocoulometry, and Chronopotentiometry. In *Encyclopedia of Applied Electrochemistry*, Kreysa, G.; Ota, K.-i.; Savinell, R. F., Eds. Springer New York: New York, NY, 2014; pp 207-214.
28. Napporn, T. W., et al., Electrochemical Measurement Methods and Characterization on the Cell Level. In *Fuel Cells and Hydrogen*, 2018; pp 175-214.
29. Garsany, Y., et al., Impact of film drying procedures on RDE characterization of Pt/VC electrocatalysts. *J. Electroanal. Chem.*, 2011, *662* (2), 396-406.
30. Faustini, M., et al., Hierarchically Structured Ultraporous Iridium-Based Materials: A Novel Catalyst Architecture for Proton Exchange Membrane Water Electrolyzers. *Adv. Energy Mater.*, 2019, *9* (4), 1802136.
31. Garsany, Y., Experimental methods for quantifying the activity of platinum electrocatalysts for the oxygen reduction reaction. *Anal. Chem.*, 2010, *82* (15), 6321-6328.
32. Gou, W., et al., Iridium-Chromium Oxide Nanowires as Highly Performed OER Catalysts in Acidic Media. *ChemCatChem*, 2019, *11* (24), 6008-6014.
33. Cherevko, S., et al., Stability of nanostructured iridium oxide electrocatalysts during oxygen evolution reaction in acidic environment. *Electrochem. Commun.*, 2014, *48*, 81-85.
34. Lee, S. W., et al., Multifunctional Ir–Ru alloy catalysts for reversal-tolerant anodes of polymer electrolyte membrane fuel cells. *J. Mater Sci Technol*, 2021, *60*, 105-112.

35. Tariq, M., et al., Unraveling the Beneficial Electrochemistry of IrO_2/MoO_3 Hybrid as a Highly Stable and Efficient Oxygen Evolution Reaction Catalyst. *ACS Sustain. Chem. Eng.*, 2018, *6* (4), 4854-4862.
36. Ouattara, L., et al., Electrochemical comparison of IrO_2 prepared by anodic oxidation of pure iridium and IrO_2 prepared by thermal decomposition of H_2IrCl_6 precursor solution. *J. Appl. Electrochem.*, 2009, *39* (8), 1361-1367.
37. Wang, Y., et al., Nanoporous Iridium-Based Alloy Nanowires as Highly Efficient Electrocatalysts Toward Acidic Oxygen Evolution Reaction. *ACS Appl Mater Interfaces*, 2019, *11* (43), 39728-39736.
38. Ahmed, J.; Mao, Y., Ultrafine Iridium Oxide Nanorods Synthesized by Molten Salt Method toward Electrocatalytic Oxygen and Hydrogen Evolution Reactions. *Electrochim. Acta*, 2016, *212*, 686-693.
39. Lee, Y., et al., Synthesis and Activities of Rutile IrO_2 and RuO_2 Nanoparticles for Oxygen Evolution in Acid and Alkaline Solutions. *J Phys Chem Lett*, 2012, *3* (3), 399-404.
40. Smith, R. D. L., et al., Facile Photochemical Preparation of Amorphous Iridium Oxide Films for Water Oxidation Catalysis. *Chem. Mater.*, 2014, *26* (4), 1654-1659.
41. Abbott, D. F., et al., Iridium Oxide for the Oxygen Evolution Reaction: Correlation between Particle Size, Morphology, and the Surface Hydroxo Layer from Operando XAS. *Chem. Mater.*, 2016, *28* (18), 6591-6604.
42. Pfeifer, V., et al., Reactive oxygen species in iridium-based OER catalysts. *Chem Sci*, 2016, *7* (11), 6791-6795.
43. Sanchez Casalongue, H. G., et al., In situ observation of surface species on iridium oxide nanoparticles during the oxygen evolution reaction. *Angew. Chem. Int. Ed. Engl.*, 2014, *53* (28), 7169-72.
44. Sun, W., et al., An efficiently tuned d-orbital occupation of IrO_2 by doping with Cu for enhancing the oxygen evolution reaction activity. *Chem Sci*, 2015, *6* (8), 4993-4999.
45. Bozack, M. J., Sputter-Induced Modifications of IrO_2 During XPS Measurements. *Surf. Sci. Spectra*, 1993, *2* (2), 123-127.
46. Audichon, T., et al., Preparation and characterization of supported $Ru_xIr_{(1-x)}O_2$ nano-oxides using a modified polyol synthesis assisted by microwave activation for energy storage applications. *Appl. Catal. B*, 2017, *200*, 493-502.
47. Zaman, W. Q., et al., Ni–Co Codoping Breaks the Limitation of Single-Metal-Doped IrO_2 with Higher Oxygen Evolution Reaction Performance and Less Iridium. *ACS Energy Lett.*, 2017, *2* (12), 2786-2793.
48. Pfeifer, V., et al., The electronic structure of iridium oxide electrodes active in water splitting. *Phys. Chem. Chem. Phys.*, 2016, *18* (4), 2292-6.
49. Pfeifer, V., et al., In situ observation of reactive oxygen species forming on oxygen-evolving iridium surfaces. *Chem Sci*, 2017, *8* (3), 2143-2149.
50. Massue, C., et al., Reactive Electrophilic $O^{(I-)}$ Species Evidenced in High-Performance Iridium Oxohydroxide Water Oxidation Electrocatalysts. *ChemSusChem*, 2017, *10* (23), 4786-4798.
51. Zheng, L., et al., Polyaniline-intercalated molybdenum oxide nanocomposites: simultaneous synthesis and their enhanced application for supercapacitor. *Chem Asian J*, 2011, *6* (6), 1505-14.
52. Vasilopoulou, M., et al., The influence of hydrogenation and oxygen vacancies on molybdenum oxides work function and gap states for application in organic optoelectronics. *J. Am. Chem. Soc.*, 2012, *134* (39), 16178-87.
53. Marshall, A., et al., Performance of a PEM water electrolysis cell using $Ir_xRu_yTa_zO_2$ electrocatalysts for the oxygen evolution electrode. *Int. J. Hydrogen Energy*, 2007, *32* (13), 2320-2324.
54. Nakagawa, T., et al., Efficient Electro-Oxidation of Water near Its Reversible Potential by a Mesoporous IrO_x Nanoparticle Film. *J. Phys. Chem. C*, 2009, *113* (30), 12958-12961.

55. Zhao, Y., et al., A High Yield Synthesis of Ligand-Free Iridium Oxide Nanoparticles with High Electrocatalytic Activity. *J. Phys. Chem. Lett*, 2011, *2* (5), 402-406.
56. Rasten, E., et al., Electrocatalysis in water electrolysis with solid polymer electrolyte. *Electrochim. Acta*, 2003, *48* (25-26), 3945-3952.
57. Cai, W., et al., Amorphous versus Crystalline in Water Oxidation Catalysis: A Case Study of NiFe Alloy. *Nano Lett.*, 2020, *20* (6), 4278-4285.
58. Tsuji, E., et al., Electrocatalytic activity of amorphous RuO_2 electrode for oxygen evolution in an aqueous solution. *Electrochim. Acta*, 2011, *56* (5), 2009-2016.
59. Yagi, S., et al., Effects of Size and Crystallinity of $CaCu_3Fe_4O_{12}$ on Catalytic Activity for Oxygen Evolution Reaction. *Materials Transactions*, 2020, *61* (8), 1698-1702.
60. Zhang, M., et al., Porous molybdenum trioxide as a bifunctional electrocatalyst for oxygen and hydrogen evolution. *J. Electroanal. Chem.*, 2019, *836*, 102-106.
61. Liu, N., et al., Hierarchically porous nickel–iridium–ruthenium–aluminum alloys with tunable compositions and electrocatalytic activities towards the oxygen/hydrogen evolution reaction in acid electrolyte. *J. Mater. Chem. A*, 2020, *8* (13), 6245-6255.
62. Xu Wu, et al., Nano-crystalline $Ru_xSn_{1-x}O_2$ powder catalysts for oxygen evolution reaction in proton exchange membrane water electrolysers. *Int. J. Hydrogen Energy*, 2011, *36*, 14796-14804.
63. A. Marshall, et al., Preparation and characterisation of nanocrystalline $Ir_xSn_{1-x}O_2$ electrocatalytic powders. *Mater. Chem. Phys.*, 2005, *94*, 226-232.
64. Papakonstantinou, G., et al., Degradation study of a proton exchange membrane water electrolyzer under dynamic operation conditions. *Applied Energy*, 2020, *280*.
65. Millet, P., et al., Electrochemical performances of PEM water electrolysis cells and perspectives. *Int. J. Hydrogen Energy*, 2011, *36* (6), 4134-4142.
66. Geiger, S., et al., The stability number as a metric for electrocatalyst stability benchmarking. *Nat. Catal.*, 2018, *1* (7), 508-515.
67. Pizzutilo, E., et al., On the Need of Improved Accelerated Degradation Protocols (ADPs): Examination of Platinum Dissolution and Carbon Corrosion in Half-Cell Tests. *J. Electrochem. Soc.*, 2016, *163* (14), F1510-F1514.
68. Delgado, D., et al., Accelerated Durability Test for High-Surface-Area Oxyhydroxide Nickel Supported on Raney Nickel as Catalyst for the Alkaline Oxygen Evolution Reaction. *Chemphyschem*, 2019, *20* (22), 3147-3153.
69. Lee, S. W., et al., Ordered mesoporous ruthenium oxide with balanced catalytic activity and stability toward oxygen evolution reaction. *Catal. Today*, 2020, *358*, 203-209.
70. Knoppel, J., et al., On the limitations in assessing stability of oxygen evolution catalysts using aqueous model electrochemical cells. *Nat Commun*, 2021, *12* (1), 2231.

CHAPTER 4. DETERMINING ELECTROCHEMICAL SURFACE AREA ON $Ir_{1-x}Mo_xO_2$ OXIDES

The electrochemical study of the $Ir_{1-x}Mo_xO_2$ (x = 0, 0.1, 0.3, 0.5, 0.7 and 1) family presented in chapter 3 gave an insight into the activity of the catalyst. This allowed to pursue the investigation with an important parameter regarding the porosity of the material and the surface area of the catalyst. This chapter describes the determination of the electrochemical surface area (ECSA) of Ir-Mo oxides with molybdenum content of 10, 30 and 50%. The first part concerns the description of the electrochemical methods used for the surface area determination. In the second part, the cyclic voltammetry (CV) technique combined with underpotential deposition of mercury and double layer capacitance tests are used to evaluate the ECSA of Ir-Mo oxides in acidic solution as function of the catalyst calcination temperature and composition. We are showing that double layer capacitance analysis only reveals tendency relating the calcination temperature and surface areas, and underpotential deposition tests revealed that a value of ECSA is achievable by this technique when tested on mixed oxides. Also, some difficulties in applying this method are discussed and some solutions are suggested.

4.1 Introduction

Electrocatalysts main function is to speed up the reaction kinetics in electrolysis devices. An important feature they must possess is high electrochemical active surface area which translates as a porous material. The performance of porous electrocatalysts depends strongly on the magnitude of the surface area as it provides more active sites or more storage capacity, leading to higher current densities.[1] Therefore, the characterization and determination of surface area is essential for electrocatalyst study since it allows comparing the catalytic activity and degradation of different catalyst materials in different conditions as well as electrodes architectures (i.e., morphologies).

OER electrocatalyst with noble metal content (Ir or Ru) and their diverse forms such as alloys, oxides, and others mentioned in chapter 1, usually possess the ability to absorb species on their surfaces facilitating the reactions for energy conversion. Regarding porous catalysts in water electrolyzers, the active surface area refers to the surface area of the catalytic particles since these ones are the ones that are simultaneously in contact with the electrolyte and the current collectors.

The determination of ECSA allows to know the number of sites that are electrochemically available to carry the OER, which can differ from the actual surface area of the material. Therefore, to enhance material activity more catalytic sites are necessary. Different methods allow this quantification, and an insight on how the different methods are working is presented in the following sections.

4.1.1. Methods for the surface area determination

A series of electrochemical methods for determining the electrochemical surface area such as CO stripping, hydrogen adsorption, oxygen adsorption, underpotential deposition (UPD) of metals, voltammetry, and others are known as in-situ methods, while ex-situ methods are Brunauer–Emmett–Teller (BET) or porosimetry among others and will give information about the surface area of the material.[2-4] From these methods, BET is considered to be the one that gives a value of the real surface area and porosity, but it is not an actual measure of the number of electroactive sites. It requires a good amount of material – in the order of several hundreds of milligrams – to give reliable values which can be problematic when the route of synthesis does not produce high amounts of catalyst or if the catalyst is made of precious metals. On the other hand, low quantities of catalyst – in the order of milligrams or less – are required while running in-situ electrochemical methods. In addition, these methods allow a direct measurement of the electrochemical surface area despite of how the materials has been deposited onto the surface of the electrode.

4.1.1.4 Brunauer–Emmett–Teller (BET) theory

BET is a characterization technique for surface analysis in which the principle is the physical adsorption of gas molecules on a solid surface, from which is possible to obtain information such as surface area and pore size distribution. The technique follows the Eq. 4-1:[5]

$$\frac{P}{V(P_0-P)} = \frac{1}{V_m C} + \frac{(C-1)}{V_m C}\left(\frac{P}{P_0}\right) \qquad \textit{(Eq. 4-1)}$$

Where P_0 is the vapor pressure of the gas employed at standard conditions, P is the equilibrium pressure, V is the volume adsorbed of gas at a relative pressure given by $\left(\frac{P}{P_0}\right)$, C is a constant that depends on the temperature and is related to the enthalpies of adsorption of the mono or multilayers, and V_m is the volume of gas required to cover a monolayer (monolayer capacity).[5] From Eq. 4-1 a plot of $\frac{P}{V(P_0-P)}$ versus $\left(\frac{P}{P_0}\right)$, gives a straight line which intercept is $\frac{1}{V_m C}$ with a slope $\frac{(C-1)}{V_m C}$. The latter plot is called BET isotherm, and there are five adsorption isotherms possible as shown in Figure 4.1.[6] Type I known as the Langmuir adsorption isotherm, portrays a rapid rise as the vapor pressure increases which indicates the formation of monolayer adsorption. Type II called S-shaped isotherm presents a multiplayer adsorption (high pressures) with inflexion formation of monolayer at lower pressures while Type III exhibits rapidly a multilayer formation. Type IV is similar to type II in which both present an inflexion formation of monolayer adsorption however in this last one capillary condensation occurs or pore filling. Finally, Type V is common on flat and homogeneous adsorbents.[7]

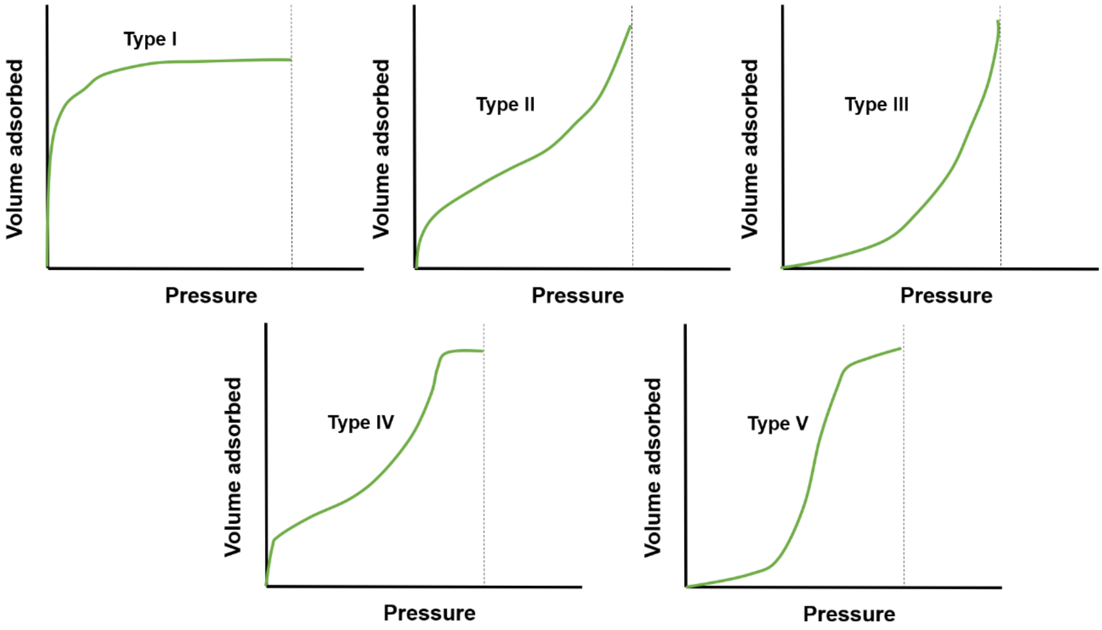

Figure 4.1 The isotherm plots the volume of gas adsorbed onto the surface of the sample as pressure increases (taken and modified from[6]).

The isotherms depend on the material and usually represent the pore size (*d*) when porous materials are subjected to this test. The three major categories are: micro- (*d* < 2nm), meso- (2< *d* <50 nm) and macroporous (*d* > 50 nm).[8] For instance, microporous materials present Type I, Type IV is generated on mesoporous materials and macroporous/non-porous exhibit Type II isotherm.[7]

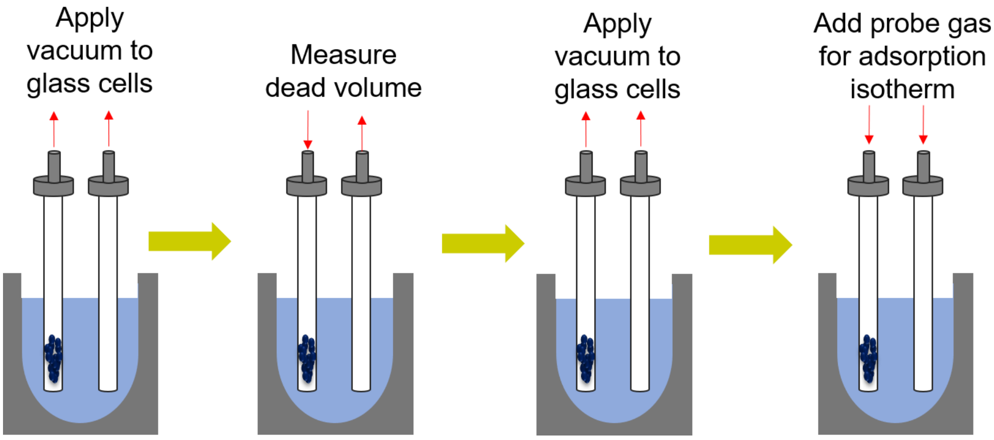

Figure 4.2 Schematic representation of measuring surface area with BET.

Thus, the area of the sample can be obtained from Eq. 4-2:

$$S = V_m \times N_{avogadro} \times A \qquad \textit{(Eq. 4-2)}$$

Where $N_{avogadro}$ is the Avogadro number per unit of volume of gas (molecules m^{-3}), and A is the area of the adsorbed gas molecule (m^2). However, values are reported based on the mass of sample used, then ECSA ($m^2\ g^{-1}$) follows:

$$ECSA = \frac{S}{mass\ sample} \qquad \textit{(Eq. 4-3)}$$

For a measurement as in Figure 4.2, the samples are placed in glass cells to be degassed in a vacuum at a temperature that will not damage the structure of the sample ‘and analyzed by the BET equipment. Firstly, usually a dead-volume measurement using an inert gas such helium is carried out to correct the gas adsorbed later. Then, once again vacuum is applied to remove the dead volume gas. Here the cells are connected to the outgas port of the device and are maintain at a constant temperature to ensure the interaction between the gas molecules and the surface of the sample, and the gas is injected with a calibrated piston. Usually, the gases used for this technique cannot chemically react with the material surfaces as the gas is adsorbed to quantify the specific surface area.[9] The probe gas most frequently used is nitrogen but argon and carbon dioxide are used as well. Therefore, BET surface area depends on the adsorbate molecule used and its adsorption cross section.[10]

4.1.1.4 Double layer capacitance (C_{dl})

The double layer capacitance is a classical approach to determine the ECSA using electrochemical techniques such as CV mentioned in chapter 3. In this case, voltammetry curves (Figure 4.3a) are recorded in small potential range, corresponding to a non-Faradaic region of the CV, and are measured at multiple scan rates. If the only process occurring in that potential range is the double layer charging, then the resulting differential capacitance equals to the C_{dl} which is the slope of the straight line (Figure 4.3b).[2, 3, 11]

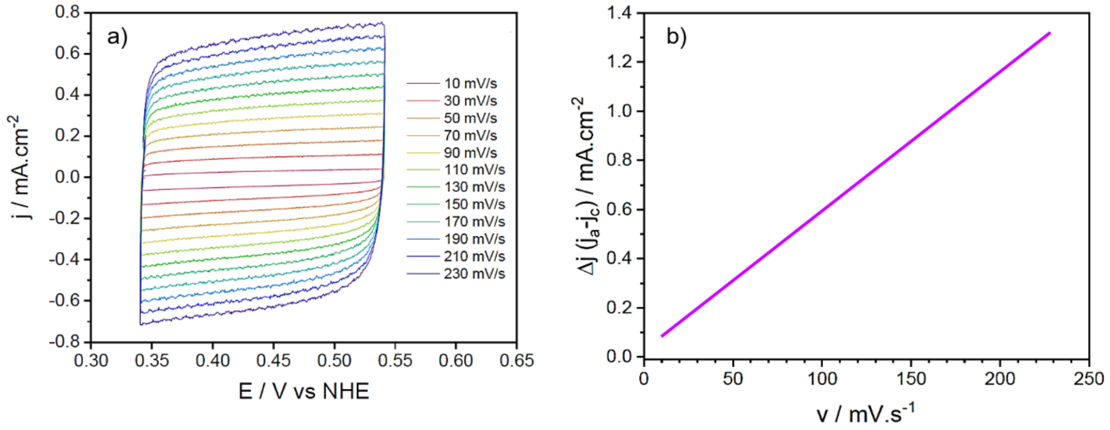

Figure 4.3 a) CV curves at different scan rates and b) the difference between anodic and cathodic measured at a specific voltage as function of the scan rate (taken and modified from[12]).

The double layer differential capacity obeys to the Eq. 4-4:[2, 3]

$$C = \frac{dQ}{dE} = i \cdot \frac{dt}{dE} = \frac{i}{dE/_{dt}} = \frac{i}{v} \qquad \textit{(Eq. 4-4)}$$

Then, the capacitance obtained is compared to a reference capacitance (C^*) value in order to obtain ECSA as follows: (C / C^*)·(1 / mass sample). The C^*, should be known and is where the limitation of this method relays since the value can varied, and various authors have reported values between 60 – 80 µF cm^{-2}

for oxide surfaces and used in materials such as perovskites,[13] SiO_2[14] or Co_3O_4.[2, 15] These values strongly depend on the electrode potential, surface structure of the material and electrolyte, thus an independent experiment has to be done to ensure a reliable $C*$ value otherwise high percentage of error could influence the ECSA.[3]

In general, this method cannot be used for comparison with different materials (i.e., oxides vs alloys) since the reference value is empiric, then it is only useful for internal comparison for a given material. For instance, porous materials or oxides tend to show a dependence of the current with the scan rate due to the less accessible surface at higher scan rate.[2] On the other hand, one of the main advantages is that this method is not destructive, enabling the use of the sample for other measurements such as OER or HER.[16]

4.1.1.3. Gas molecule adsorption methods

Using a probe gas where a gas molecule followed by electrochemical stripping is adsorbed onto the surface of the material generating an exchange current during the process is one of the in-situ methods to determine ECSA. The commonly use probe gasses are hydrogen and carbon monoxide, and they are used mainly on metals.

a) Hydrogen adsorption method

Hydrogen adsorption measurements can only be applied when the surface of the material allows “underpotential” adsorption of hydrogen molecules. Metal surfaces such as platinum, iridium, and rhodium have been studied extensively by this method. To obtain the value of ECSA, the following assumption must be taken into account: a 1:1 relation where one metal atom can absorb one hydrogen atom.[2, 17] Using CV as shown in Figure 4.4 the region where hydrogen adsorption takes place is characterized by different peaks.

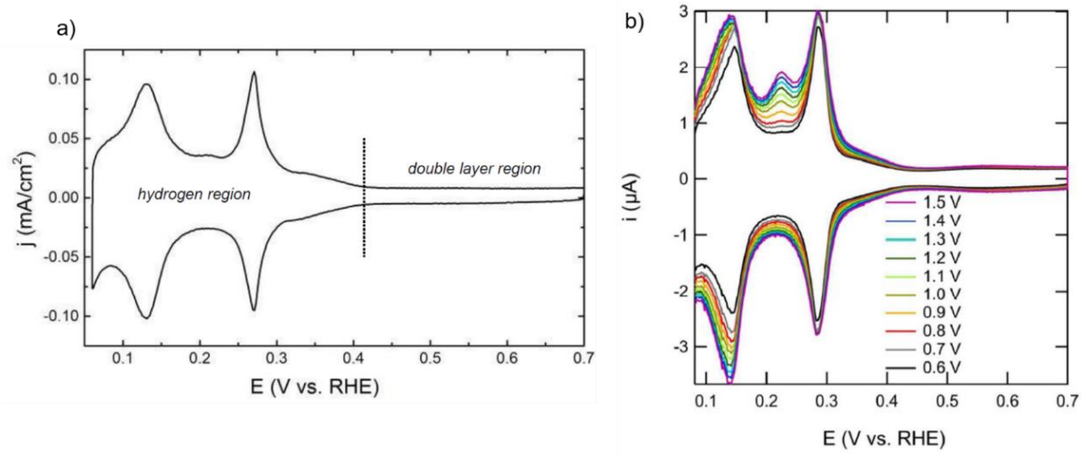

Figure 4.4 a) Blank voltammogram of a Pt polycrystalline electrode and b) Development of hydrogen adsorption peak on Pt electrode (taken and modified from[17]).

The voltammogram displayed in Figure 4.4a was recorded in 0.5 M H_2SO_4 and shows the two main regions – the third one being the "oxygen region" – identified as the "hydrogen region" where hydrogen adsorption/desorption takes place, and the "double layer region" where non-Faradaic processes are present. Figure 4.4b shows how an additional peak appearing and becoming more pronounced. For platinum, which is the example used here but as well for rhodium and iridium, the ECSA value can be calculated according to Eq. 4-5:[2, 3]

$$ECSA = \frac{Q_H}{Q_H^*} \times \frac{1}{mass\ sample} \qquad (Eq.\ 4\text{-}5)$$

Where Q_H corresponds to the charge under the voltammogram peaks for hydrogen adsorption, and the charge associated to that 1:1 ratio per unit area where a monolayer of adsorbed hydrogen is form is labeled as Q_H*. This is calculated based on the assumption of a well-defined single crystal face. A crucial parameter to carry this measurement is to know at which potential the hydrogen monolayer is formed. However, determining this is difficult, then it has been proposed to use as reference the end point potential and place the potential just before HER takes places. This depends on the electrode surface roughness, temperature and scan rate.[18, 19] In addition, this method presents some limitations: for instance when tested on highly porous electrodes using low potential scan rates such as 5 mV s^{-1} the voltammogram does not show reliable data.[2] Also, the nature of the electrolyte influences the height of the peaks and their position, and in the case of metallic particles using supports the hydrogen atoms tend to diffuse to surfaces where the support is not covered.[2] Overall, this method is mainly used on d-metal electrodes mostly with a low error around 10%.[20]

b) CO adsorption method

CO adsorption method, also called CO stripping voltammetry, is used by "poisoning" the surface of the materials.[21] As in hydrogen adsorption method, in CO stripping a gas molecule is adsorbed at the surface at a potential where CO oxidation does not take place and is then removed resulting in a peak from which the underlying charge is calculated. As an example, Figure 4.5 shows different CO stripping curves for different materials.

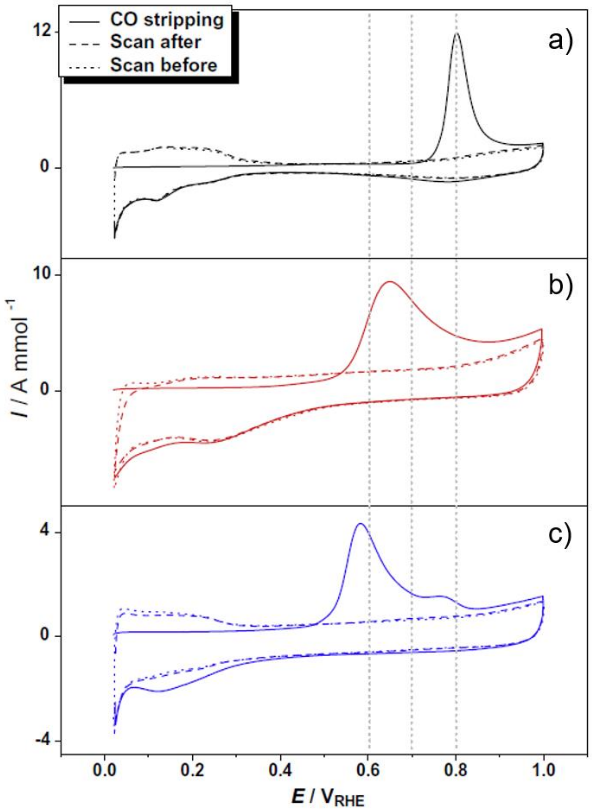

Figure 4.5 CO adsorption method of a) Pt, b) Ru and c) Ru@Pt in 0.5 M H_2SO_4 at 50 mV s^{-1} (taken and modified from[22]).

In CO adsorption a new parameter has to be considered, corresponding to the number of electrons *n* exchanged during the process (oxidation), then the determination of ECSA follows Eq. 4-6:[21]

$$ECSA = \frac{Q_{CO}}{n\,F\,S_{CO}} \times \frac{1}{mass\ sample} \qquad (Eq.\ 4\text{-}6)$$

where Q_{CO} corresponds to the charge under CO adsorption peak, F is Faraday's constant and S_{CO} is the saturation coverage of CO in mol cm^{-2} units. For a given material, the adsorbate monolayer depends on the adsorption potential, time, temperature, surface roughness and pretreatment and electrolyte solution. This is shown in Figure 4.5 where the same electrolyte solution and different materials showed a shift in the CO adsorption peak.[3] Unlike, the hydrogen method, CO stripping can be used in many metals and alloys but also presents some limitations or uncertainties such as the kind of CO bonding at the surface and the charge correction with respect to other contribution (i.e., double layer charge, metal oxide formation).[2, 23] A promising way to separate at least the Faradaic and non-Faradaic processes while using CO can be by infra-red (IR).[24] In general, despite the limitations and risks (i.e. poisonous) of working with CO, this stripping voltammetry is used mainly in a qualitative way that enables comparison of different catalysts activities as reported by *Souza et al.,*[25] and *Ochal et al.,*[22]

4.1.1.4 Underpotential deposition (UPD) of metals

Several electrochemical methods are used for characterizing the materials surface as the ones mentioned above, however, sometimes those methods cannot be applied or do not give acceptable results on some electrocatalysts that contain elements such as Ag, Cu or any other metal where hydrogen and oxygen adsorption does not take place (i.e., Ru).[2] Thus, UPD has been proven to be a powerful tool for probing the surface of those electrocatalysts, and can be used on nanoparticles, single and polycrystalline surfaces.[26 27]

UPD, as indicated by its name, refers to the deposition of a metal onto a foreign metal substrate at a potential (or a potential region) lower than the potential it would deposit onto itself. The deposition occurs at a potential less negative than the potential required for reduction of the metal.[3, 26] As a reference, the potential predicted by the Nernst equation for bulk deposition is taken into account since no bulk deposition (multilayers) is wanted, a monolayer is desired (Figure 4.6).[28] Thermodynamically, in order to obtain a monolayer the binding energy between the adsorbed metal and the substrate has to be greater that the affinity of the adsorb metal to itself.[27, 29]

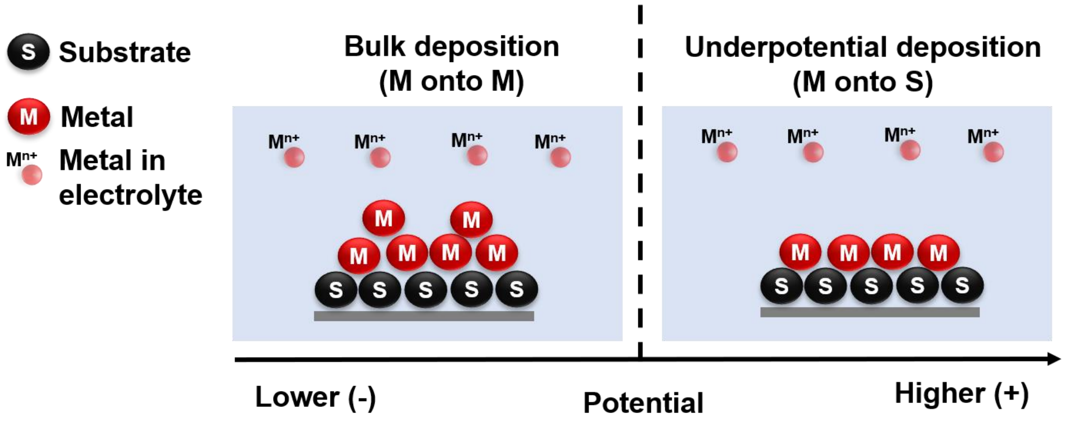

Figure 4.6 Scheme difference between bulk deposition and underpotential deposition.

Different techniques such as radiotracer, twin-electrode thin layer and others have been used to carry out UPD, however, cyclic voltammetry is frequently used compared to the other techniques since it allows the deduction of the potential between monolayer formation and bulk deposition as shown in Figure 4.7 where *Alia et al.,*[30] determined that potentials lower than 0.25 V bulk deposition of the metal occurs.[31, 32] As mentioned in chapter 3, a potential is swept linearly between two fixed potentials with a constant scan rate, and as the current is recorded a forward and backward scan result in a cyclic voltammogram.[33] Here, the forward and backward scans result in adsorption and desorption peaks, corresponding to the deposition and dissolution of the deposited metal, as represented in Figure 4.7.[26]

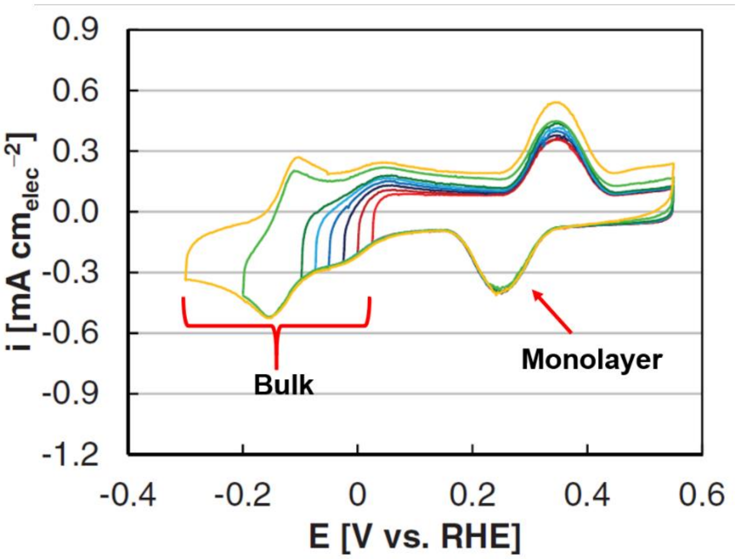

Figure 4.7 Voltammograms at variable potential range while testing mercury UPD onto iridium nanoparticles (taken and modified from[30]).

The principle behind UPD is similar to the gas adsorption methods, where the charge associated to the deposition of the metal onto the surface can be converted to ECSA, following the same equation as for hydrogen adsorption Eq. 4-5.[2] The metals most often used are Cu, Ag and Pb,[34-38] as well as Cd, Sn, Bi, Sb, Ni and Hg which have been used as well.[30, 39-43] Similarly to the other methods, UPD shares limitations such as the nature of the material affinity to the deposited ion, however, the main problem lays in the quantification of the charge corresponding to the deposited metal since a correction has to be applied where the double layer charge has to be considered. In addition, even if CV allows to identify the potential region for UPD, sometimes the proper identification of the potential for a monolayer formation is not possible. Another important limitation is that the value of the charge of the substrate are obtained, most of the times, under empirical consideration or assumptions, thus giving a margin of error. Despite the limitations, UPD measurements tend to have a high reproducibility if an established insight of the system is known.[2, 3, 26, 27, 44-46]

4.2. Surface area determination of $Ir_{1-x}Mo_xO_2$

Based on the above, this section presents the following experimental conditions that were taken into account to test the surface area of the materials synthesized in chapter 2 and electrochemically tested in chapter 3. The electrochemical surface area (ECSA) was determined by *in-situ* measurements such as double layer capacitance (C_{dl}) and underpotential deposition of mercury (UPD_{Hg}), as well as by *ex-situ* method BET used as point of reference, in order to understand the behavior presented in chapter 3 of the catalyst performances.

4.2.1. Experimental section

For all *in-situ* measurements, a three-electrode set up was employed with a RDE. The WE was a glassy carbon (GC) electrode with a surface are of 0.1963 cm^2, a Saturated Calomel Electrode (SCE) as a RE and a platinum wire as a CE. All three submerged in a 0.1 mol L^{-1} $HClO_4$ solution as supporting electrolyte. The collection of data was done by using a potentiostat Autolab PGSTAT 12 (see chapter 6 for further specifications). Also, all graphs potential (E), are reported in V vs Normal Hydrogen Electrode (NHE), therefore a correction of +0.242 V vs NHE was done.

4.2.1.1. Double layer capacitance

For each catalyst the following experimental procedure was employed:

i. iR-drop compensation was measured by potential feedback. A value of ca. 20 Ω was obtained and compensated in all cases.
ii. The catalyst was cycled between 0.89 and 1.09 V vs NHE at six different scan rates in a 0.1 mol L^{-1} $HClO_4$ solution, and CVs were recorded in the following order: 200, 150, 100, 50, 25 and 10 mV s^{-1}, normally 1 cycle for each scan rate.

During these measurements, the electrode was rotate at 1600 rpm, and for reproducibility, the measurements were done with at least 4 independent experiments.

4.2.1.2. UPD by Hg

For each catalyst the following experimental procedure was employed:

i. iR-drop compensation was measured by potential feedback. A value of ca. 20 Ω was obtained and compensated in all cases.
ii. The catalysts were cycled between 0.24 and 0.84 V vs NHE at four different scan rates in a 0.1 mol L^{-1} $HClO_4$ solution, and CVs were recorded

in the following order: 100, 75, 50, and 25 mV s^{-1}, normally 1 cycle for each scan rate. This step is in to collect blank CVs.

iii. 5 µL of a 1 mol L^{-1} of mercury nitrate solution was added to give a final concentration of 1mM in the final solution, and CVs were recorded once again at four different scan rates in the following order: 100, 75, 50, and 25 mV s^{-1}, normally 2 cycles for each scan rate. Between each scan rate, an electrochemical conditioning consisting of 10 cycles in the range between 1.24 and 1.54 V vs NHE in the OER region, were performed at a scan rate of 100 mV s^{-1}.

As an example, the sequence is as follows:

1) Scan 1 cycle at the four different sweep rates in the potential range 0.24 – 0.84 V vs NHE in a 0.1 mol L^{-1} $HClO_4$ solution.
2) After the last scan at 25 mV s^{-1}, mercury nitrate is added. Then, 2 cycles at a scan rate of 100 mV s^{-1} in the same potential range are recorded.
3) Electrochemical conditioning: 10 cycles are performed in potential range 1.24 – 1.54 V vs NHE. This is the OER region.
4) Lastly, 2 cycles at a scan rate of 100 mV s^{-1} between 0.24 – 0.84 V vs NHE are recorded once again.

Steps 2 and 4 are considered before and after OER, respectively. Those were done for each scan rate. During these measurements the electrode was rotate at 1600 rpm, and for reproducibility the measurements were done at least 3 times for each catalyst. In order to process the desorption monolayer the Coulombic charge of 138.6 µC cm_{Ir}^{-2} was used as a conversion of factor.[30]

4.2.1.3. BET

Physisorption studies were performed with N_2 at 77 K using a Belsorp-max apparatus from MicrotracBEL. Before analysis, the samples were outgassed at 423 K for 12 h under 0.1 Pa. The BET processing was carried out in the relative pressure range 0.05–0.25.

4.3. Results and discussion

4.3.1. CO Adsorption method

An important parameter in normalizing activities of porous electrocatalysts is real surface area of the catalyst. As a first attempt to carry out this, CO stripping voltammetry was applied in order to observe the poisoning of it onto the Ir-Mo oxides. Usually, to apply this method the first step is to determine the potential where a probe molecule is adsorbed at the surface considering that CO oxidation does not occur, once this is found, the potential sweep back when removing the adsorbed molecule leaves an oxidation peak.

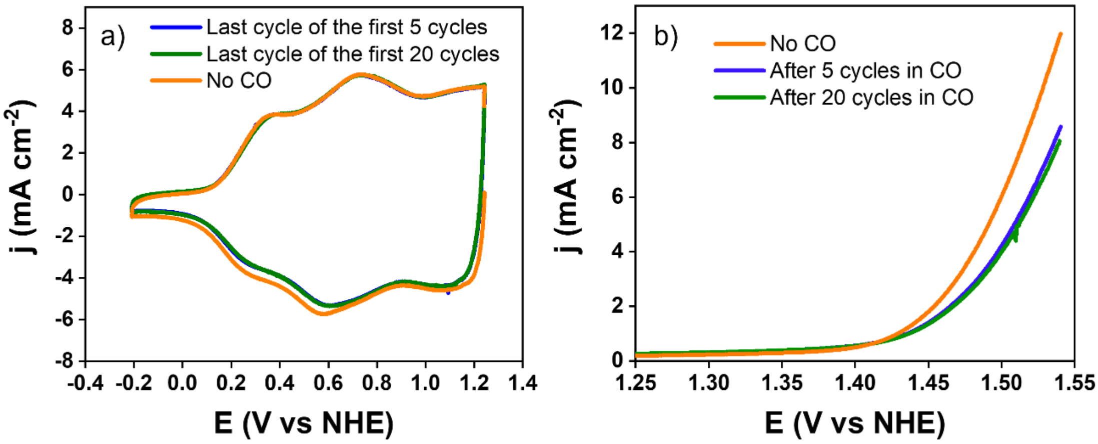

Figure 4.8 a) Cyclic voltammograms (last cycle) of IrO_2 commercial at 200 mV s^{-1} in 0.05 M H_2SO_4 under CO atmosphere (blue and green) and air (orange) and b) OER of IrO_2 commercial at 10 mV s^{-1} in 0.05 M H_2SO_4 under air (orange) and CO (blue and green) atmosphere.

Based on this, CO stripping was tested firstly onto non-porous IrO_2 commercial, and as reference a forward scan in no CO atmosphere in the potential range where OER takes place was recorded (Figure 4.8b, orange line) as well as CV (Figure 4.8a, orange line). After this, the electrolyte (0.05 M H_2SO_4) was consecutively bubbled with CO for at least 15 min while the electrode was maintained submerged. The potential was then cycled firstly 5 times (Figure 4.8a, blue line) from -0.2 V to 1.2 V at constant scan rate of 200 mV s^{-1} in order to observe the strip off or poisoning of the CO onto the surface followed again by a forward scan in the OER region (Figure 4.8b, blue line). Lastly, 20 cycles (Figure 4.8a, green line) were recorded from -0.2 V to 1.2 V at the same constant scan rate in order to observe if by increasing the cycling the CO adsorption could take place. However, as observed in Figure 4.8a, no change is visible i.e., oxidation peak is not present on the CV, meaning that no poisoning or adsorbed molecule was achieved onto the surface of the oxide. After these 20 cycles, a forward scan again took place between 1.24 – 1.54 V, and the OER performance decrease while CO was constantly bubbled increasing the overpotential.

These measurements confirmed that CO stripping is usually employed where the catalyst material to be able to chemically adsorb CO as a monolayer where the catalyst has to be in its fully reduce state i.e., metallic state. Otherwise CO will poorly (or no) adsorbs onto the surface of oxides, thus CO stripping is not feasible.[47, 48] Furthermore, *Trasatti et al.,*[2] mentioned as major drawback of this method that the adsorbate may depend on surface charge, and it has been found that the monolayer depends on the metal nature and crystallite size i.e., Pt.[49] Based on the stated above regarding the oxidation state of the catalyst, and the results of XPS and XANES presented in chapter 3, no further measurements involving CO were done since $Ir_{1-x}Mo_xO_2$ catalysts oxidation states are either Ir^{3+} or Ir^{4+}. Then, double layer capacitance and underpotential deposition of metal were considered as electrochemical methods for ECSA estimation.

4.3.2. Double layer capacitance (C_{dl})

As previously mentioned, the capacitance method consists in cycling the electrode at different scan rates in a non-Faradaic charging region to be able to estimate ECSA. However, an important parameter to be able to determine this value is the reference capacitance (C^*) since it depends strongly on the electrode potential, surface structure and electrolyte. Therefore, and as reported previously by *Faustini et al.,*[12] there is no existing reference capacitance to normalize the differential capacitance (C_{dl}) on iridium-based catalyst prepared by spray drying technique in order to avoid a high percentage of error that could influence the ECSA.[3]

Based on the above, the double layer capacitance (C_{dl}) in-situ electrochemical method was measured in order to observe how the ECSA may evolve when tested in the following section. Also, in this section and in the followings, based on the results presented in chapter 3, the catalysts containing 10, 30 and 50-Mo calcined at 450, 500, 550 and 600 °C were the ones assessed by in-situ electrochemical methods. By testing the catalysts at those four calcination temperatures allows to observe how the capacitance in this case may evolve instead of just selecting the catalyst that performed the best towards OER.

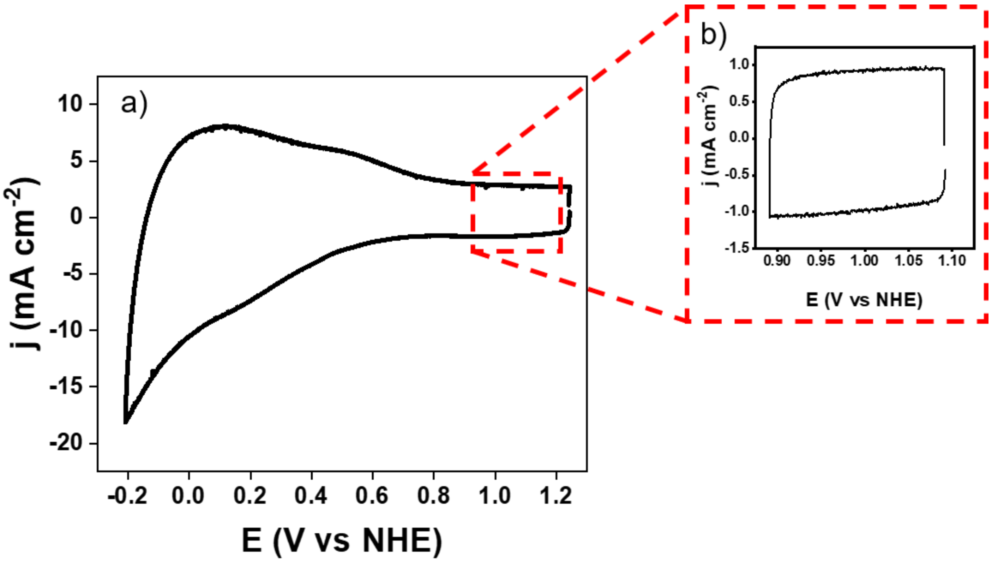

Figure 4.9 a) Cyclic voltammogram of 50-Mo@550 recorded at a scan rate of 25 mV s^{-1} in 0.1 M $HClO_4$ and b) zoom in non-Faradaic.

Firstly, a scan at 25 mV s^{-1} in the range -0.2 V to 1.2 V vs NHE (Figure 4.9a) was performed in order to determine the non-Faradaic region, which correspond to the region between 0.89 V to 1.09 V vs NHE as presented in Figure 4.9b. Despite the sample used for determined the potential range, all catalysts used in this part showed the same CV. All catalyst films onto the GC electrode were recorded at six different scan rates, as this is required for normalization procedure. CVs presented in Figure 4.10 were carried out at various scan rates from 10 mV s^{-1} which correspond to the inner curve (brown line) up to 200 mV s^{-1} which is the outer curve (purple line). From those data it is possible to determine the charging current density (j_C) of the electrodes at each scan rate by following Eq. 4-7:

$$j_C = j_a - j_c \qquad \textit{(Eq. 4-7)}$$

j_a and j_c correspond to the anodic and cathodic current density, respectively, taken from the CVs in Figure 4.10. From Figure 4.10, interestingly the samples that exhibited the best performance towards OER are the ones that showed a bigger size i.e., high charge, than the rest of temperatures. Also, apparently the only series that showed a drastic change in size was 10-Mo (Figure 4.10a), where the CVs of the sample calcined at 600 °C are reduced by almost five times when compared to 450 °C sample.

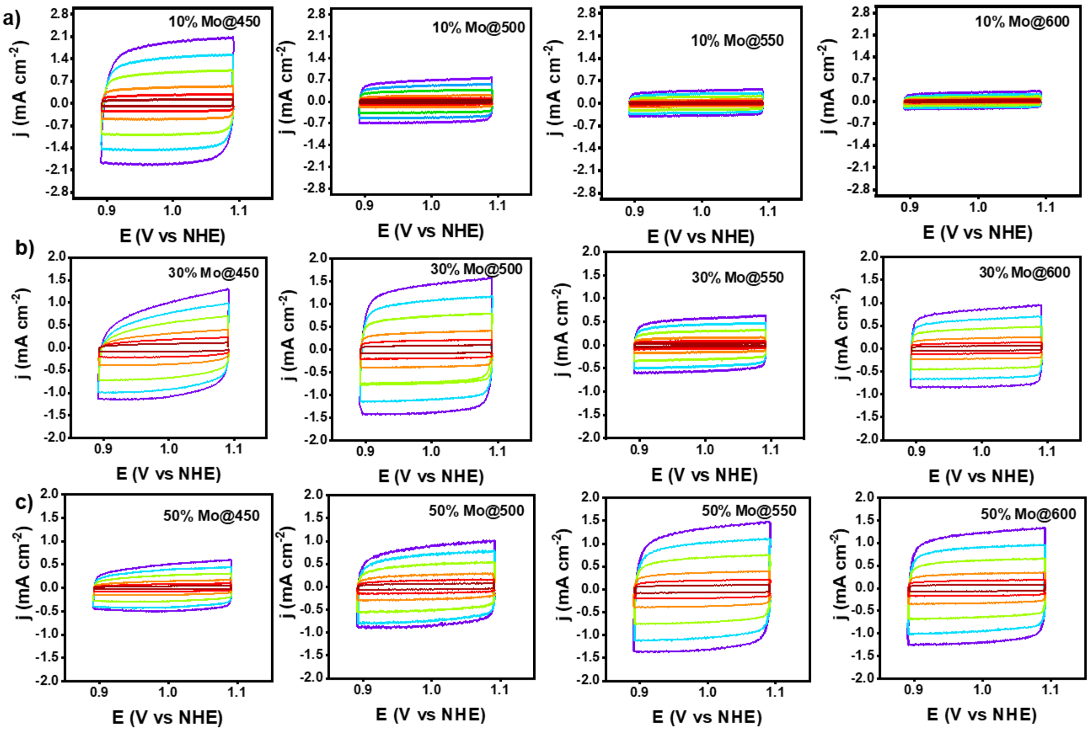

Figure 4.10 Cyclic voltammograms measured in a non – Faradaic region in 0.1 M $HClO_4$ at multiple scan rates: 0.2, 0.15, 0.1, 0.05, 0.025 and 0.01 V s^{-1} for a) 10, b) 30, and c) 50-Mo samples obtained after calcination in air at different temperatures.

It is then possible to obtain the value of the C_{dl} by plotting a graph of j_c versus scan rate. Figure 4.11 shows the linear regression (the difference obtained from Eq. 4-7) measured at 1.0 V vs NHE as function of scan rate as well as the evolution of the C_{dl}, extracted from the slope:

$$Slope = \frac{j_a - j_c [\mathrm{mA\ cm^{-2}}]}{2\ \Delta v\ [\mathrm{mV\ s^{-1}}]} \times 10^3 = C_{dl}\ [\mu F\ cm^{-2}] \qquad (Eq.\ 4\text{-}8)$$

In general, from Figure 4.11a, b and c, and from the equation presented previously, the higher the slope the higher the ECSA and C_{dl}.

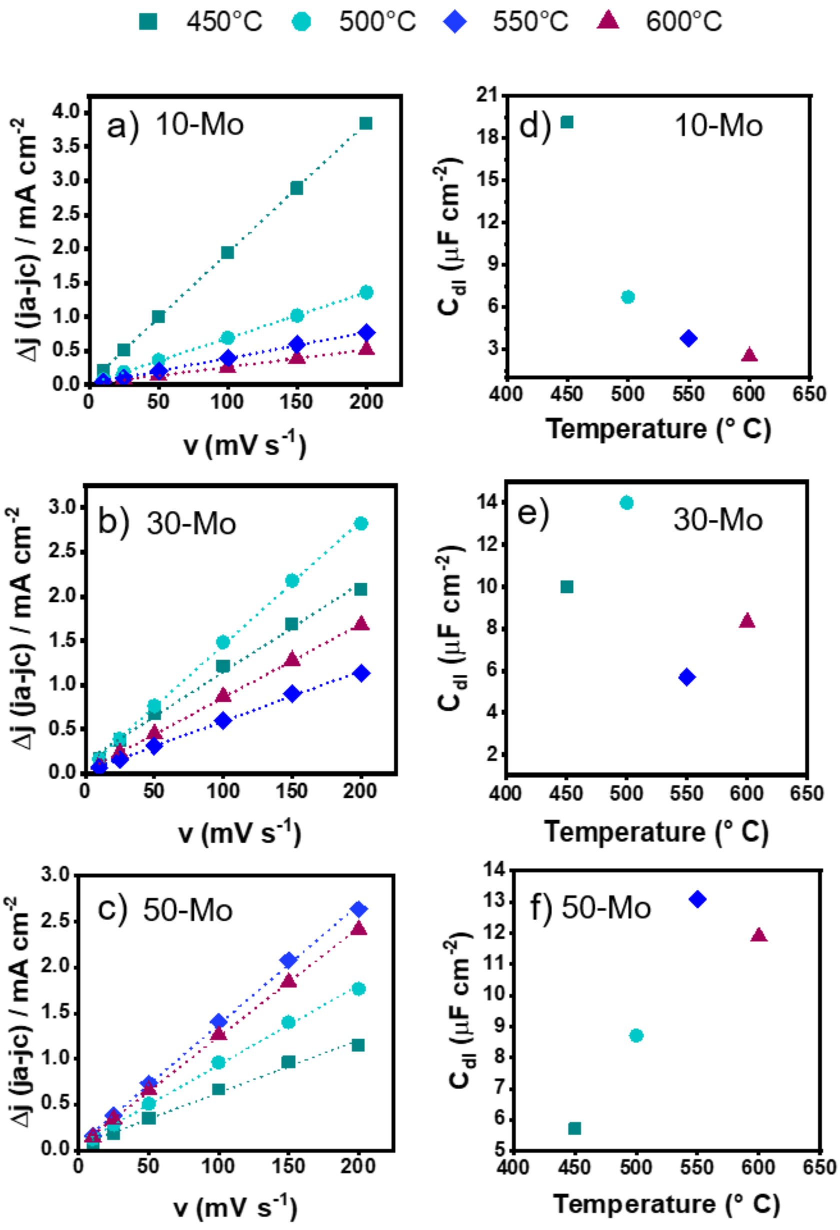

Figure 4.11 a, b, c) The difference between anodic and cathodic charging current density measured at 1.0 V vs NHE plotted as function of scan rate, and d,e,f) the evolution of the differential capacitance (Cdl) estimated from cyclic voltammograms experiments in the non-Faradaic region in 0.1 M $HClO_4$;

Figure 4.11d, e and f show the evolution of the C_{dl}, where the value corresponding to samples at which they presented a good OER response are higher. In the case of 10-Mo, the capacitance evolution is the same as the one presented by *Faustini et al.,*[12] for pure IrO_2, and by *Grupioni et al.,*[50] for $Ir_{0.3}Mn_{0.7}O_2$ in the temperature range 400-550 °C. On the other hand, for both 30 and 50-Mo samples, the behaviour differs, as an increase in C_{dl} is observed as the temperature is increasing but once this one reaches the optimal calcination temperature for each molybdenum content the C_{dl} value drops. Overall, the catalysts that exhibit higher C_{dl} values than the rest among their series, suggests high values of the electroactive surface area. This result agrees with SEM analysis in chapter 2 that show a decrease of the porosity at higher temperatures. Moreover, *Grupioni et al.,*[50] and *Zheng et al.,*[51] have reported that electrocatalysts annealed between 400-450 °C results in high charge capacitance electrodes which ends up in high surface area.

Since in this section no ECSA values are presented, it is important to remark the variation of it or the possible high error when the reference capacitance ($\boldsymbol{C^*}$) is selected. This value can be either the specific capacitance of the sample which is consider not to be practical or the capacitance of an atomically smooth planar surface of the material per unit of area under similar electrolyte conditions.[52] In the literature a variety of values haven been reported for both alkaline and acidic solution. For instance, for $Ir_{0.3}Mn_{0.7}O_2$ [50] an assumed value of 80 µF cm^{-2} was used due to measurements were done in acidic solution (0.5 M H_2SO_4) while other papers report 35 µF cm^{-2} for a 1 M H_2SO_4 solution,[52] while for commercial IrO_2 a value of 40 µF cm^{-2} is considered a reference capacitance in 1 M NaOH solution. However, since $\boldsymbol{C^*}$ varies from 15 to 110 µF cm^{-2} in H_2SO_4,[52] we discarded this method due to its dependence to surface morphologies and chemical composition.

4.3.3. BET

The well-known BET ex-situ method for surface analysis, is without a doubt the most popular technique to obtain reliable surface area values. Therefore, for $Ir_{1-x}Mo_xO_2$ (x = 0.1, 0.3 and 0.5) electrocatalysts calcined at 450, 500, 550 and 600 °C surface areas were assessed by this method with the purpose of using them as comparison values for the following section concerning underpotential deposition.

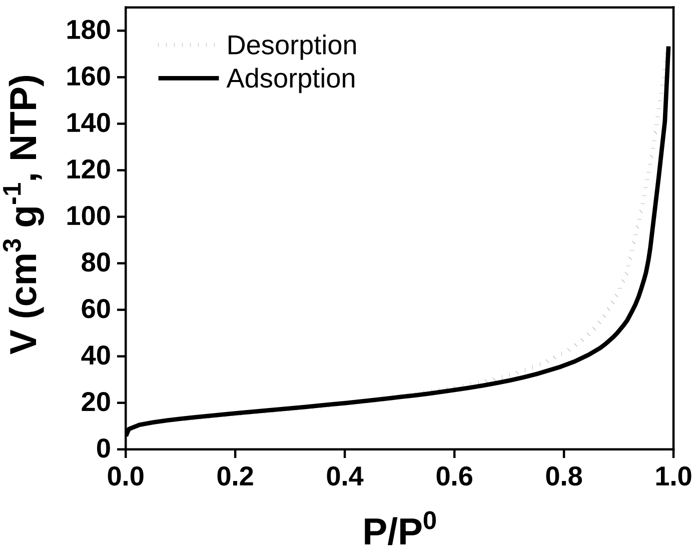

Figure 4.12 N_2 adsorption and desorption isotherms obtained at 77 K for 50-Mo@550

As an example, Figure 4.12 shows the adsorption isotherm of 50-Mo calcined at 550 °C which displays a Type II isotherm (see Figure 4.1). This is the most common isotherm obtained when using BET on non-porous or macroporous materials,[7, 53] confirming that the $Ir_{1-x}Mo_xO_2$ (x = 0.1, 0.3 and 0.5) electrocatalysts are macroporous adsorbents. The other electrocatalysts studied displayed the same isotherm. In addition, the hysteresis loop is often identified with specific pore structures. In the case of $Ir_{1-x}Mo_xO_2$, Figure 4.12 exhibits a type H1 where the desorption and adsorption lines are almost vertical and nearly parallel over a high relative pressure (P/P^0), and this type is also associated with porous materials.[53]

The ECSA values, determined using the BET equation, are listed in Table 4.1. The measurements show that $Ir_{1-x}Mo_xO_2$ samples such as 10-Mo@450, 30-Mo@500 and 50-Mo@550 has a much larger surface area than commercial IrO_2 (29 m^2 g^{-1}), and pure Ir oxide prepared under the same conditions and same calcination temperature.[12] In addition, among each molybdenum series, the samples which displayed better performances towards OER in chapter 3, present as well higher values of ECSA.

	IrO_2 [12]	**10-Mo**	**30-Mo**	**50-Mo**
Temperature (° C)	**S_{BET} ($m^2\ g^{-1}$)**	**S_{BET} ($m^2\ g^{-1}$)**	**S_{BET} ($m^2\ g^{-1}$)**	**S_{BET} ($m^2\ g^{-1}$)**
450	30	64	50	24
500	29	49	74	27
550	17	29	40	55
600	-	22	76	29

Table 4.1. BET surface area of the $Ir_{1-x}Mo_xO_2$ (x = 0.1, 0.3 and 0.5) catalyst sample and pure IrO_2.

The literature relates the change in surface area by the size of the crystallite, however, $Ir_{1-x}Mo_xO_2$ (x = 0.1, 0.3 and 0.5) and pure IrO_2 by *Faustini et al.,*[12] present the same crystallite size around ~ 2 nm. Therefore, the increase in surface area in these samples cannot be associated to the crystallite size or to which sample crystallizes first. On the contrary, it can be associated to the presence of more active sites. However, BET technique does not provide this information.

4.3.4. Underpotential deposition of mercury

The electrochemical active surface area (ECSA) serves as a key parameter for comparison between electrocatalysts since it provides a connection between the active catalytic sites of the material and its activity.[54] BET measurements allowed to obtain a reference value for surface area, and despite of it being considered as a solid value, the major drawback of its used with $Ir_{1-x}Mo_xO_2$ oxides is the fact that this method requires up to several hundreds of milligrams of material to give reliable values. Electrochemical techniques, such as carbon monoxide stripping (section 4.3.1) and underpotential deposition (UPD), allow a direct measurement of the ECSA of the material onto the electrode, and only require very small amounts of material compared to BET, in the order of the microgram in our case. Therefore, UPD became of great interest along with a recent study on measuring ECSA of commercial iridium oxide by mercury underpotential deposition (Hg-UPD) where *Alia et al.,*[30] estimated surfaces that resulted in values close enough to the ones calculated from BET tests. In addition, the method allowed to test the oxide before and after OER measurements, thus assessing the morphological stability of the catalyst after the catalytic reaction.

Based on the above, and using the double layer capacitance and BET as a guidance for testing the evolution of ECSA by Hg-UPD while adapting slightly the methodology implemented by *Alia et al.,*[30], this section presents the expansion of the method to porous $Ir_{1-x}Mo_xO_2$ oxides with x = 0, 0.1, 0.3, and 0.5. The electrochemical results are presented in experimental order to demonstrate the coherence and the reproducibility among the measurements.

4.3.4.1. Pure IrO_2

Firstly, ECSA was evaluated on pure IrO_2 (x = 0) samples calcined in the range 400 – 800 °C in order to ensure applicability of this method on ultraporous materials. Figure 4.13a, presents voltammograms at a variable potential range at 50 mV s^{-1} with the aim to determine the potential range where both mercury bulk and the monolayer are form. It can be observed in Figure 4.13b that during the anodic scan, bulk mercury oxidation (arrow) appeared at potentials greater than -0.15 V (visible in purple, blue, magenta, green and yellow lines), and its presence depends on the lower limit potential. Also, the blue circle highlights the mercury monolayer desorption peak at ~0.7 V (red line).

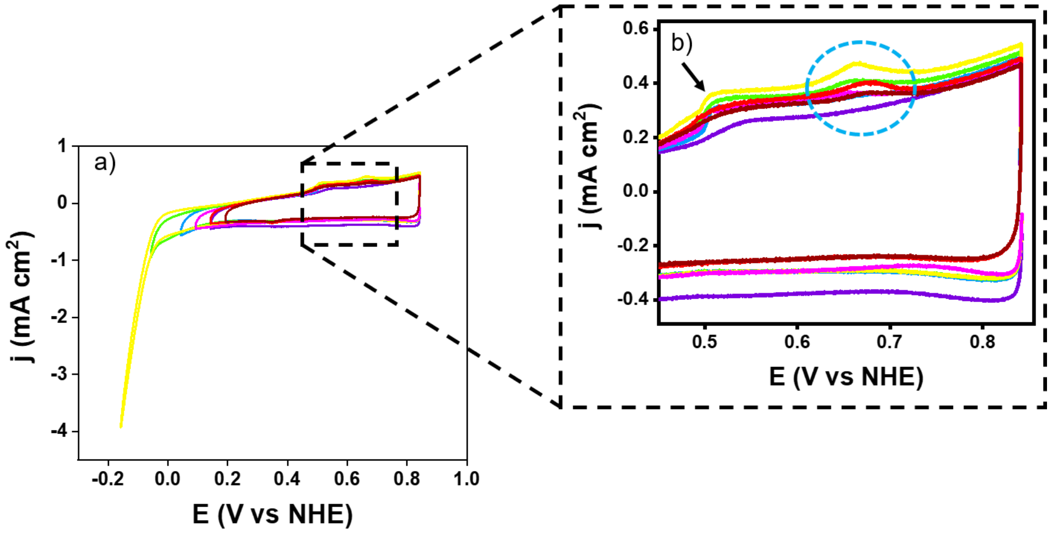

Figure 4.13 a) CVs of IrO_2@400 at variable potential range at 50 mV s^{-1} in 0.1 M $HClO_4$ containing mercury nitrate solution and b) Zoom in the potential range 0.5 – 0.84 V vs NHE.

Therefore, based on the above, the potential limits used to get the cyclic voltammogram for pure IrO_2 in both background (only 0.1M $HClO_4$ solution) and Hg-containing solution, are from 0.24 V to 0.84 V vs. NHE. This potential range was selected, which corresponded to the potential range of the red line in Figure 4.13, due to the sole mercury monolayer desorption peak (described before in section 4.1.1.4) at ~0.7 V (highlighted by blue circle). Also, all samples for all calcination temperatures presented an anodic desorption peak at ca. +0.7 V vs. NHE.

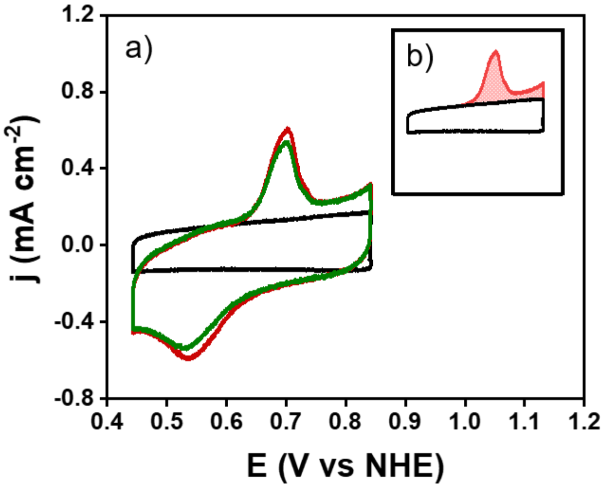

Figure 4.14 a) Cyclic voltammogram of IrO_2@450 recorded at a scan rate of 50 mV s^{-1} in 0.1 M $HClO_4$ (background), and 0.1 M $HClO_4$ containing 1 mM mercury nitrate solution, and b) Inset of the area of the charge current corresponding to the anodic peak.

In Figure 4.14, the black line represents the electrode CV response in the background electrolyte (0.1 M $HClO_4$) while red and green lines represent before and after OER cycling, respectively, cyclic voltammograms behavior in Hg-containing solution. In addition, the insert (Figure 4.14b) displays the area that represents the charge of the anodic peak which was estimated from the integration of the peak area, both before and after OER characterization. Moreover, the cyclic voltammogram recorded in the background electrolyte served as a guideline for the subtraction of other current while preserving the charging phenomenon generated by mercury desorption, this charging corresponds to the colored red zone in Figure 4.14b.

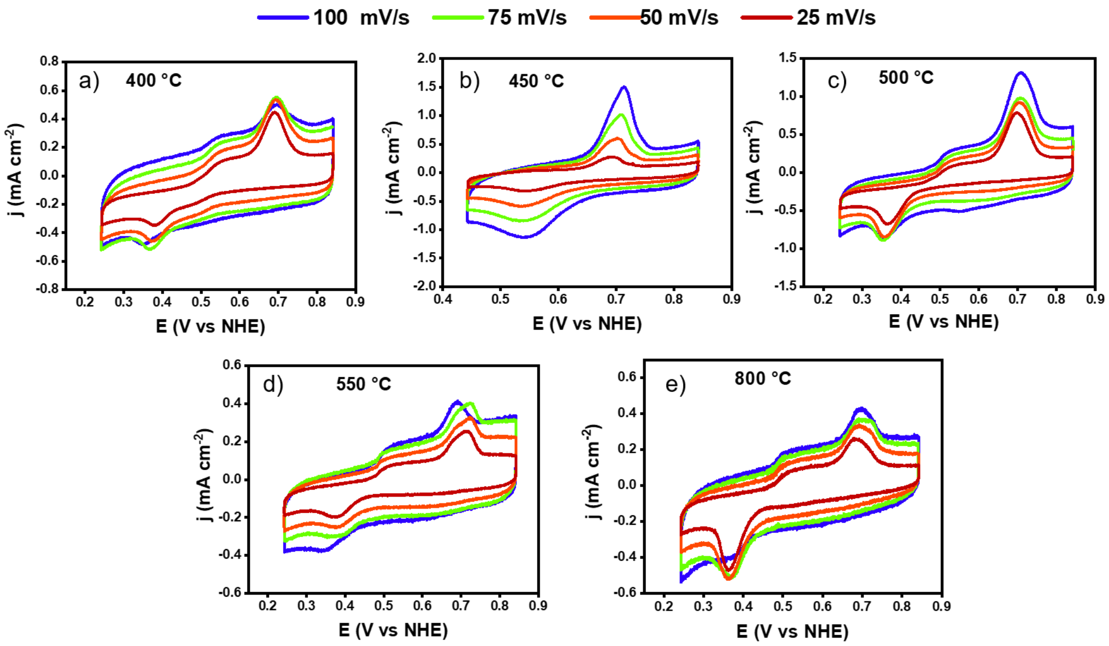

Figure 4.15 Cyclic voltammograms of IrO_2 samples calcined in the temperature range 400-800 °C recorded at multiple scan rates in a 0.1 M $HClO_4$ containing 1 mM mercury nitrate solution.

The anodic peak was selected for integration of the charge rather the cathodic peak since in some samples the cathodic peak did not show well defined limits, which is crucial for the integration of the peak, as observed in Figure 4.15a, b and d. Those poorly defined cathodic peaks were as well noted by *Alia et al.*[30] Also, from Figure 4.15, when comparing the Hg-UPD peak among them, the samples calcined at 400, 450 and 500 °C are presenting a much larger current density than the other two samples. Furthermore, Figure 4.15 shows only the CVs before the 10 cycles over the OER region (+1.24 to +1.54 V vs. NHE), since the after CVs displayed almost similar behaviors before and after scanning in the OER region. This can be better observed in Figure 4.16, where very little variations regarding the charging current before and after electrochemical condition were visible. In addition, as the material aging temperature is increased the slope of the charging current starts to drop gradually. Similar behavior was observed in section 4.3.2 regarding the double layer capacitance.

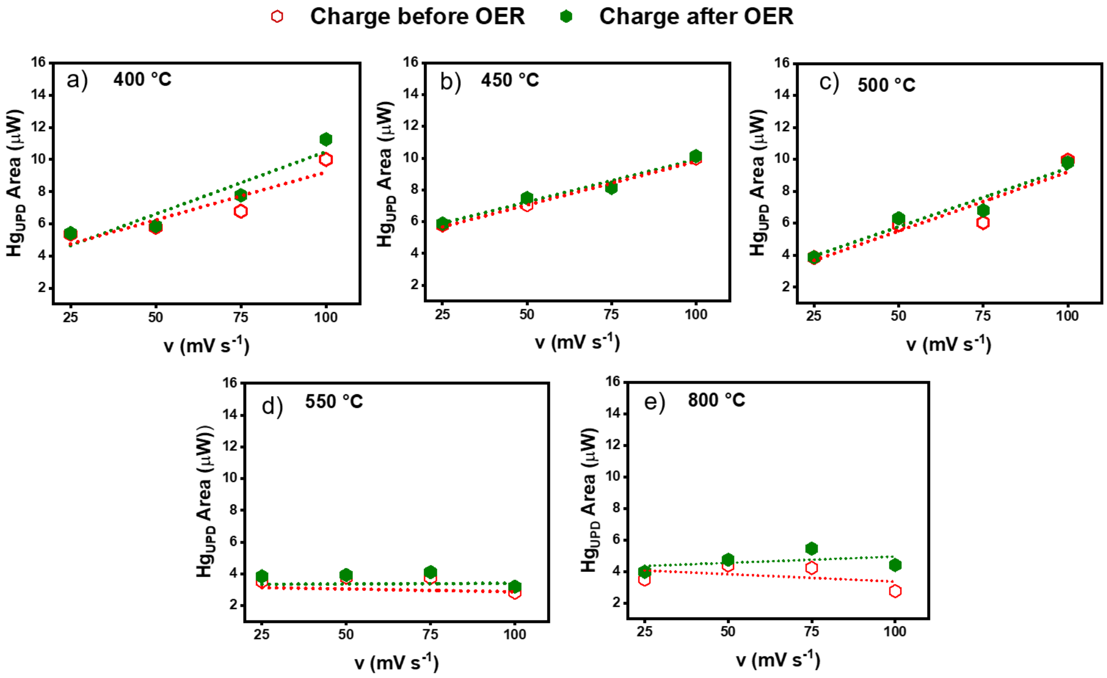

Figure 4.16 Charges before and after electrochemical conditioning of OER on IrO_2 samples calcined in the temperature range 400-800 °C in a 0.1 M $HClO_4$ containing 1 mM mercury nitrate solution.

At this point, a Coulombic charge of 138.6 μC cm^{-2} was used as a conversion factor to obtain the ECSA,[30] and following the above IrO_2@400 which presents the highest slope resulted with the highest ECSA value as presented in Table 4.2. Focusing on the surface area before OER, a decrease from 30 m^2 g^{-1} to 14 m^2 g^{-1} when increasing the thermal treatment from 400 to 800 °C, and after OER values are presenting the same trend. Since the Hg-UPD values are in the same range as the ones previously determined by BET method,[12] it is concluded that the free Hg^{2+} ions in the solution have the same access to adsorption sites as the N_2 probe gas onto the highly porous structure generated by spray-drying technique. Then, mercury ions are adsorbed both at the surface as well as inside the pores. Since results of pure IrO_2 were satisfactory, Hg-UPD was further investigate for $Ir_{1-x}Mo_xO_2$ oxides.

Temperature (° C)	**S_{BET} (m^2 g^{-1})**	**S_{HgUPD} before OER (m^2 g^{-1})**	**S_{HgUPD} after OER (m^2 g^{-1})**
400	32	30 ± 1.3	32 ± 2.1
450	30	28 ± 2.5	28 ± 2.7
500	29	26 ± 1.4	27 ± 1.6
550	17	17 ± 2.2	18 ± 2.1
800	13	14 ± 1.5	16 ± 0.5

Table 4.2. ECSA values before and after electrochemical conditioning of OER on IrO2 samples calcined in the temperature range 400-800 °C in a 0.1 M $HClO_4$ containing 1 mM mercury nitrate solution.

4.3.4.2. Ir-Mo oxides

Hg-UPD protocol used on pure IrO_2 was performed on $Ir_{1-x}Mo_xO_2$ (x = 0.1, 0.3 and 0.5) oxides to estimate their ECSA. However, since the Hg-UPD method was going to be used for the first time onto mixed oxides, it was necessary to determine that the 100% molybdenum oxide particles were also sensible when subjected to mercury adsorption due to the fact that the nature of the material can affect the UPD process.

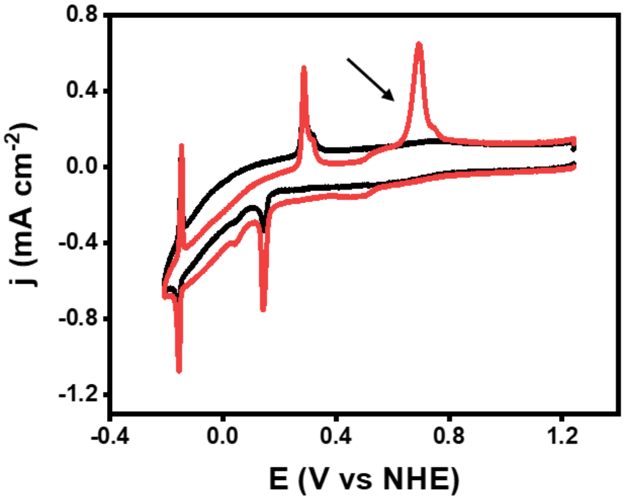

Figure 4.17 Cyclic voltammograms of 100-Mo@550 recorded at 20 mV s^{-1} in a 0.1 M $HClO_4$ (background) and in a 0.1 M $HClO_4$ containing 1 mM mercury nitrate solution.

Figure 4.17, displays the electrochemical response of MoO_3 in the potential range -0.2 V to 1.24 V vs NHE at 20 mV s^{-1} in both background (black line) and Hg-containing solution (red line). The cyclic voltammogram shows several adsorption and desorption peaks, we thus concluded that the method is suitable to continue with the Ir-Mo oxides since the peak pointed by the arrow around +0.7 V vs. NHE in the presence of mercury nitrate (red line) coinciding with pure IrO_2 electrochemical response, allowing the desorption peak to be easily identified when investigating the substitution of iridium for molybdenum. Following the protocol, all Ir-Mo oxides were recorded as well at multiple scan rates (100, 75, 50 and 25 mV s^{-1}), however, with the aim to observe the evolution of the CV shape and characteristic anodic peak at ca. +0.7 V vs NHE of all Ir-Mo oxides, the 25 mV s^{-1} CVs were chosen to show the behavior as represented in Figure 4.18.

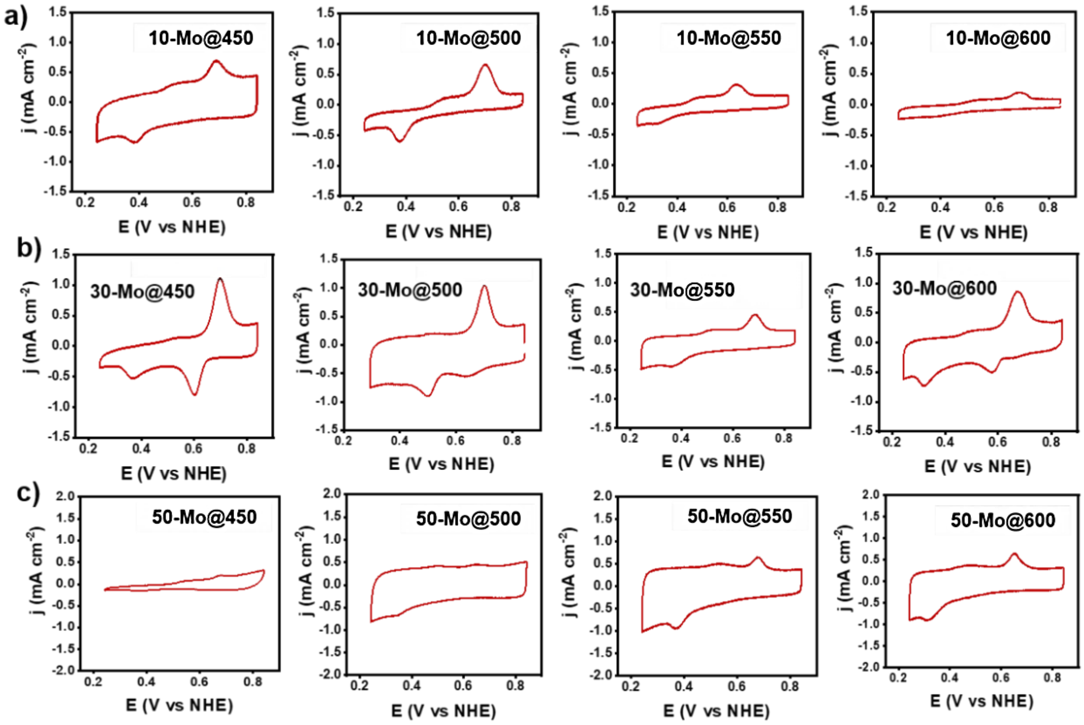

Figure 4.18 Cyclic voltammograms of $Ir_{1-x}Mo_xO_2$ samples calcined at different temperatures and measured at 25 mV s^{-1} for a) 10, b) 30, and c) 50-Mo in a 0.1 M $HClO_4$ containing 1 mM mercury nitrate solution.

The CVs in Figure 4.18, interestingly, displayed a similar behavior as Figure 4.10 in line with double layer capacitance ECSA measurements. For instance, for the 10-Mo CVs series (Figure 4.18a), as the calcination temperature increased the charge of the peak decreased as well similar to 10-Mo double layer capacitances CVs. Also, 30 and 50-Mo series showed the same trend as their corresponding double layer capacitance CVs but not as visible as for the 10-Mo series. The changes in CVs' shape such as the height or broadness of the peak might suggest the presence of more active sites where Hg ions deposit on.

All CVs are presenting a double hump on the anodic scan: the small hump did not increase (or decreased) with calcination temperature or scan rates variation. Therefore, was considered as the limit where the peak (at 0.7 V) started to form. Also, the presence of the small hump could result from the difference between Ir and Mo desorption sites for mercury. In a similar study, *Wang et al.,*[55] despite of using another adsorption metal for UPD onto IrO_2/SnO_2 catalyst, presented a similar hump at begining of the peak for the anodic Cu-UPD stripping but with no clear attribution. For the reverse scan, only the 30-Mo series (Figure 4.18b) presented a double hump on the cathodic scan while the rest displayed only one peak.

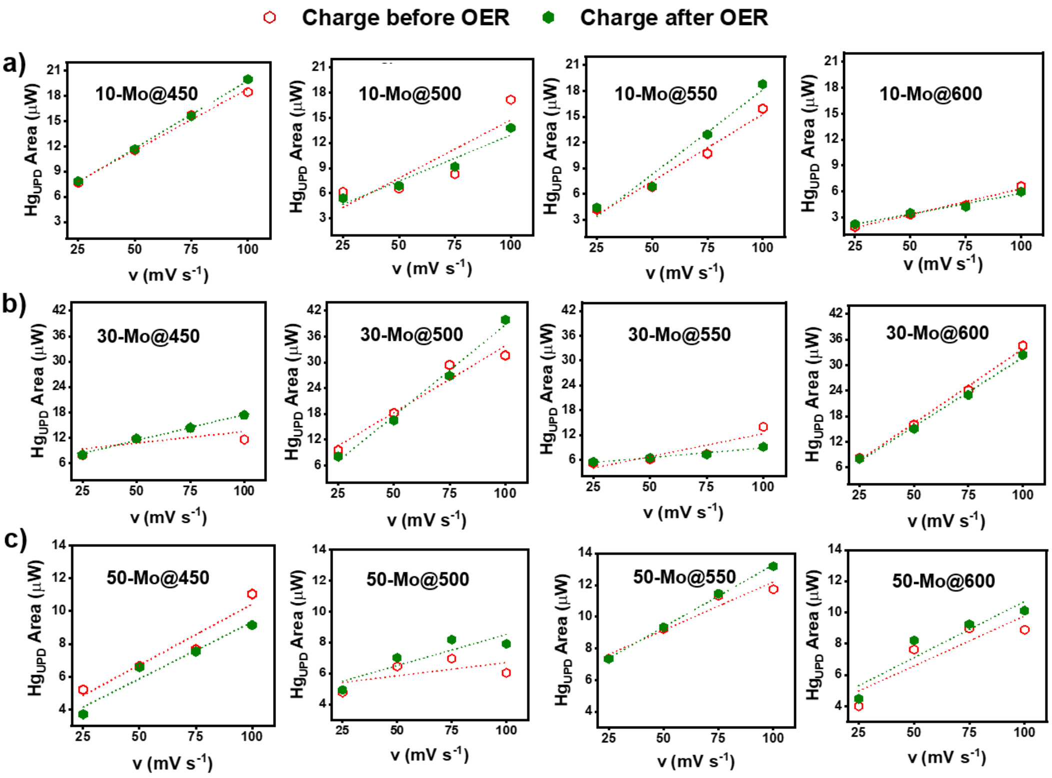

Figure 4.19 Charges before and after electrochemical conditioning of OER of $Ir_{1-x}Mo_xO_2$ samples calcined at different temperatures and measured at different scan rates for a) 10, b) 30, and c) 50-Mo in a 0.1 M $HClO_4$ containing 1 mM mercury nitrate solution.

10-Mo

Temperature (° C)	**S_{BET} (m^2 g^{-1})**	**S_{HgUPD} before OER (m^2 g^{-1})**	**S_{HgUPD} after OER (m^2 g^{-1})**	**C_{dl} (µF cm^{-2})**
450	64	52 ± 1.2	53 ± 1.2	19.10
500	49	38 ± 1.3	35 ± 1.4	6.2
550	29	28 ± 0.6	31 ± 0.5	3.8
600	22	18 ± 2.5	19 ± 2.9	2.5

30-Mo

Temperature (° C)	**S_{BET} (m^2 g^{-1})**	**S_{HgUPD} before OER (m^2 g^{-1})**	**S_{HgUPD} after OER (m^2 g^{-1})**	**C_{dl} (µF cm^{-2})**
450	50	46 ± 1.2	49 ± 1.2	10
500	74	74 ± 0.8	70 ± 0.7	14
550	40	32 ± 1.3	31 ± 1.9	5.7
600	76	61 ± 0.7	59 ± 0.7	8.3

50-Mo

Temperature (° C)	**S_{BET} (m^2 g^{-1})**	**S_{HgUPD} before OER (m^2 g^{-1})**	**S_{HgUPD} after OER (m^2 g^{-1})**	**C_{dl} (µF cm^{-2})**
450	24	31 ± 0.7	27 ±0.07	5.7
500	27	31 ± 3.4	31 ± 2.2	8.7
550	55	57 ± 2.1	53 ± 2.3	13.1
600	29	32 ± 2.2	33 ± 0.7	11.9

Table 4.3. Summary of ECSA values before and after electrochemical conditioning OER on $Ir_{1-x}Mo_xO_2$ samples in a 0.1 M $HClO_4$ containing 1 mM mercury nitrate solution, BET measurements and capacitive current measurements.

As in pure IrO_2, a comparison of the performance of the Hg-UPD charge current as function of the temperature for $Ir_{1-x}Mo_xO_2$ is represented in Figure 4.19. Similarly, to pure IrO_2, the behavior of the slope of all the oxides agrees with the one observed in Figure 4.11 regarding the C_{dl}. Therefore, samples 10-Mo@450, 30-Mo@500, and 50-Mo@550 which present the highest slopes before and after OER treatment would result in high ECSA values. For the conversion, the Coulombic charge of 138.6 µC cm^{-2} was used as well, since based on XRD results in chapter 2 the unit-cell parameters through the series remain constant, implying that iridium atoms are being replaced by molybdenum atoms without changing the crystal structure. Therefore, the coulombic charge can be assumed to remain identical to the iridium series.

As observed in Table 4.3, the ECSA values after OER cycling do not present significant variations, which outlines the stability of the material. When compared to the BET method, it presents favorable numbers, and the trends observed for both Hg-UPD and BET are similar. Moreover, when observing the C_{dl} trend, is expected that both UPD and BET exhibits the same behavior, however, in 30-Mo series this is not present since the sample calcined at 600 °C (BET = 76 m^2 g^{-1}) presented a value slightly higher than the electrocatalyst (30-Mo@500, BET = 74 m^2 g^{-1}) that performed the best among this series towards OER. This discrepancy can be associated to the fact that samples came from different batches, meaning that the sample calcined at 600 °C was not the same powder batch calcined in the range 450 – 550 °C. On the other hand, Hg-UPD followed the capacitance trend, showing that among them 30-Mo@500 has the highest ECSA value. Moreover, when analyzing the OER performances of each series in chapter 3 by incorporating the ECSA values, it is visible that the performance was strongly influenced by the surface area thus resulting in 10-Mo@450, 30-Mo@500 and 50-Mo@550 as the most actives towards OER in their corresponding family. On the other hand, the only series in which the ECSA was strongly influenced by the calcination temperature in terms of crystallinity is the 10-Mo series where the surface area decreases as the temperature increases, similarly to pure IrO_2.[12]

Now, among the electrocatalysts that performed the best towards OER, 30-Mo@500 shows the highest Hg-UPD which is indicating that it has the highest surface active site, and that ECSA is not related to the amount of iridium in the catalyst. On the contrary, *Wang et al.,*[55] reported that iridium loading influenced the Cu-UPD stripping charge where Ir-nano benchmark catalyst resulted with the highest charge compared to the supported catalysts. Moreover, interestingly, from Table 4.3 some values are closer to BET than other ones, and these differences have been reported previously in the case of Zn-UPD[56] where Zn^{2+} ions were limited or could only access certain electrochemical accessible area of the IrO_x films due to poor mobility through the pores, resulting in an ECSA value that corresponded only to the 53% of BET. Therefore, $Ir_{1-x}Mo_xO_2$ oxides differences towards BET can be associated to a low or poor infiltration of the mercury ions into deeper pores presented on the oxides, as well as to the quality of the electrode coating and the catalyst loading.

4.4. Conclusions

In this chapter, the series of $Ir_{1-x}Mo_xO_2$ oxides across the composition range x = 0, 0.1, 0.3, 0.5, and 1 have been tested by a typical three-electrode electrochemical setup for double layer capacitance and underpotential deposition of mercury. The double layer capacitance method allowed to obtain a trend of the charging current behavior of the catalyst as the sintering temperature is increased which let on to have an insight into Hg-UPD method and BET behaviors. The Hg-UPD method results prove its relevance and applicability for porous and mixed oxides when tested in RDE. The electrochemical study showed that the ECSA reaches its highest values when the catalyst is calcined at the optimal calcination, meaning 10-Mo@450, 30-Mo@500 and 50-Mo@550, for then decreasing drastically due to the loss of porosity (higher crystallinity of the materials). The values obtained are consistent with BET measurements as confirmed by the robustness of the method. Finally, among the $Ir_{1-x}Mo_xO_2$ oxides, $Ir_{0.7}Mo_{0.3}O_2$ composition calcined at 500 °C outperformed the other two catalyst ($Ir_{0.9}Mo_{0.1}O_2$ and $Ir_{0.5}Mo_{0.5}O_2$, calcined at 450 and 500 °C, respectively) and presented the highest active sites surface area.

4.5. References

1. Zhu, P.; Zhao, Y., Effects of electrochemical reaction and surface morphology on electroactive surface area of porous copper manufactured by Lost Carbonate Sintering. *RSC Adv.*, 2017, *7* (42), 26392-26400.
2. Trasatti, S.; Petrii, O. A., Real surface area measurements in electrochemistry. *Pure Appl. Chem.*, 1991, *63* (5), 711-734.
3. Łukaszewski, M., Electrochemical Methods of Real Surface Area Determination of Noble Metal Electrodes – an Overview. *Int. J. Electrochem. Sci.*, 2016, 4442-4469.
4. Lohmann-Richters, F. P., et al., In situ determination of the electrochemically active platinum surface area: key to improvement of solid acid fuel cells. *J. Mater. Chem. A*, 2018, *6* (6), 2700-2707.
5. Brunauer, S., et al., Adsorption of Gases in Multimolecular Layers. *JACS*, 1938, *60* (2), 309-319.
6. Brunauer, S., et al., On a Theory of the van der Waals Adsorption of Gases. *JACS*, 1940, *62* (7), 1723-1732.

7. Naderi, M., Chapter Fourteen - Surface Area: Brunauer–Emmett–Teller (BET). In *Progress in Filtration and Separation*, Tarleton, S., Ed. Academic Press: Oxford, 2015; pp 585-608.
8. Zdravkov, B., et al., Pore classification in the characterization of porous materials: A perspective. *Open Chemistry*, 2007, *5* (2), 385-395.
9. Nasrollahzadeh, M., et al., Plant-Mediated Green Synthesis of Nanostructures: Mechanisms, Characterization, and Applications. In *An Introduction to Green Nanotechnology*, 2019; pp 199-322.
10. Hanaor, D. A., et al., Scalable surface area characterization by electrokinetic analysis of complex anion adsorption. *Langmuir*, 2014, *30* (50), 15143-52.
11. Connor, P., et al., The Determination of Electrochemical Active Surface Area and Specific Capacity Revisited for the System MnOx as an Oxygen Evolution Catalyst. *Z. Phys. Chem.*, 2020, *234* (5), 979-994.
12. Faustini, M., et al., Hierarchically Structured Ultraporous Iridium-Based Materials: A Novel Catalyst Architecture for Proton Exchange Membrane Water Electrolyzers. *Adv. Energy Mater.*, 2019, *9* (4), 1802136.
13. Bockris, J. O. M.; Otagawa, T., The Electrocatalysis of Oxygen Evolution on Perovskites. *J. Electrochem. Soc.*, 2019, *131* (2), 290-302.
14. Levine, S.; Smith, A. L., Theory of the differential capacity of the oxide/aqueous electrolyte interface. *Discussions of the Faraday Society*, 1971, *52* (0), 290-301.
15. Boggio, R., et al., Electrochemical surface properties of Co3O4 electrodes. *J. Appl. Electrochem.*, 1987, *17* (4), 828-840.
16. Tremblay, M. L., et al., Determination of the real surface area of powdered materials in cavity microelectrodes by electrochemical impedance spectroscopy. *Electrochim. Acta*, 2010, *55* (21), 6283-6291.
17. Diaz-Morales, O., et al., Hydrogen adsorption on nano-structured platinum electrodes. *Faraday Discuss.*, 2018, *210* (0), 301-315.
18. Woods, R., Hydrogen adsorption on platinum, iridium, and rhodium electrodes at reduced temperatures and the dertermination of real surface area. *Electroanalytical chemistry and interfacial electrochemistry*, 1974, *49*, 217-226.
19. Furuya, N.; Koide, S., Hydrogen adsorption on iridium single-crystal surfaces. *Surf. Sci.*, 1990, *226* (3), 221-225.
20. Hayes, M.; Kuhn, A. T., Determination of platinum catalyst surface area with potentiodynamic techniques — Effect of experimental parameters. *Applications of Surface Science*, 1980, *6* (1), 1-14.
21. Kohlmayr, G.; Stonehart, P., Adsorption kinetics for carbon monoxide on platinum in hot phosphoric acid. *Electrochim. Acta*, 1973, *18* (2), 211-223.
22. Ochal, P., et al., CO stripping as an electrochemical tool for characterization of Ru@Pt core-shell catalysts. *J. Electroanal. Chem.*, 2011, *655* (2), 140-146.
23. Gilman, S., A study of the adsorption of carbon monoxide and oxygen on platinum. Significance of the "polarization curve". *The Journal of Physical Chemistry*, 1962, *66* (12), 2657-2664.
24. Maillard, F., et al., Infrared Spectroscopic Study of CO Adsorption and Electro-oxidation on Carbon-Supported Pt Nanoparticles: Interparticle versus Intraparticle Heterogeneity. *The Journal of Physical Chemistry B*, 2004, *108* (46), 17893-17904.
25. Iúdice de Souza, J. P., et al., Performance evaluation of porous electrocatalysts via normalization of the active surface. *J. Appl. Electrochem.*, 2000, *30* (1), 43-48.
26. Mayet, N., et al., Probing the Surface of Noble Metals Electrochemically by Underpotential Deposition of Transition Metals. *Surfaces*, 2019, *2* (2), 257-276.
27. Swathirajan, S.; Bruckenstein, S., Thermodynamics and kinetics of underpotential deposition of metal monolayers on polycrystalline substrates. *Electrochim. Acta*, 1983, *28* (7), 865-877.
28. Sudha, V.; Sangaranarayanan, M. V., Underpotential deposition of metals – Progress and prospects in modelling. *J. Chem. Sci.*, 2005, *117* (3), 207-218.

29. Pangarov, n., Thermodynamics of electrochemical phase formation and underpotential metal deposition. *Electrochim. Acta*, 1983, *28* (6), 763-775.
30. Alia, S. M., et al., Mercury Underpotential Deposition to Determine Iridium and Iridium Oxide Electrochemical Surface Areas. *J. Electrochem. Soc.*, 2016, *163* (11), F3051-F3056.
31. Kolb, D. M., et al., Underpotential deposition of metals and work function differences. *J. Electroanal. Chem. Interf. Electrochem.*, 1974, *54* (1), 25-38.
32. Oviedo, O. A., et al., Experimental Techniques and Structure of the Underpotential Deposition Phase. In *Underpotential Deposition: From Fundamentals and Theory to Applications at the Nanoscale*, Springer International Publishing: Cham, 2016; pp 17-89.
33. Zhang, J., et al., Techniques for PEM Fuel Cell Testing and Diagnosis. In *PEM Fuel Cell Testing and Diagnosis*, 2013; pp 81-119.
34. Garcia, S., et al., Ag UPD on Au(100) and Au(111). *Electrochim. Acta*, 1998, *43* (19), 3007-3019.
35. Aniskevich, Y. M., et al., Determination of the Electrochemically Active Surface Area of PbSe and Bi2Te3 Films Using the Deposition of Lead Atoms. *Theor. Exp. Chem.*, 2019, *55* (1), 64-71.
36. Nakamura, M., et al., Surface X-ray diffraction study of Cu UPD on Au(111) electrode in 0.5 M H2SO4 solution: the coadsorption structure of UPD copper, hydration water molecule and bisulfate anion on Au(111). *Surf. Sci.*, 2002, *514* (1), 227-233.
37. Kuzume, A., et al., Copper underpotential deposition at high index single crystal surfaces of Au. *J. Electroanal. Chem.*, 2004, *570* (2), 157-161.
38. Feliu, J. M., et al., The behaviour of lead and bismuth adatoms on well-defined platinum surfaces. *Journal de Chimie Physique*, 2017, *88*, 1493-1518.
39. Brust, M., et al., Site-Specific Modification of Gold Nanoparticles by Underpotential Deposition of Cadmium Atoms. *ChemElectroChem*, 2018, *5* (12), 1586-1590.
40. Abaci, S., et al., The influence of counter anions on the underpotential deposition of mercury(II) on Au(111): temperature-dependent studies. *J. Electroanal. Chem.*, 2004, *571* (2), 169-176.
41. Meier, L. A., et al., Spontaneous deposition of Sn on Au(111). An in situ STM study. *Electrochem. Commun.*, 2008, *10* (10), 1583-1586.
42. Thiel, K. O., et al., Bismuth UPD on the modified Au(111) electrode. *J. Electroanal. Chem.*, 2010, *638* (1), 143-150.
43. Vaskevich, A., et al., Underpotential Deposition of Nickel on {111}-Textured Gold Electrodes in Dimethyl Sulfoxide. *J. Electrochem. Soc.*, 2005, *152* (11), C744.
44. Santos, M. C., et al., Voltammetric and rotating ring-disk studies of underpotential deposition of Ag and Cu on polycrystalline Au electrodes in aqueous H2SO4. *Electrochim. Acta*, 1998, *43* (16), 2263-2272.
45. Chen, D., et al., Determining the Active Surface Area for Various Platinum Electrodes. *Electrocatalysis*, 2011, *2*, 207-219.
46. Fang, L.-l., et al., Determination of the Real Surface Area of Palladium Electrode. *Chinese Journal of Chemical Physics*, 2010, *23* (5), 543-548.
47. Bizzotto, F., et al., Ir nanoparticles with ultrahigh dispersion as oxygen evolution reaction (OER) catalysts: synthesis and activity benchmarking. *Catalysis Science & Technology*, 2019, *9* (22), 6345-6356.
48. Pauporté, T., et al., Some electrocatalytic properties of anodic iridium oxide nanoparticles in acidic solution. *Electrochim. Acta*, 1999, *45* (3), 431-439.
49. Bett, J. A. S., et al., Crystallite growth of platinum dispersed on graphitized carbon black: II. Effect of liquid environment. *J. Catal.*, 1976, *41* (1), 124-133.
50. Grupioni, A. A. F., et al., Voltammetric characterization of an iridium oxide-based system: the pseudocapacitive nature of the Ir0.3Mn0.7O2 electrode. *Electrochim. Acta*, 2002, *48* (4), 407-418.
51. Zheng, J. P., et al., Hydrous Ruthenium Oxide as an Electrode Material for Electrochemical Capacitors. *J. Electrochem. Soc.*, 1995, *142* (8), 2699-2703.

52. McCrory, C. C., et al., Benchmarking heterogeneous electrocatalysts for the oxygen evolution reaction. *J. Am. Chem. Soc.*, 2013, *135* (45), 16977-87.
53. Sing, K. S. W., Reporting physisorption data for gas/solid systems with special reference to the determination of surface area and porosity (Recommendations 1984) %J Pure and Applied Chemistry. 1985, *57* (4), 603-619.
54. Wei, C., et al., Approaches for measuring the surface areas of metal oxide electrocatalysts for determining their intrinsic electrocatalytic activity. *Chem. Soc. Rev.*, 2019, *48* (9), 2518-2534.
55. Wang, L., et al., Improving the activity and stability of Ir catalysts for PEM electrolyzer anodes by SnO2:Sb aerogel supports: does V addition play an active role in electrocatalysis? *J. Mater. Chem. A*, 2017, *5* (7), 3172-3178.
56. Zhao, S., et al., Calculating the Electrochemically Active Surface Area of Iridium Oxide in Operating Proton Exchange Membrane Electrolyzers. *J. Electrochem. Soc.*, 2015, *162* (12), F1292-F1298.

CHAPTER 5. GENERAL CONCLUSIONS

The aim of the present thesis was to perform electrochemical studies on iridium based electrocatalysts with reduced iridium content by dopant effect of molybdenum under simplify and economic version of PEM water electrolysis conditions. The performance of the catalysts towards OER as anode material of PEM water electrolyzers was evaluated, as well as the influence of the catalysts content to enhance the surface area by lowering the metal.

In order to seek the above objectives, the highlighted different characteristics that the electrodes must present for PEMWE are mentioned in chapter 1. The different routes of synthesis to reduce the iridium content or to produce cost effective electrocatalyst with high surface area and tunable properties discussed in chapter 2 were considered to prepare the Ir-based oxides.

The spray-drying method was used to prepare the $Ir_{1-x}Mo_xO_2$ mixed oxides across the composition range x = 0, 0.1, 0.3, 0.5, 0.7 and 1 calcined between 400 – 800 °C. XRD analysis showed that the oxide crystallite size increased as sintering temperature increased, and as molybdenum was introduced the crystallization of the oxide was delay. Thus, single phases compounds were obtained for x = 0.1, 0.3 and 0.5 starting from the sintering temperatures of 450, 500 and 550 °C, respectively. SEM analysis showed that the sintered powders resulted in powders with ultraporous structure with different morphologies, and the porogen structure is preserved up to 600 °C.

The electrocatalytic activity and stability of the $Ir_{1-x}Mo_xO_2$ towards the OER were investigated using CV and chronoamperometry. The enhancement in catalytic activity by addition of molybdenum was clearly demonstrated by three-electrode electrochemical testing in 0.05 M H_2SO_4. Oxides with x = 0.1, 0.3 and 0.5 calcined at 450, 500 and 550 °C, respectively, exhibited the best performance towards OER. Meanwhile the stability of these oxide catalysts showed to be able to maintain a constant potential over the course of several hours during the oxygen evolution reaction process. XRD suggested that these electrocatalysts are not fully amorphous with the presence of rutile phase and crystallite size of 2 nm. Combined XPS and XANES measurements allowed to investigate the interaction between iridium and molybdenum in $Ir_{1-x}Mo_xO_2$ electrocatalysts. The analysis presented evidenced that the iridium oxidation state remains unchanged when introducing molybdenum, as well as when the temperature of calcination is increased, concluding that the oxidation does not rule over OER performances.

Double layer capacitance characterization by CV made possible to have a trend of $Ir_{1-x}Mo_xO_2$ electrocatalysts surface areas. The underpotential deposition of Hg method proved its relevance for the determination of the electrochemical surface area (ECSA), as well as for stability/degradation test when subjected to OER conditions. The integration of the Hg-UPD desorption peak gave reliable results that are consistent with BET analysis. The three main series showed that the highest ECSA value is reached when the mixed oxide is calcined at an optimal calcination temperature. Among the main electrocatalysts the oxide with 30% of molybdenum sintered at 500 °C exhibited the highest surface area with more active sites.

In conclusion, this study has shown that it is possible to reduce the iridium metal content of OER electrocatalysts by introduction non-noble metals such as Mo by a cost-effective synthesis method such spray-drying. Different electrochemical techniques can give an insight into the electrocatalysts behavior and porosity morphology. The tunable properties provided by this route of synthesis allowed to obtain highly porous mixed oxides, not fully amorphous, with high electrocatalytic activity and stability toward O_2 evolution reaction due to the high surface area with more accessible active sites. Meanwhile the protocol established by UPD of mercury allowed to determine the surface areas of the electrocatalysts with minimum quantity of material with values comparable to BET measurements.

CHAPTER 6. EXPERIMENTAL PROCEDURES

6.1. Sample preparation

The $Ir_{1-x}Mo_xO_2$ (x = 0, 0.1, 0.3, 0.5, 0.7 and 1) compounds tested in this thesis have been synthesized by the spray-drying technique at the LCMCP (group of Cédric Boissière, Sorbonne Université) by Dr. Mateusz Odziomek.

6.1.1. Material synthesis: Spray – drying technique

Spray-drying technique is a powder manufacturing method which consists in transforming the liquid that contains the particles of interest into its dried form by a rapid drying in a hot oven[1] (Figure 6.1). The method has been widely use in the pharmaceutical and food industries,[2] due to its low cost, water-based and scalable process. The general process involves three main steps:[1]

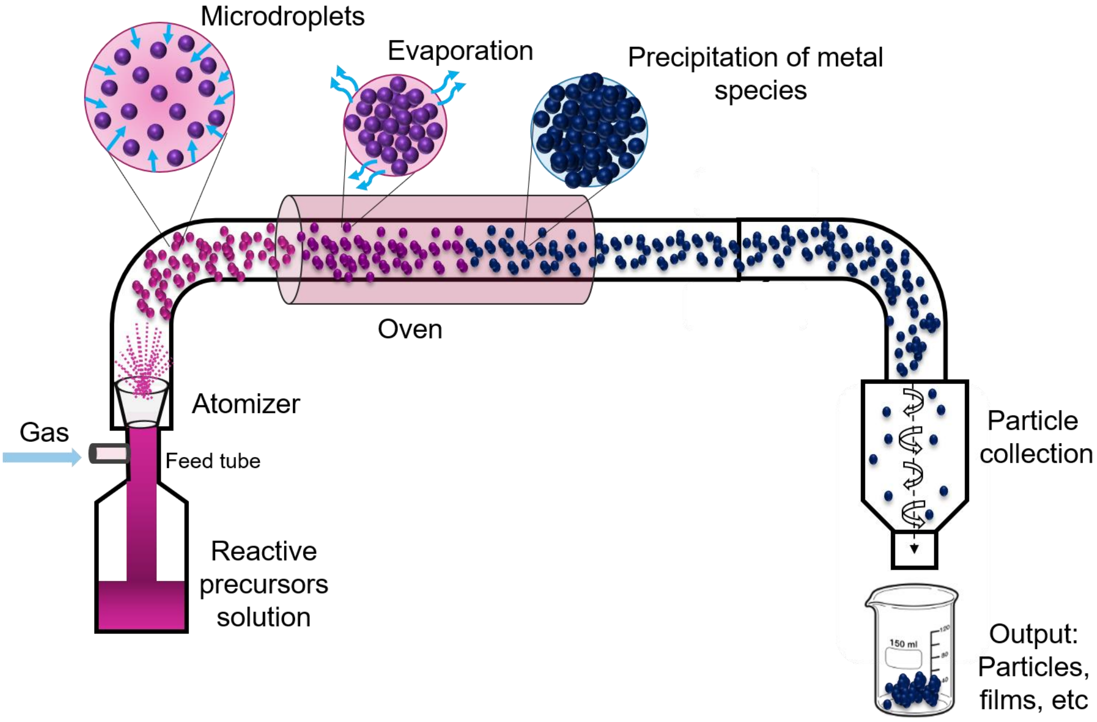

Figure 6.1 General schematic representation of spray-drying process

i. Atomization: the process starts with the feed of the liquid suspension into the atomizer by a pump. This step makes spray drying a method that allows the formation of particles with the desired physicochemical characteristics and morphological properties which depend strongly on the atomizer implemented. The common devices are rotary, ultrasonic and hydraulic atomizers; these ones are in charge of breaking up the suspension into microdroplets.

ii. Droplets: they are obtained by the action of either pressure, centrifugal or ultrasonic energy. The droplet feed is exposed immediately to hot air in a drying chamber, the temperature is adjusted to allow the best thermal process, in order to evaporate the solvent and as a result dried particle is obtained.

iii. Particle collection: The particles descend to the bottom of the chamber where they can be collected by bag filters or cyclone devices.

Furthermore, this method has been extensively used to produce porous catalyst [3-5] or nanocomposites [6, 7] since this process allows to tune the size and the morphology. The method was adapted to produce the mixed Ir-based oxide samples, $Ir_{1-x}Mo_xO_2$, using the synthesis method described below and illustrated in Figure 6.2.

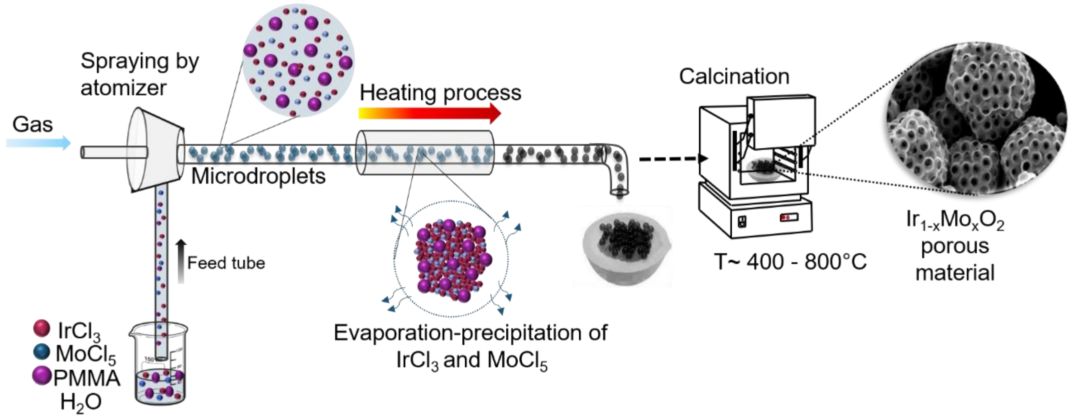

Figure 6.2 Synthesis of porous $Ir_{1-x}Mo_xO_2$ (x = 0, 0.1, 0.3, 0.5, 0.7 and 1) material.

The solution of precursors contained the inorganic reagents, hydrated iridium (III) chloride ($IrCl_3.xH_2O$, 98%, Alfa-Aesar) and molybdenum (V) chloride ($MoCl_5.xH_2O$, 98%, Sigma-Aldrich) in a ratio of 1 g dissolved in 27 mL of water. After constant stirring for 30 min, 11 wt. % colloidal dispersion of 300 nm spherical polymethylmethacrylate beads (PMMA template) was then introduced in the previous solution. The beads were synthesized by radical polymerization from methyl methacrylate following the protocol described by *Hatton et al.,*[8]. After another 10 min of stirring, the solution was first sprayed with an atomizer (B-290 atomizer, Büchi) to form microdroplets which were then transported by an air flux in a drying chamber (input temperature 220 °C, pump flow 5 mL min^{-1}) where evaporation took place, and the powder was then collected in a glass vessel by a vortex separator. The collected powder was then calcined above 350 °C since the polymer template is removed at this temperature, and the range selected was 400 – 800 °C. The powder was then calcined at 400 up to 800 °C for 15 min at each temperature under static air. Then, the iridium-molybdenum species are converted into oxides by aerial oxidation.[9, 10] Samples containing 30, 50 and 70%-Mo followed a 3 h / 30 min ramp up until the selected temperature. On the other hand, the 10%-Mo series for the sample calcined at 400 °C followed a ramp of 3 h, 450-500 °C a ramp of 5 h and 550-800 °C a ramp of 8 h, all this in order to avoid the formation of metallic iridium.

6.2. Characterization techniques

The $Ir_{1-x}Mo_xO_2$ (x = 0, 0.1, 0.3, 0.5, 0.7 and 1) compounds were characterized at the ITODYS (group of Jennifer Peron and Marion Giraud, Université de Paris) by Marine Elmaalouf (XRD and SEM).

6.2.1. X-Ray (XRD)

X-ray diffraction is a powerful technique used in the characterization of materials. It is primarily used for phase identification of a crystalline material which is provided by its diffraction pattern.

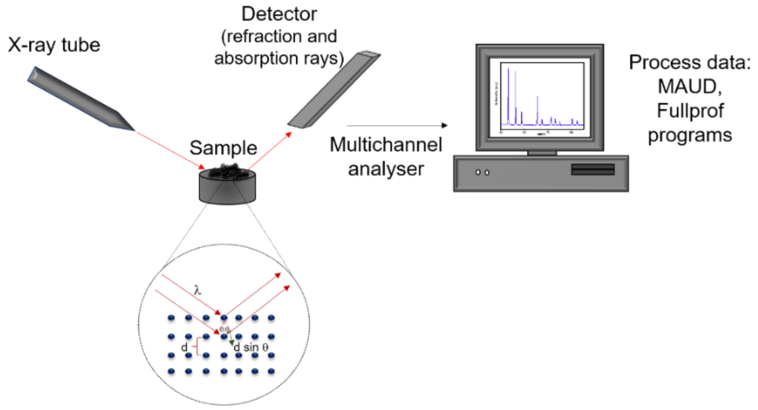

Figure 6.3 Illustration of the interaction between X-rays and sample to obtain a diffractogram while following the Bragg's Law.

The latter is obtained when the Bragg's law is satisfied, this one relates the wavelength (λ) to the diffraction angle (θ) and the lattice spacing (*d*) in a crystalline sample as given in Eq. 6-1.

$$n\lambda = 2d \sin\theta \; ; n = 1, 2, \ldots . \qquad (Eq.\ 6\text{-}1)$$

Once a diffraction pattern is obtained (Figure 6.3), Rietveld refinements are necessary in order to identify and quantify phases and structural changes present on the material, several programs are used to obtain the cell parameters such as Fullprof Suite program with its graphical interface WinPLOTR [11] and MAUD[12] programs. The results presented on this thesis were characterized by the ITODYS group on a Panalytical X'pert pro diffractometer equipped with a Co anode ($\lambda K\alpha$ = 1.789 Å) and a multichannel X'celerator detector. Each pattern was recorded in the θ - θ Bragg – Brentano geometry in the range 15 – 120 ° using 2θ step size of 0.0334 ° and compared to diffraction profiles reported in the ICSD (Inorganic Crystal Structure Database) and MAUD program for parameter extraction.

6.2.2. Scanning Electron Microscopy (SEM)

Scanning Electron Microscopy is a high-resolution imaging technique that uses beams of electrons to provide images where the structure and surface present on the materials of study are depicted. The path of the accelerated electrons is control by electromagnetic lenses, the condenser defines the size of the beam i.e., the resolution, and the objective lens is used to focus the beam on the sample (Figure 6.4).

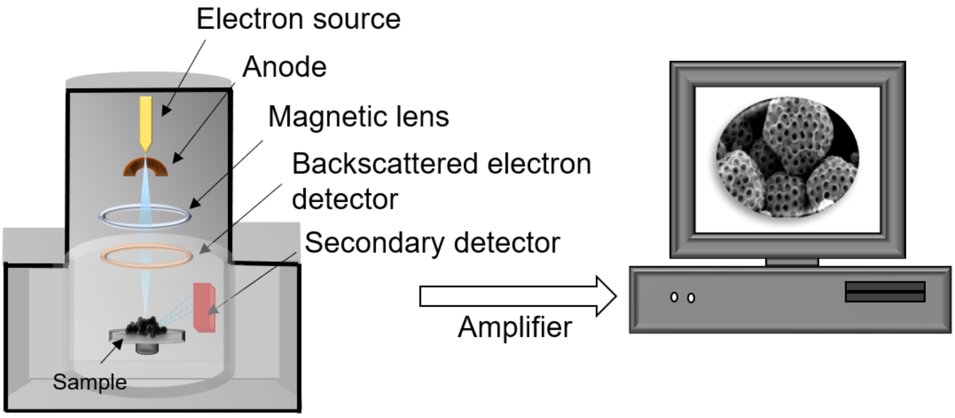

Figure 6.4 Basic components of a SEM instrument.

The instrument is based on the following principle: primary electrons generated by the electron source provide energy to the atomic electrons of the sample which then are release as secondary electrons, by collecting the latter, an image can be formed giving information about topography, morphology, orientation of grains, etc.[13] The SEM images presented on this work were obtain using a Zeiss SUPRA 40 FESEM operating at 5 kV.

6.3. Electrochemical measurements

Electrochemical measurements are a response of electrodes while being immersed in an electrolyte solution when they are subjected to an applied potential or a current. The results presented in this thesis were performed using a Rotating Disk Electrode (RDE). One of the advantage of this device is the rotation which allows the removal of the produced gas bubbles from the surface of the catalyst while OER and HER measurements are taking place, as well as the hydrodynamic assumption (working principle behind RDE) that the electrode is in a uniform contact in the solution which allows to obtain precise and reproducible control of the convection and diffusion of the reagent to the electrode.[14, 15] The equipment implemented in this thesis was a RDE (Pine Research Instrumentation) with a 5 mm diameter glassy carbon (GC) surrounded by a Teflon cylinder connected to a potentiostat Autolab PGSTAT 12 as presented in Figure 6.5.

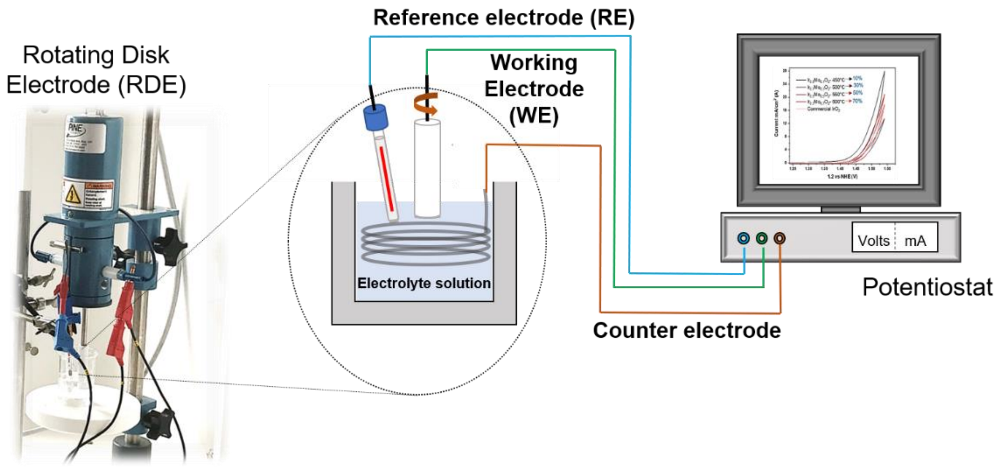

Figure 6.5 Electrochemical set-up measurements using a three-electrode cell with a rotating disk electrode.

6.3.1. Three-electrode set-up

In a general three-electrode set-up, both potential and current can be monitor simultaneously permitting to study the behavior of the analyte at the electrode/electrolyte interface. The system[16] is composed of (Figure 6.5):

i. Working electrode (WE): is the one in contact with the analyte to which the potential is applied and where the reaction of interest is occurring.
ii. Counter electrode (CE): is used to close the current circuit in the electrochemical set-up, passing all the necessary current to balance the current produce by the WE. The commonly use are Pt, Au or graphite.
iii. Reference electrode (RE): serve as a reference in measuring and controlling the WE potential. Saturated Calomel Electrode (SCE) and Ag/AgCl electrode are the most used.

The system works as described: an external voltage (*V*) is applied between the RE and the WE, an operational amplifier (present in the potentiostat) ensures that no electric current flows between the RE and WE, instead it flows between the CE and the WE, ensuring that the external voltage required is achieved. For this thesis, the WE is coated with the $Ir_{1-x}Mo_xO_2$ samples, the current flowed between the Ir-Mo oxides and the Pt wire (CE). The latter serves as a cathode since the case of study is the OER on the Ir-Mo oxides (anode materials). The potential applied between the WE and the RE is measured against Saturated Calomel

Electrode (RE), however, all the results are reported against Normal Hydrogen Electrode (NHE) and no against Reversible Hydrogen Electrode (RHE), since the latter potential depends on the pH of the solution, but still, both define the zero point in the electrochemical scale. For NHE, therefore 0.242 V must be added to correct the scale.

6.3.2. Electrode preparation

In order to achieve high quality films, these ones must be drop casted on a well-polished glassy carbon (GC) electrode. To achieve the "mirror finish" on the electrode the use of abrasives and polishing cloths were implemented on a Lam Plan polishing machine (Smartlam® 2.0) as shown in Figure 6.6.

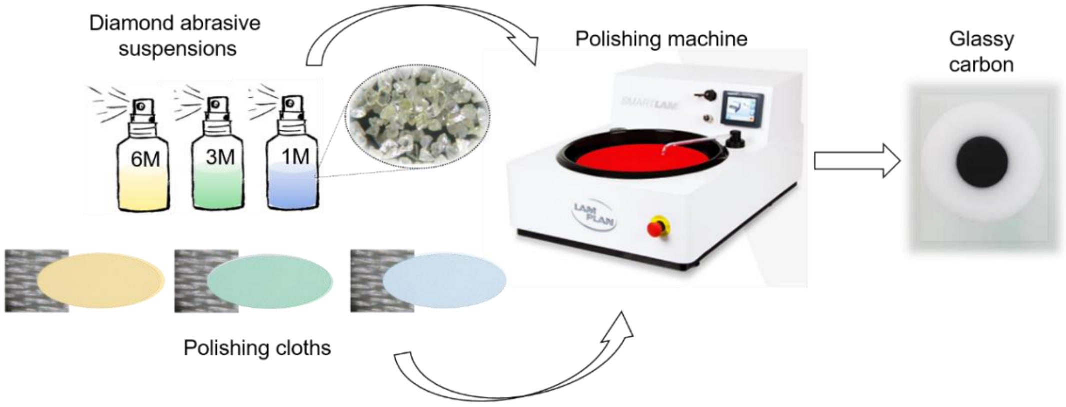

Figure 6.6 Illustration of the preparation of the working electrode surface.

Different diamond suspensions (1, 3 and 6M; Bio DIAMANT) were sprayed on polishing cloths with different roughness, for each cloth 2 minutes of polishing at 250 rpm was used. Starting with the suspension with the highest concentration (yellow) and finalizing with the suspension with the lowest one (blue). The electrode was rinsed with deionized water (0.059 µS cm^{-2}) and ethanol every time the disk and particle suspension were changed, and followed by ultrasonic bath and then dried at room temperature in air for 20 min before drop casting the ink.

6.3.2.1. Ink preparation

Catalyst ink properties and composition are crucial to achieve high quality films. Inks, typically, contain the catalyst, a perfluorosulfonic acid ionomer (usually Nafion) and a solvent (water/alcohol). Ink recipes are variable and are adjusted to the type of catalyst, however a main characteristic is to present a well-dispersed suspension and no flocculates.[17] To achieve this, properties such as viscosity and homogeneity [18] have to be taken into account, therefore the type of solvent plays a significantly role affecting the distribution of the ionomer on the catalyst surface as wells as its distribution on the surface area of the glassy carbon electrode.

Based on the above, the ink recipe for the Ir-Mo catalyst was the same as the one presented by *Faustini et al.,*[9] suspending ~1 mg of the catalyst sample with ~2 mg of carbon Vulcan XC72R (Cabot) in 250 µL of Nafion® solution (5% w/w, Alfa Aesar) and 250 µL of deionized water (0.059 µS cm^{-2}), and sonicated in an ultrasonic bath for 30 min. Once the catalyst ink is satisfactory, the last consideration to take into account to obtain a smooth film is the drying conditions of the ink droplet, which should cover the entire surface of the glassy carbon electrode. The drying of the film is directly related to the alcohol type, content, and ambient conditions (temperature and humidity).[17-20] Faustini used a drying temperature of 100 °C for 30 min in oven, however, in this work a drying temperature of 60 °C/ 30 min was used (Figure 6.7).

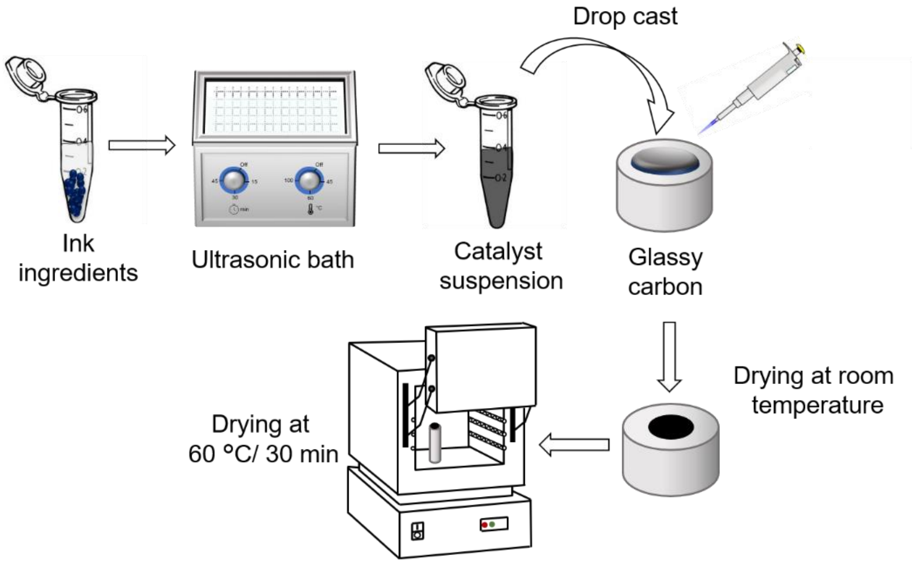

Figure 6.7 Schematic representation of the catalyst ink formation and drying

As a resume, all electrochemical tests were studied using a rotating disk electrode (RDE, Pine Research Instrumentation) with a potentiostat Autolab PGSTAT 12. The three-electrode cell set-up included a saturated calomel electrode (SCE) as a reference electrode (RE), a 5 mm diameter glassy carbon (previously polish and rinsed in ethanol) as a working electrode (WE) where 8 µL of catalyst ink was cast on (dried in air and at 60 °C/ 30 min in an oven), and a Pt wire as the counter electrode (CE).

6.3.3. Measuring techniques

6.3.3.1. Cyclic voltammetry (CV)

This electrochemical technique is considered as a basic electrochemical test for materials. As the potential is sweeping from positive to negative and vice versa, the current is being recorded. The graph (Figure 6.8) obtained from a CV gives information about the oxidation/reduction peaks as well as capacitive behavior, reversibility or irreversibility of the electrochemical processes, and potential catalytic activity of the material. A forward scan (positive slope) switches after reaching the first half-cycle to a reverse scan (negative slope) to complete the second half-cycle with the aim to reach the same position at which it started.[21]

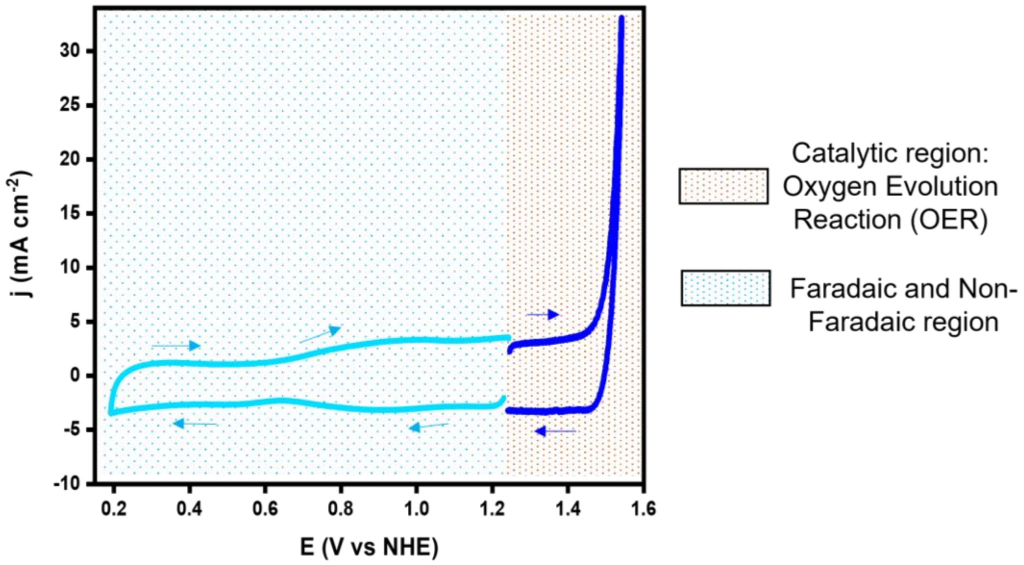

Figure 6.8 Graphical representation of a cyclic voltammogram zones.

The changes in the colored blue region when performing CV tests are due to the influence of the scan rate (slope in V s^{-1}), the slower the scan rate the lower charging current, while higher scan rates lead to higher flow of current. The catalytic activity of the Ir-Mo catalysts was done by measuring the OER at a constant rotating rate speed of 1600 rpm in a beaker containing a 0.05 mol L^{-1}

H_2SO_4 solution (ohmic drop of ca. 30 Ω) as supporting electrolyte solution as follows: 50 cycles in the range -0.2 V to 1.2 V followed by a forward scan recorded at 10 mV s^{-1} in the potential range of 1.2 –1.5 V.

a) Double layer capacitance

As mentioned above CVs can give detail capacitance behavior (Figure 6.8), since CV measurements consist of applying a potential at the electrode which varies linearly with time while the current is recorded, and the charge accumulated at the electrode makes it possible to estimate its capacitance. For this, the double layer capacitance (C_{dl}) region, which corresponds to a non-Faradaic region (no redox processes take place), must be determined.[22]

$$i = v \cdot C_{dl} \qquad \text{(Eq. 6-2)}$$

The capacitance is measured by recording several voltammograms at different scan rates. The plot of the current registered vs the scan rates gives a graph as in Figure 4.3b, where the slope (Eq. 6-2) results to be the C_{dl} usually given in the units of µF cm^{-2}.

In this thesis, the C_{dl} region was found to be between 0.89 V and 1.09 V as shown in Figure 4.9. The measurements were carried out in 0.1 M $HClO_4$ (ohmic drop of ca. 20 Ω) as supporting electrolyte solution while cyclic voltammograms were recorded in a non-faradaic region of the potential sweep at multiple scan rates (0.2, 0.15, 0.1, 0.05, 0.025 and 0.01 V s^{-1}).

b) Underpotential deposition (UPD) of metal

The deposition of the metal on to the substrate relays on the potential required to produce a monolayer while avoiding the bulk deposition, and the CV technique allows to deduce the underpotential deposition (UPD) shift (monolayer to bulk deposition).[23] The CV and UPD tools permit to characterize the materials surface, the phenomenon occurs (Figure 6.9) at slightly higher potentials than the potential necessary to reduce the substrate, therefore the UPD has to be measured in a region where no other redox processes take place. In this range, the metal is deposited as a monolayer on the substrate surface and its response is observe as a peak in the voltammogram.

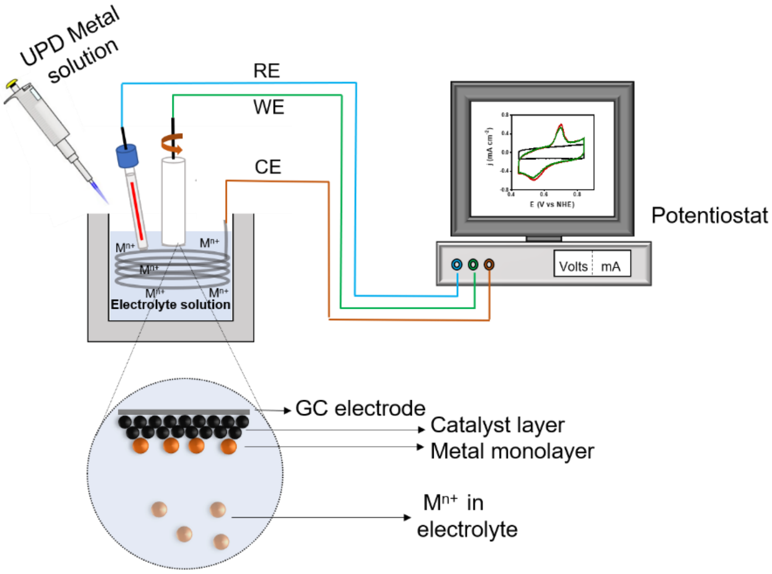

Figure 6.9 Schematic representation of Underpotential deposition (UPD) phenomenon.

The metal used in this work for the UPD measurements was mercury (Hg). Mercury underpotential deposition (Hg-UPD) tests for the electrochemical surface area (ECSA) measurements were carried out as follows modifying the protocol presented in ref:[24] cyclic voltammograms were taken at variable scan rates (0.1, 0.075, 0.05 and 0.025 V s^{-1}) in the range 0.2 V to 0.8 V in 0.1 M $HClO_4$ (ohmic drop of ca. 20 Ω) as supporting electrolyte solution before and after dropping 5 µL of 1 M mercury nitrate solution into the supporting electrolyte to achieve achieve a Hg^{2+} final concentration of 1mM in the final solution. OER measurements were performed by 10 cycles in the range 1.2 V to 1.5 V at 0.1 V s^{-1} as an electrochemical conditioning prior to ECSA measurements once mercury solution has been introduced. To process the desorption monolayer the Coulombic charge of 138.6 µC cm_{Ir}^{-2} was used as a conversion of factor.[24]

6.4. References

1. Cal, K.; Sollohub, K., Spray drying technique. I: Hardware and process parameters. *J. Pharm. Sci.*, 2010, *99* (2), 575-86.
2. Wang, S.; Langrish, T., A review of process simulations and the use of additives in spray drying. *Food Res. Int.*, 2009, *42* (1), 13-25.

3. Peron, J., et al., Hollow iridium-based catalysts for the oxygen evolution reaction in proton exchange membrane water electrolyzers. *ECS Trans.*, 2017, *80* (8), 1077-1084.
4. Debecker, D. P., et al., Aerosol processing: a wind of innovation in the field of advanced heterogeneous catalysts. *Chem. Soc. Rev.*, 2018, *47*, 4112-4155.
5. Lv, C., et al., Porous TiO_2 nanowire microsphere constructed by spray drying and its electrochemical lithium storage properties. *Microsc. Res. Tech.*, 2014, *77* (2), 170-5.
6. Yao, C., et al., Synthesis of PtCoNiRu/C nanoparticles by spray drying combined with reduction sintering for methanol electro-oxidation. *RSC Adv.*, 2020, *10* (6), 3579-3587.
7. Nishio, M., et al., Effective spray drying technique to prepare nanocomposite particles by preventing the growth of needle-like simvastatin crystal. *J. Drug Deliv Sci Technol*, 2019, *53*.
8. Hatton, B., et al., Assembly of large-area, highly ordered, crack-free inverse opal films. *Proc Natl Acad Sci U S A*, 2010, *107* (23), 10354-9.
9. Faustini, M., et al., Hierarchically Structured Ultraporous Iridium-Based Materials: A Novel Catalyst Architecture for Proton Exchange Membrane Water Electrolyzers. *Adv. Energy Mater.*, 2019, *9* (4), 1802136.
10. Boissiere, C., et al., Aerosol Route to Functional Nanostructured Inorganic and Hybrid Porous Materials. *Adv. Mater.*, 2011, *23* (5), 599-623.
11. T. Roisnel, J. R.-C., WinPLOTR: a Windows tool for powder diffraction patterns analysis Materials Science Forum, Proceedings of the Seventh European Powder Diffraction Conference (EPDIC 7). 2000, 118 - 123.
12. Lutterotti, L., et al., MAUD: a friendly Java program for material analysis using diffraction. *IUCr: Newsletter of the CPD*, 1999, *21*, 14-15.
13. Kalsoom Akhtar, S. A. K., Sher Bahadar Khan, Abdullah M. Asiri, Scanning Electron Microscopy: Principle and Applications in Nanomaterials Characterization. In *Handbook of materials characterization* Sharma, S. K., Ed. Springer: 2018; pp 116 - 121.
14. Albery, W. J.; Hitchman, M. L., *Ring-disc electrodes* Clarendon Press: 1971.
15. Guy Denuault, M. S., Kristy-Jo Williams, Classical experiments. In *Handbook of Electrochemistry*, Zoski, C. G., Ed. Elsevier: 2007; pp 431 - 469.
16. *Basic overview of the working principle of a potentiostat/galvanostat (PGSTAT) - Electrochemical cell set up*, 2011.
17. Garsany, Y., Experimental methods for quantifying the activity of platinum electrocatalysts for the oxygen reduction reaction. *Anal. Chem.*, 2010, *82* (15), 6321-6328.
18. Orfanidi, A., et al., Ink solvent dependence of the ionomer distribution in the catalyst layer of a PEMFC. *J. Electrochem. Soc.*, 2018, *165* (14), F1254-F1263.
19. S. j. Shin, et al., Effect of the catalytic ink preparation method on the performance of polymer electrolyte membrane fuel cells. *J. Power Sources*, 2002, *106*, 146-152.
20. De-Chin Huang, et al., Effect of Dispersion Solvent in Catalyst Ink on Proton Exchange Membrane Fuel Cell Performance. *Int. J. Electrochem. Sci.*, 2011, *6* (7), 2566-2580.
21. Yogesh S. Choudhary, L. J., Gomathi Nageswaran, Electrochemical Characterization. In *In Micro and Nano Technologies, Spectroscopic Methods for Nanomaterials Characterization*, Sabu Thomas, R. T., Ajesh K. Zachariah, Raghvendra Kumar Mishra, Ed. Elsevier: 2017; pp 19-54.
22. Ge, Y., et al., How to measure and report the capacity of electrochemical double layers, supercapacitors, and their electrode materials. *J. Solid State Electrochem.*, 2020, *24* (11-12), 3215-3230.
23. Sudha, V.; Sangaranarayanan, M. V., Underpotential deposition of metals – Progress and prospects in modelling. *J. Chem. Sci.*, 2005, *117* (3), 207-218.
24. Alia, S. M., et al., Mercury Underpotential Deposition to Determine Iridium and Iridium Oxide Electrochemical Surface Areas. *J. Electrochem. Soc.*, 2016, *163* (11), F3051-F3056.

ECOLE
DOCTORALE

Titre : Evaluation électrochimique d'électrocatalyseurs pour la réaction d'oxydation de l'eau : le cas de matériaux ultraporeux d'oxydes d'iridium et d'oxydes mixtes à base d'iridium

Mots clés : PEMWE, catalyse, électrochimie, electrocatalyseurs, iridium, poreux

Résumé : La diversification des sources d’énergie en incorporant des technologies propres et renouvelables devrait jouer en rôle important pour s’affranchir du système actuel dominé par les énergies fossiles. L’hydrogène est un vecteur énergétique renouvelable prometteur, et l’électrolyseur d’eau à membrane échangeuse de proton (PEMWE) est une technologie reconnue pour produire du H_2 de haute pureté. Néanmoins, et malgré les performances prometteuses, une utilisation à grande échelle de ce type d’électrolyseur est confrontée à des problématiques de coût et d’efficacité pour lesquelles le catalyseur anodique est l’un des principaux contributeurs du fait de sa composition (matériaux à base d’iridium) et des grandes surtensions nécessaires pour la réaction de production d’oxygène (OER) qui induisent une cinétique lente. Ce travail de thèse s’intéresse à l’étude électrochimique de différents catalyseurs à base d’iridium pour l’OER. Plusieurs stratégies ont été employées pour déterminer différentes propriétés comme la surface électroactive (ECSA) et la stabilité et la dégradation en condition d’électrolyse afin de pouvoir décrire, analyser et comparer les différents catalyseurs. Les dérivés d’oxydes mixtes de formule $Ir_{1-x}Mo_xO_2$ (x =0, 0.1, 0.3, 0.5, 0.7 and 1) ont été synthétisés par le procédé de spray-drying (déshydratation par atomisation) et calcinés à différentes températures entre 450 et 800°C. Les électrocatalyseurs ont été caractérisés par diffraction des rayons X sur poudre (XRD), microscopie électronique à balayage (SEM) et spectrométrie photoélectronique X (XPS). L’étude par SEM de ces matériaux a confirmé les morphonologies poreuses et amorphes à basses températures de calcination. L’analyse des spectres XRD a aussi pu notamment établir que la taille des cristallites augmentait avec la température de calcination et diminuait avec la teneur en molybdène. Les spectres XPS ont pu démontrer que les principaux états d’oxydation de ces oxydes mixtes étaient Ir^{3+}/Ir^{4+} ou Ir^{4+}. En utilisant une électrode à disque tournant (RDE), les caractérisations électrochimiques par voltammétrie cyclique (CV) et chronoampérométrie, ainsi que des mesures de capacitance de double couche (Cdl) et d’électrodéposition à sous-potentiel de mercure (Hg-UPD) ont permis de s’intéresser aux mesures de surface électroactive de ces matériaux. De plus, les voltammogrammes des différents oxydes mixtes ont mis en évidence l’influence de la température de calcination sur les performances électrocatalytiques. Trois composés de la série $Ir_{1-x}Mo_xO_2$ (x = 0.1, 0.3, 0.5) calcinés à 450, 500 et 550°C ont été étudiés pour leur stabilité comme matériaux anodiques. Les mesures de capacitance de double couche ont démontré qu’elles ne pouvaient être appliquées uniquement pour obtenir des tendances pour les mesures d’ECSA, alors que la méthode Hg-UPD permettait d’obtenir des résultats comparables aux mesures BET pour ces matériaux ultraporeux.

Title : Electrochemical evaluation of oxygen evolution reaction electrocatalysts: the case of ultraporous iridium oxide and iridium-based mixed oxide materials

Keywords : PEMWE, catalysis, electrochemistry, electrocatalysts, iridium, porous

Abstract : Diversifying energy sources by incorporating cleaner technologies i.e., renewable energy sources, are expected to play an important role to move from the current non-renewable dominated energy system. One of the promising energy carriers for renewable energy systems is hydrogen, and proton exchange membrane water electrolyzer (PEMWE) is one of the technologies known to produce highly pure H_2. Regardless the promising performances, large-scale use of such device faces efficiency and cost issues, among which the anode catalyst material is one of the main contributors due to its composition (Ir-based materials) and high overpotential towards the oxygen evolution reaction (OER) (slow kinetic). This thesis work aimed to electrochemically study several Ir-based OER catalysts by different strategies since properties such as electrochemical surface area (ECSA), stability/degradation tests and catalytic processes are critical characteristics to describe, analyze and compare electrocatalysts. The mixed oxides derived from $Ir_{1-x}Mo_xO_2$ (x =0, 0.1, 0.3, 0.5, 0.7 and 1) were synthesized by the spray-drying process and calcined at different temperatures in the range 450–800 °C. The electrocatalysts were characterized by X-ray powder diffraction (XRD), scanning electron microscopy (SEM), and X-ray photoelectron spectroscopy (XPS). The SEM study of these materials confirmed the amorphous - porous morphologies at lower calcination temperatures. XRD analysis showed that the crystallite size increases with temperature and decreases with molybdenum content. XPS spectra demonstrated that the main oxidation states present on the mixed oxides are Ir^{3+}/Ir^{4+} or Ir^{4+}. The electrochemical characterization using rotating disc electrode (RDE) technique consisted of cyclic voltammetry (CV) and chronoamperometry, as well as double layer capacitance (Cdl) and Hg underpotential deposition (Hg-UPD), which allowed to investigate their ECSA. The CV of all the mixed oxides allowed to compare and observed the influence of the sintering temperature on the performance towards OER. Three of the compounds of the series $Ir_{1-x}Mo_xO_2$ (x = 0.1, 0.3, 0.5) calcined at 450, 500 and 550 °C were studied for stability as anode materials. The Cdl method allowed to obtain a trend of the charging current behavior of the electrocatalyst as function of the sintering temperature, while the HgUPD method results prove its relevancy and applicability for ultraporous and Ir-mixed oxides when tested in RDE giving consistent ECSA values in agreement with BET measurements.

Institut Polytechnique de Paris
91120 Palaiseau, France